Master's Thesis

Kinematic Analysis of the Standard Missile-2 Block IIIA Surface-to-Air Missile

Development of engagement envelopes against Houthi weapon systems for fleet defence

Author: Jacco Huising

Supervisors: Dr.ir. Ralph Savelsberg and Dr.ir. Roelof Vos

TU Delft Delft University of Technology

Collectie Nederlands Instituut voor Militaire Historie, 2006

This page intentionally left blank

Master's Thesis

Kinematic Analysis of the Standard Missile-2 Block IIIA Surface-to-Air Missile

Submitted in partial fulfillment of the requirements for the degree of

Master of Science

In

Aerospace Engineering

At

Delft University of Technology

Student:

Jacco Huising - 5654076

Supervisors:

Dr.ir. Ralph Savelsberg - Netherlands Defence Academy

And

Dr.ir. Roelof Vos - TU Delft

June 2024

Delft University of Technology

Abstract

The Standard Missile-2 Block IIIA is the current medium-range Surface-to-Air missile in service with the Royal Netherlands Navy. Since November 2023, Houthi terrorists have been striking commercial shipping in the Red Sea and the Gulf of Aden, severely impacting between Europe and Asia. Using publicly available information, this thesis investigates the kinematic performance of the SM-2 Block IIIA and its area-defence capabilities against Houthi drones and Anti-Ship Cruise Missiles. A modified point mass simulation model was developed to simulate the SM-2 intercepting flying targets. The SM-2's kinematic performance was analysed by developing flyout tables. Engagement envelopes were developed to analyse the SM-2's area-defence capabilities against crossing targets. The SM-2 is found to have a maximum sea-level adjusted burnout Mach number of 3.8, a maximum ground range of 173 km, and a service ceiling of 20-25 km. The SM-2 is found to be capable of providing extensive area-defence coverage against each modelled weapon system.

Contents

List of Figures

List of Tables

List of symbols

Roman letter	Description
a	Acceleration
$\mathbf{a}$	Acceleration vector
A	Area, Intermediate value (no definition)
AR	Aspect Ratio
$[A]$	Euler angle transformation matrix
B	Intermediate value (no definition)
c	Chord length
C	Intermediate value (no definition)
D	Drag force, diameter
F	Force
$\mathbf{F}$	Force vector
g	Gravitational acceleration
$\mathbf{g}$	Gravitational acceleration vector
h	altitude, wing span
$\mathbf{h}$	Angular momentum vector
$[\mathbf{I}]$	Inertia matrix
I	Inertia
J	Performance index
k	Thermal conductivity
K	Intermediate value (no definition)
L	Roll moment, Lift force, lead angle, missile length
m	Missile mass
M	Pitch moment, Mach number
$\mathbf{M}$	Moment vector
n	Acceleration, trajectory shaping gain for midcourse guidance
N	Yaw moment
N'	Navigation gain
p	Roll rate, pressure
$\dot{p}$	Time derivative of p
$[p]$	Transformation matrix from LCIC MBCF
$[\bar{p}]$	Average of $[p]$ over whole flight envelope during midcourse guidance
$\mathbf{P}$	Intermediate value vector (no definition)
Pr	Prandtl number
q	Pitch rate, quaternion
$\dot{q}$	Time derivative of q
$\mathbf{Q}$	Intermediate value vector (no definition)
$[Q]$	Quaternion transformation matrix
r	Yaw rate, range, recovery factor
$\dot{r}$	Time derivative of r
R	Total range, universal gas constant
$\mathbf{R}$	Range vector

Roman letter	Description
Re	Reynolds number
S	Surface area
$[S]$	Intermediate matrix (no definition)
$[\bar{S}]$	Intermediate matrix (no definition)
t	Time
T	Thrust force, temperature
u	Velocity in x-direction in MBCF
$\dot{u}$	Time derivative of u
v	Velocity in y-direction in MBCF
$\dot{v}$	Time derivative of v
V	Velocity
$\mathbf{V}$	Velocity vector
$\dot{\mathbf{V}}$	Time derivative of $\mathbf{V}$
w	Velocity in z-direction MBCF
$\dot{w}$	Time derivative of w
X	Distance from nose tip along missile longitudinal axis

Greek letter	Description
α	Angle of attack
β	Angle of sideslip, normalized speed parameter
δ	Control surface deflection, angular deviation from collision course in vertical plane
ζ	Damping
η	Aerodynamic efficiency factor
θ	Body pitch angle
$\dot{\theta}$	Time derivative of θ
λ	LOS angle
μ	Dynamic viscosity, angular error between present missile velocity vector and specified terminal intercept angle in the vertical plane
$\dot{\lambda}$	LOS rate
$\dot{\boldsymbol{\lambda}}$	LOS rate vector
ρ	Air density
τ	Autopilot time constant
ϕ	Body roll angle
$\dot{\phi}$	Time derivative of ϕ
ψ	Body yaw angle
$\dot{\psi}$	Time derivative of ψ
ω	Trajectory-shaping coefficient, frequency, intermediate value (no definition)
$\boldsymbol{\omega}$	Angular rate vector, natural frequency
$\dot{\boldsymbol{\omega}}$	Time derivative of $\boldsymbol{\omega}$

List of symbols with subscripts and superscripts

Roman letter	Description
a_c	Commanded acceleration normal to the current velocity vector in vertical plane
$\mathbf{a}_c^{LCIC}$	Commanded acceleration vector in LCIC frame
a_x^{MBC}	Acceleration command in x-direction in MBCF
a_x^{LCIC}	Acceleration command in x-direction in LCIC
a_y^{MBC}	Acceleration command in y-direction in MBCF
a_y^{MBC}	Acceleration command in y-direction in LCIC
a_z^{MBC}	Acceleration command in z-direction in MBCF
a_z^{MBC}	Acceleration command in z-direction in LCIC
$\mathbf{a}_c$	Commanded acceleration vector normal to the current velocity vector
$\mathbf{a}_{long}$	Acceleration along missile x-axis in MBCF
$\mathbf{a}_M$	Missile acceleration normal to LOS
$\mathbf{a}_T$	Target acceleration normal to $\mathbf{v}_T$
A_N	Nose area
A_B	Body area
$[A]_{LCIC}^{MBC}$	Euler angle transformation matrix from LCIC to MBC
c_p	Constant-pressure heat capacity
c_{RT}	Root chord length tail wing
c_{RW}	Root chord length main wing
c_{TT}	Tip chord length tail wing
c_{TW}	Tip chord length main wing
C_{D_0}	Zero-lift drag coefficient
C_{D_i}	Lift-induced drag coefficient
C_f	Drag coefficient due to friction
C_{l_p}	Roll moment coefficient to due roll rate
C_{l_δ}	Roll moment coefficient due to control surface deflection
C_L	Lift coefficient
C_{L_α}	Lift coefficient derivative w.r.t. α
C_{M_L}	Moment coefficient due to lift
$C_{M_{trim}}$	Moment coefficient at trim conditions
C_{M_x}	Moment coefficient about x-axis
C_{M_y}	Moment coefficient about y-axis
$C_{M_{y_L}}$	Moment coefficient about y-axis due to lift
C_{M_z}	Moment coefficient about z-axis
$C_{M_{z_L}}$	Moment coefficient about z-axis due to lift
C_{M_α}	Moment coefficient derivative w.r.t. α
$C_{M_{\alpha_{trim}}}$	Moment coefficient derivative w.r.t. α at trim conditions
C_{M_δ}	Moment coefficient derivative w.r.t. δ

Roman letter	Description
$C_{M_{\delta_{trim}}}$	Moment coefficient derivative w.r.t. δ at trim conditions
C_{N_L}	Normal force coefficient due to lift
$C_{N_{trim}}$	Normal force coefficient at trim conditions
C_{N_x}	Normal force coefficient along x-axis
$C_{N_{x_D}}$	Normal force coefficient along x-axis due to drag
C_{N_y}	Normal force coefficient along y-axis
$C_{N_{y_D}}$	Normal force coefficient along y-axis due to drag
$C_{N_{y_L}}$	Normal force coefficient along y-axis due to lift
C_{N_z}	Normal force coefficient along z-axis
$C_{N_{z_D}}$	Normal force coefficient along z-axis due to drag
$C_{N_{z_L}}$	Normal force coefficient along z-axis due to lift
C_{N_α}	Normal force coefficient derivative w.r.t. α
$C_{N_{\alpha_{trim}}}$	Normal force coefficient derivative w.r.t. α at trim conditions
C_{N_δ}	Normal force coefficient derivative w.r.t. δ
$C_{N_{\delta_{trim}}}$	Normal force coefficient derivative w.r.t. δ at trim conditions
$\mathbf{C}_1$	Intermediate value vector (no definition)
$\mathbf{C}_2$	Intermediate value vector (no definition)
D_0	Zero-lift drag force
D_f	Drag force due to friction
$D_{inner,p}$	Inner diameter of propellant section
$D_{M,empty}$	Distance between centers of gravity of empty and non-empty missile
$D_{M,p}$	Distance between centers of gravity of missile and propellant section
D_{outer}	Outer missile diameter
$F^b_{A_x}$	Aerodynamic force along x-axis in MBCF
$F^b_{A_y}$	Aerodynamic force along y-axis in MBCF
$F^b_{A_z}$	Aerodynamic force along z-axis in MBCF
F_x	Force along x-axis
F^b_x	Force along x-axis in MBCF
F_y	Force along y-axis
F^b_y	Force along y-axis in MBCF
F_z	Force along z-axis
F^b_z	Force along z-axis in MBCF
$\mathbf{F}^b_A$	Aerodynamic force vector in MBCF
$\mathbf{F}^b$	Force vector in MBCF
$\mathbf{F}^b_g$	Gravitational force vector in MBCF
$\mathbf{F}^{LCIC}_g$	Gravitational force vector in LCIC frame
$\mathbf{F}^b_p$	Propulsive force vector in MBCF
g_0	Gravitational acceleration at sea level
$\mathbf{g}^{LCIC}_{comp}$	Gravity compensation vector in LCIC frame
h_T	Tail wing span
h_w	Main wing span
$\mathbf{i}_{MF}$	Missile velocity unit vector at PCP
I_{sp}	Specific impulse
$I_{sp,boost}$	Specific impulse of booster
$I_{sp,sustain}$	Specific impulse during sustain phase
$I_{x_{CG,tot}}$	Inertia about interceptor x-axis originating from center of gravity

Roman letter	Description
$I_{x_{CG,empty}}$	Inertia about interceptor x-axis due to empty missile
$I_{x_{CG,p}}$	Inertia about interceptor x-axis due to propellant
$I_{y_{CG,tot}}$	Inertia about interceptor y-axis originating from center of gravity
$I_{y_{CG,empty}}$	Inertia about interceptor y-axis due to empty missile
$I_{y_{CG,p}}$	Inertia about interceptor y-axis due to propellant
$I_{z_{CG}}$	Inertia about interceptor z-axis originating from center of gravity
$I_{z_{CG,empty}}$	Inertia about interceptor z-axis due to empty missile
$I_{z_{CG,p}}$	Inertia about interceptor z-axis due to propellant
K_0	Intermediate value (no definition)
K_1	Time-varying weighting factor, aerodynamic acceleration gain
K_2	Time-varying weighting factor
K_3	Aerodynamic body rate gain
K_A	Autopilot gain
K_C	Intermediate value (no definition)
K_{DC}	Autopilot gain
K_R	Autopilot gain
$\mathbf{l}_1$	Intermediate value vector (no definition)
$\mathbf{l}_2$	Intermediate value vector (no definition)
L_A	Aerodynamic roll moment
L_p	Propellant section length
L_α	Lift force derivative w.r.t. α
L'	Nose section length
m_0	Missile mass at launch
$\mathbf{m}_1$	Intermediate value vector (no definition)
$\mathbf{m}_2$	Intermediate value vector (no definition)
m_{empty}	Empty missile mass
m_p	Propellant mass
m_{p_0}	Propellant mass at launch
$m_{p_{start,sustain}}$	Propellant mass at start of sustain phase
M_A	Aerodynamic pitch moment
M_α	Moment derivative w.r.t. α
M_δ	Moment derivative w.r.t. δ
$\mathbf{M}_A^b$	Aerodynamic moment vector in MBCF
$\mathbf{M}^b$	Moment vector in MBCF
n_c	Commanded acceleration
n_c'	Commanded acceleration multiplied by autopilot gain K_{DC}
n_L	Achieved acceleration
N_A	Aerodynamic yaw moment
N_α	Normal force derivative w.r.t. α
N_δ	Normal force derivative w.r.t. δ
$q_{0,1,2,3}$	Quaternions
q_d	Dynamic pressure
$[Q]_{MBC}^{LCIC}$	Quaternion transformation matrix from MBC to LCIC
r_x	Range from missile to target in LCIC x-direction
r_y	Range from missile to target in LCIC y-direction
r_z	Range from missile to target in LCIC z-direction
$\mathbf{r}_M$	Range vector from LCIC origin to missile c.g.

Roman letter	Description
$\mathbf{r}_T$	Range vector from LCIC origin to target
R_e	Radius of Earth
R_{MPCP}	Range from missile to PCP
$\mathbf{R}_M$	Range vector from LCIC origin to missile c.g.
$\mathbf{R}_{PCP}$	Range vector from LCIC origin to PCP
Re_c^*	Reynolds number due to chord length based on reference temperature
S_{Plan}	Planform surface area
S_{Ref}	Reference surface area
S_T	Tail wing surface area
S_W	Wing surface area
$t_{burnout}$	Time at burnout
T_∞	Atmospheric temperature
T_0	Temperature at sea level
T_{aw}	Adiabatic wall temperature
T_{go}	Time-to-go
T_α	Turning rate constant
T^*	Reference temperature
V_C	Closing velocity
V_{MF}	Predicted missile velocity at PCP
$\mathbf{V}^b$	Missile velocity in MBCF
$\dot{\mathbf{V}}^b$	Time derivative of $\mathbf{V}_b$
$\mathbf{V}^{LCIC}$	Missile velocity in LCIC frame
$\dot{\mathbf{V}}^{LCIC}$	Time derivative of $\mathbf{V}_{LCIC}$
$\mathbf{V}_M$	Missile velocity vector
$\mathbf{V}_{MF}$	Predicted missile velocity vector at PCP
$\mathbf{V}_T$	Target velocity
X_{CG}	Distance from missile nose tip to center of gravity
$X_{CG_{boost,end}}$	Distance from missile nose tip to center of gravity of empty missile
$X_{CG_{boost,start}}$	Distance from missile nose tip to center of gravity at end of boost phase
$X_{CG_{empty}}$	Distance from missile nose tip to center of gravity at start of boost phase
$X_{CG_{propellant}}$	Distance from missile nose tip to center of gravity of propellant
X_{CPB}	Distance from missile nose tip to body center of pressure
X_{CPN}	Distance from missile nose tip to nose center of pressure
X_{CPW}	Distance from missile nose tip to wing center or pressure
X_{HL}	Distance from missile nose tip to tail wing hinge line
X_W	Font body length

Greek letter	Description
α_{trim}	Angle of attack at trim
γ_v	Vertical flight path angle
$\bar{\gamma_v}$	Average vertical flight path angle over flight envelope during midcourse guidance
$\gamma_{v,d}$	Desired (specified) vertical flight path angle at PCP
δ_r	Control surface deflection to generate roll moment
δ_{trim}	Control surface deflection at trim
ζ_0	Intermediate value (no definition)
ζ_{ACT}	Actuator damping
ζ_{AF}	Airframe damping
λ_M	Missile flight path angle
λ_T	Target flight path angle
μ_0	Dynamic viscosity at sea level
μ^*	Reference dynamic viscosity
ρ_p	Propellant density
ρ^*	Reference density
ψ_h	Velocity vector heading angle
$\bar{\psi_h}$	Average heading angle over flight envelope during midcourse guidance
$\psi_{h,d}$	Desired (specified) heading angle at PCP
ω_{ACT}	Actuator natural frequency
ω_{AF}	Airframe natural frequency
ω_{CR}	Crossover frequency
ω_I	Autopilot gain
ω_z	Airframe zero
$\boldsymbol{\omega}^b$	Angular rate vector in MBCF
$\dot{\boldsymbol{\omega}}^b$	Time derivative of $\boldsymbol{\omega}^b$
$\boldsymbol{\omega}^{LCIC}$	Angular rate vector in LCIC frame
$\dot{\boldsymbol{\omega}}^{LCIC}$	Time derivative of $\boldsymbol{\omega}^{LCIC}$

List of abbreviations

Abbreviation	Description
3-DOF	3 Degrees-of-Freedom
6-DOF	6 Degrees-of-Freedom
2T	Terrier/Tartar
ADCF	Air Defence and Command Frigate
AIAA	American Institute of Aeronautics and Astronautics
APAR	Active Phased Array Radar
APN	Augmented Proportional Navigation
ASBM	Anti-Ship Ballistic Missile
ASCM	Anti-Ship Cruise Missile
CPN	Compensated Proportional Navigation
DTRM	Dual-Thrust Rocket Motor
ECEF	Earth-Centered Earth-Fixed
ECM	Electronic Counter Measure
EG	Explicit Guidance
EoM	Equations of Motion
ER	Extended Range
FCS	Fire Control System
GENEX	Generalized Explicit Guidance
HM	Hinge Moment
ICWI	Interrupted Continuous Wave Illumination
IRU	Inertial Reference Unit
LACM	Land-Attack Cruise Missile
LCIC	Launch-Centered Inertial Cartesian
LOS	Line-of-Sight
MBC	Missile Body Coordinate
MBCF	Missile Body Coordinate Frame
MFR	Multi Function Radar
NED	North-East-Down
OC	Optimal Control
PID	Proportional-Integral-Derivative
PIP	Predicted Intercept Point
PCP	Primary Command Point
PN	Proportional Navigation
SAM	Surface-to-Air Missile
SM-2	Standard Missile-2
USCENTCOM	United States Central Command
VLS	Vertical Launching System

This page intentionally left blank

Acknowledgements

Gratitude is due to those people, without whom I would not have been able to complete my thesis and to those who lovingly supported me this past year. Thank you.

First and foremost I would like to extend my deepest gratitude to my thesis supervisor, Dr. Ralph Savelsberg, who for the past year has guided my work with such passion and personal attention. Without Ralph's knowledge and eagerness to invest time and effort, I would not have been able to complete this thesis. Ralph and I spent many hours together, discussing new ideas, comparing work, and chatting about our shared interest for military technology. Secondly, I want to thank professor Roelof Vos of the Technical University of Delft, who very sympathetically accepted the research proposal to model the Standard Missile-2, allowing me to research that which truly sparks my interest. Dr. Vos is doing great work in his lecture series on aircraft design, his research into new forms of aviation, and in guiding student's theses. Thirdly, I want to thank my colleagues at the Command Materiel and IT (COMMIT) of the Dutch Ministry of Defence. Their knowledge and advice were of great value in shaping this work. While working on this thesis and during a previous internship, I felt like I was really 'part of the team'. I am proud to say that I will continue working for COMMIT as an engineer.

My dear wife, who was pursuing her master's degree in Agricultural Engineering at the Catholic University of Leuven and I spent many days apart because I stayed at the base in the Netherlands multiple nights per week to have access to the office. I thank her for our sacrifice of having to miss each other so many days this past year. Frieda, your love and gentleness melt my heart every day! Now that we both completed our studies, we can truly start our family.

The International Catholic Church of Sint Kwinten in Leuven has been of great spiritual help in our academic pursuits and married life. Pursuing master's degrees in different countries and deepening our love for each other is hard, but with everyone in the community praying for each other, anything is possible in the name of Jesus. It is so inspiring to see so many students and young families at Church, the Holy Spirit is truly here.

Ave Maria, gratia plena,
Dominus tecum.
Benedicta tu in mulieribus
et benedictus fructus ventris tui, Iesus.

Sancta Maria, Mater Dei,
ora pro nobis peccatoribus,
nunc et in hora mortis nostrae.
Amen.

1. Introduction

The Standard Missile-2 (SM-2) Block IIIA is the current medium range Surface-to-Air Missile (SAM) of the Royal Netherlands Navy. The missile has a reported top speed of Mach 3, a maximum effective range of 167 km and a service ceiling of 20 km [1]. The SM-2 is designed against both sea-skimming and high-altitude targets, as well as "high-speed manoeuvring targets in a severe electronic countermeasure (ECM) environment" [1]. The Dutch ministry of Defence has expressed its desire to develop an in-house digital interceptor model of the SM-2. This model should aid in developing in-house knowledge on missile modelling to aid in the acquisition processes of future ship- and fleet-defence interceptors. In order for the development and results of the model to be available as a publicly publishable MSc. thesis and allow for using the model in an unclassified environment, the model has to be entirely based on open-source information.

Since October 2023, the Islamist terrorist group Ansar Allah, also known as the Houthis, have been firing drones, Anti-Ship Cruise Missiles (ASCM's) and Anti-Ship Ballistic Missiles (ASBMs) at civilian cargo ships in the Red Sea and the Gulf of Aden [2], [3], [4], [5]. Figure 1 shows a map, published by the BBC, displaying where commercial ships have been attacked by Houthi drones and missiles [5].

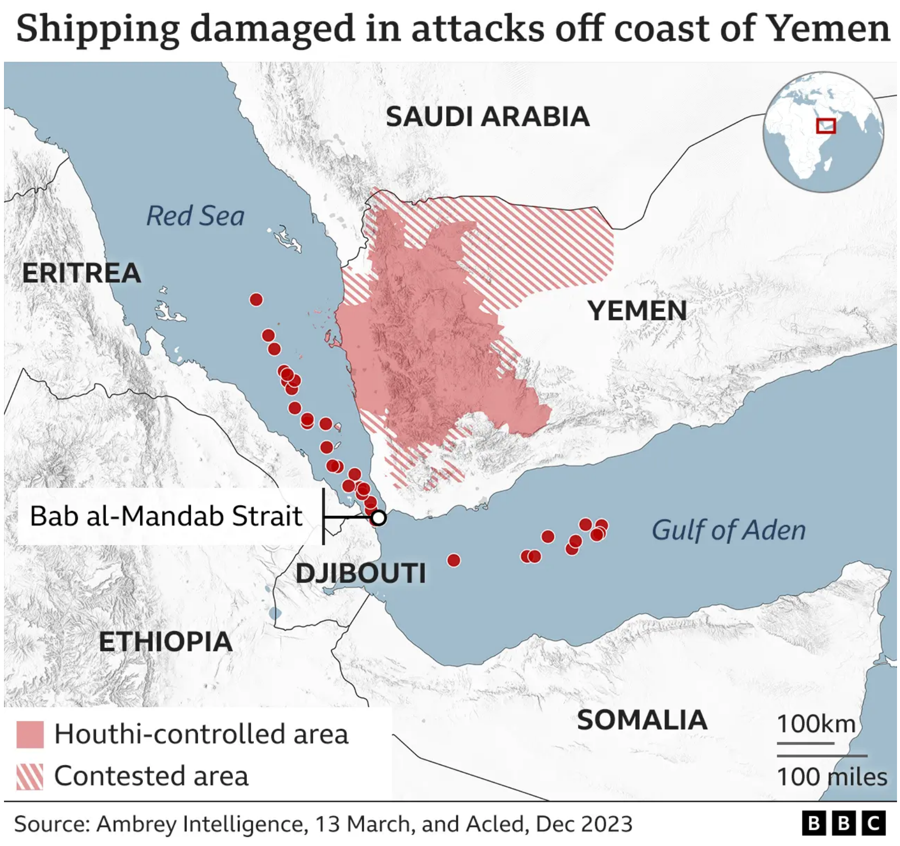

Figure 1: Locations of commercial ships struck by Houthi drone- and missile attacks. Source: BBC [5].

On February 19, 2020, U.S. Central Command (USCENTCOM) reported the interdiction of multiple Dhow boats smuggling weapons and cruise missile components by the USS

Forrest Sherman on November 19, 2019 and by the USS Normandy on February 9, 2020 [6]. Figure 2 presents some of the weapons and missile components that were seized, including anti-tank guided missiles, surface-to-air missiles, and components for the Quds-1/"351" Land-Attack Cruise Missile (LACM) and Noor/C-802 Anti-Ship Cruise Missile (ASCM). The "Quds-1" LACM, known as the "351" by USCENTCOM, is a Houthi variant of the Iranian "Soumar" family of Land-Attack Cruise Missiles, with a claimed range of 800km [7]. The "Noor" ASCM is an Iranian export variant of the C-802 [3], itself a member of the Chinese YJ-83 "Saccade" family, and has a maximum range of 120km [3], [7], [8], [9]. The Houthis have previously deployed the C-802 in attacks on ships. In October 2016, the Houthis fired a C-802 at the United Arab Emirates-leased HSV Swift and struck the ship [10], [11].

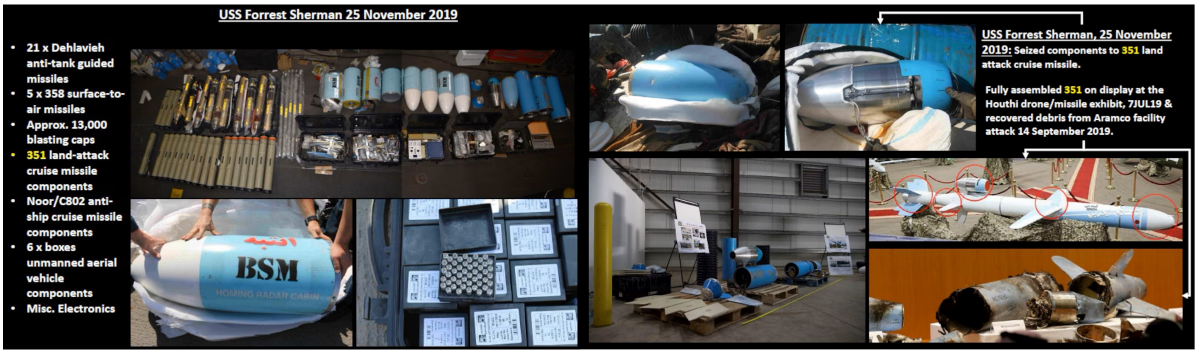

Figure 2: Seized Houthi weapons, including Quds-1 ("351") and C-802 "Noor" cruise missile components. Image source: United States Central Command [6].

The Houthis claim to also be in possession of the Iranian-made extended-range "Ghadir" variant of the C-802, dubbed the "Al-Mandab 2" [3], as well as the "Sayyad" and "Quds Z-0" Anti-Ship variants of the Quds family LACM's [12]. Iranian state media claim that the maximum range of the Ghadir/Al-Mandab 2 has been increased to 300 km [3], [13]. The Sayyad and Quds Z-0 ASCM variants of the Quds LACM family are claimed to have a range of 800 km [3], [12], equal to that of the original Quds-1 ("351") Land-Attack version [7]. The Sayyad employs a radar seeker to hit its targets, whereas the Quds Z-0 uses an electro-optical or infrared seeker [12]. Figure 3 presents two photos of the Al-Mandab 2/Ghadir (left) and the Sayyad (right) Anti-Ship Cruise Missiles during a Houthi military parade [12].

Figure 3: Left: "Al-Mandab 2/Ghadir" extended-range version of the C-802 Anti-Ship Cruise Missile during a Houthi parade. Image source: Overt Defense [14]. Right: "Sayyad" radar-guided Anti-Ship variant of the Quds family Land-Attack Cruise Missile during a Houthi parade. Image source: IISS [12].

On February 12th, 2024, Forces.net reported a photo taken of the HMS Diamond, a Type 45 Destroyer of the British Royal Navy, sailing into the port of Gibraltar after its deployment in the Red Sea [15]. In the photo, the ship displays kill markings, with the silhouettes of drones it shot down during its deployment in the Red Sea. In the photo, the silhouettes are identified to be that of the Samad-2, Shahed-136, and Mersad-2 [15]. On March 20, 2024, the French armed forces published a video on X (formerly Twitter) of a French helicopter intercepting, what seems to be, a Houthi Samad-2 drone en-route to a commercial vessel in the Red Sea, using its on-board gun, as part of the European Union's Aspides mission [16]. Figure 4 shows the type Type-45 "HMS Diamond" with its kill markings (left) and a screenshot of the video of the French helicopter intercepting the Samad-2 drone (right) [15], [16].

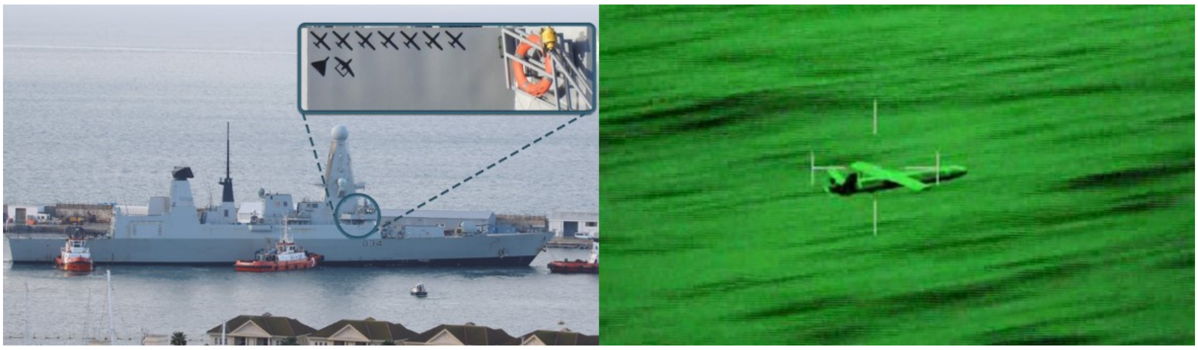

Figure 4: Left: Kill markings on Type 45 "HMS Diamond" after deployment in the Red Sea. Identified can be the Samad-2, Shahed-136 and Mersad-2. Image source: Forces.net [15] (X: @Michael J Sanchez key2med). Right: Screenshot of a French armed forces naval helicopter accompanying a FREMM frigate taking out a Houthi Samad-2 drone en-route to a commercial vessel in the Red Sea. Image source: EUNAVFOR ASPIDES [17] (X: @EUNAVFORASPIDES).

Besides low and slow flying drones (Samad-2) and low and fast-flying cruise missiles (C-802 Ghadir/Al-Mandab 2), the Houthis have also reportedly fired Short Range Ballistic Missiles (SRBMs) and Anti-Ship Ballistic Missiles (ASBMs) at commercial ships [3], [18]. Though from a kinematic point of view, the SM-2 Block IIIA could theoretically be deployed against Short Range Ballistic Missiles in a point-defence scenario, the SM-2 is not designed to take out these targets. Therefore, this thesis will not discuss intercept scenarios of SRBMs and ASBMs by the SM-2 Block IIIA. However, as the SM-2 is designed against high-altitude targets besides the aforementioned sea-skimming targets, it is desirable to characterize a high-altitude, high-speed target for the SM-2 to be deployed against. The Soviet-made AS-5 "Kelt" is chosen to be this target.

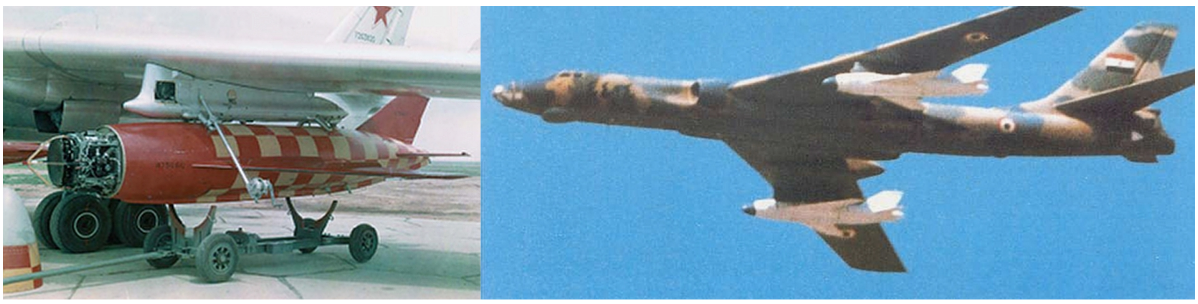

Figure 5: Left: Prototype AS-5 Kelt mounted on a prototype Tupolev Tu-16K-16 Badger G. Image source: Rus MoD (via [19]). Right: Tupolev Tu-16K-16 Badger G armed with two AS-5 Kelts. Image source: Carlo Kopp [19].

Protecting convoys and fleets by intercepting crossing targets in an area-defence scenario introduces greater complexity than defending against an incoming threat in a head-on point-defence scenario. In a point-defence scenario, an interceptor is fired in the direction of the incoming threat and the engagement geometry is constrained to the vertical manoeuvre plane only. The interceptor only needs to make manoeuvres in the vertical plane to intercept the incoming threat. Defending against crossing targets introduces large relative velocities in the horizontal manoeuvre plane, especially when the interceptor engages a threat (nearly) perpendicularly when viewed from above. The interceptor has to correct for errors and establish a collision course in both the vertical and horizontal manoeuvre plane. To fully characterize an interceptor's kinematic performance and ability to defend convoys and fleets, area-defence scenarios must be simulated.

Engagement envelopes show, for a specific defence scenario, what area around the launching ship can be protected by an interceptor. Threats are simulated to fly in a specific direction, and are engaged once they appear above the radar horizon. Figure 6 presents a schematic overview of a nominal engagement envelope. Engagement envelopes are critical for mission planners to optimize the deployment of the limited amount of guided-missile frigates and destroyers available in the Red Sea and Gulf of Aden, which can be tasked with protecting commercial shipping. Therefore, this thesis will focus on developing such engagement envelopes against the relevant Houthi threats.

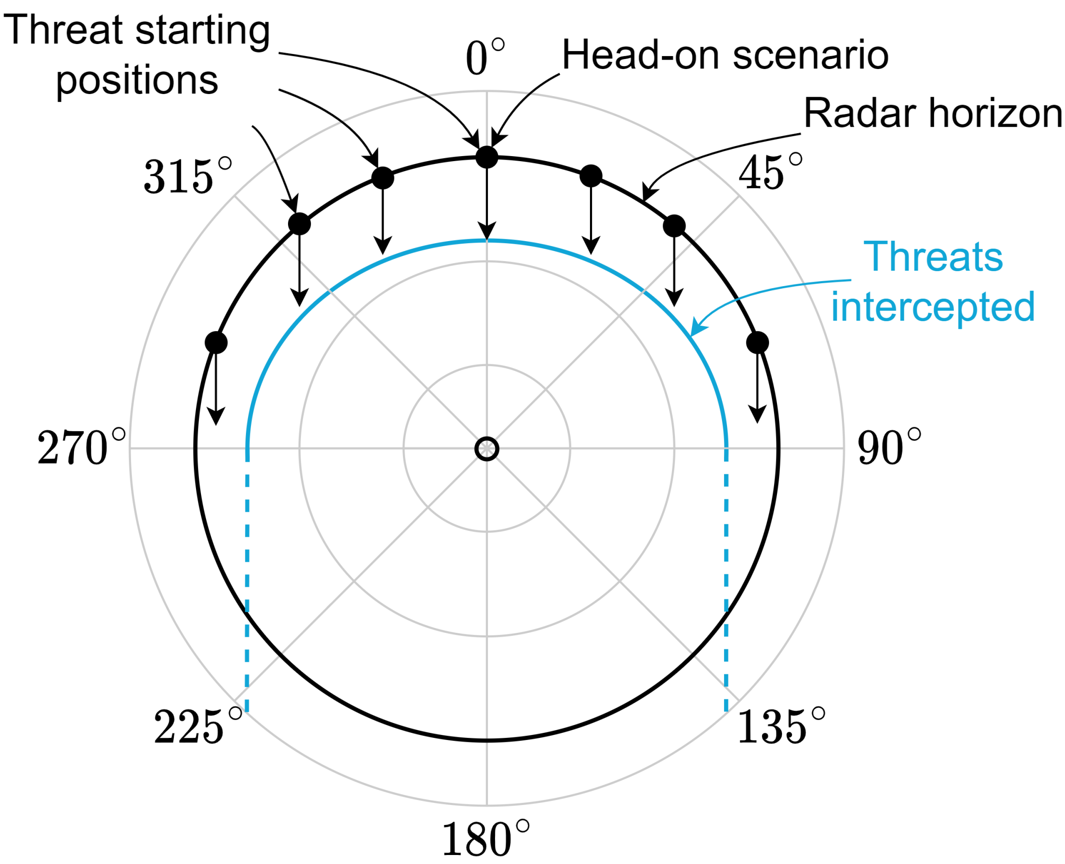

Figure 6: Schematic overview of an engagement envelope. Threats come in from the top of the figure, appearing on the Radar Horizon and fly "downward" (direction 180°)

1.1. Research objective and Research Questions

The objective of this report is to analyse the kinematic performance of the Standard Missile-2 Block IIIA and assess its suitability in protecting commercial shipping in the Red Sea and Gulf of Aden against Houthi threats. The kinematic performance of the SM-2 Block IIIA is derived from the missile's burnout velocity, its guidance methodology, and its maximum effective range and altitude. Assessing the interceptor's area-defence capabilities to protect commercial shipping is done by developing engagement envelopes against the Shahed-2 drone, Al-Mandab 2 version of the C-802 cruise missile, and Soviet-made AS-5 Kelt.

The research objective is formed into a research question and shall be:

"How well is the Standard Missile-2 Block IIIA suited kinematically for use in area defence to protect commercial shipping vessels against Houthi threats in the Red Sea and Gulf of Aden?"

With specific subquestions:

What is the protective envelope of the Standard Missile-2 Block IIIA when employed in area defence against crossing:

- ***low and slow flying targets, characterized by the Samad-2?***
- ***low and fast flying targets, characterized by the C-802 "Ghadir/Al-Mandab 2"?***
- ***high and fast flying targets, characterized by the AS-5 "Kelt"?***

Additional subquestions are:

- ***What guidance method(s) does the Standard Missile-2 Block IIIA employ to intercept flying targets?***
- ***What is the Standard Missile-2 Block IIIA's burnout velocity?***
- ***What is the Standard Missile-2 Block IIIA's maximum range?***
- ***What is the Standard Missile-2 Block IIIA's maximum effective altitude?***

1.2. Outline of the report

First, the methodology and the setup of the Simulink model are presented in section 2. The first two subsections present a general overview of a Surface-to-Air missile's flight phases and the guidance loop. Then, in subsection 2.3 to subsection 2.10, the report presents the quaternion transformation matrix, Kappa midcourse guidance, Proportional Navigation for terminal phase homing, the modified point mass equations of motion, modelling of forces, Primary Command Point calculation procedure, Simulink model block diagrams, and the verification of the Simulink model.

In section 3, the Standard Missile-2 itself and the threats modelled in this thesis are investigated. First, the interceptor properties, such as that of the MK104 Dual-Thrust Rocket Motor, internal layout, external geometry, and actuator properties are investigated. Then, the SM-2's time-varying mass, center of gravity, and moment of inertia are derived and modelled. An aerodynamic analysis of the SM-2 is performed and the modeled autopilot and airframe acceleration response section are presented. Finally, the relevant threats are investigated and modelled.

The important results that are directly linked to the research questions are presented in section 4. Flyout tables for each variant to the Kappa midcourse guidance mode are presented and the interceptor's kinematic performance metrics are derived. Then, engagement envelopes are shown against each threat type to assess the SM-2's area-defence capabilities.

Finally, conclusions are drawn and the research questions are answered. The results are interpreted and 'given sense'. At the very last, recommendations for future research are given.

2. Methodology and setup of Simulink model

2.1. Flight Phases

Figure 7 presents the phases of the SM2's flight. During the pre-launch phase, the ship's Fire Control System (FCS) initializes the ship-to-missile communication links and the missile is set to Aegis or Terrier/Tartar (2T) mode for compatibility with Fire Control Systems on different classes of ships [20]. Aegis mode allows the ship to send direct steering commands to the missile, whereas in 2T mode, the ship supplies the missile with a Primary Command Point (PCP), a point in space where the interceptor is expected to intercept the target and wehre the missile navigates to using its own navigation systems [20]. The Royal Netherlands Navy uses a form of 2T navigation, where the ship's Active Phased Arrar Radar (APAR) X-Band Multi-Function Radar (MFR) tracks and illuminates the target.

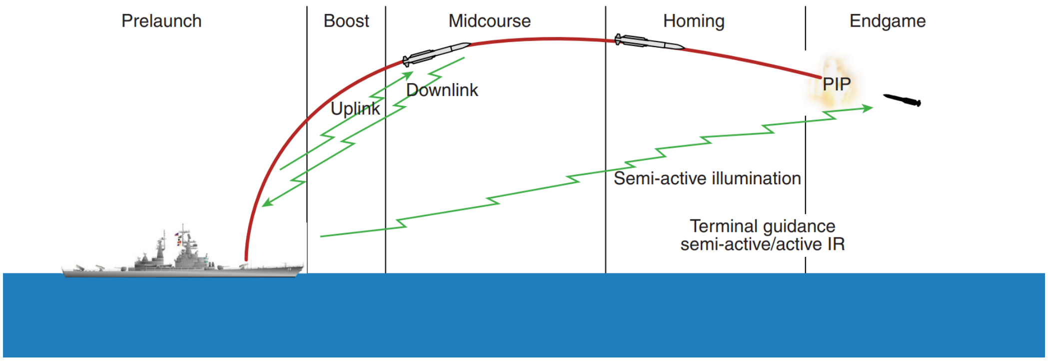

Figure 7: General overview of the flight phases of the SM-2 Block IIIA including pre-launch, boost, midcourse and terminal homing phases, as well as endgame kill assessment. The PIP (Predicted Intercept Point) in this figure is equivalent to the Primary Command Point (PCP) term used in this report. Image source: Cole Jr. [20].

During the boost phase, the missile's MK104 Dual-Thrust Rocket Motor (DTRM) is ignited and the missile accelerates vertically from the ship's Mark 41 Vertical Launching System (VLS). The MK104 has a boost-sustain thrust profile, generating a large thrust during the first few seconds of flight (boost), after which a smaller amount of thrust is produced for the remaining time until engine burnout (sustain phase). After 1 second of vertical flight, the missile starts a pitch-over manoeuvre and its guided flight to the PCP.

In 2T mode, during the midcourse phase, the missile uses its own Inertial Reference Unit (IRU) to fly towards the specified PCP using an Explicit Guidance guidance law [21] to optimize the initial engagement conditions for the terminal phase [22]. The ship supplies the missile with a new PCP if the newly calculated PCP were to become significantly different from the initial PCP [20], [21]. This could occur if the target changes course and/or speed [21].

Once the interceptor reaches the vicinity of the PCP, it switches to semi-active homing mode. The ship's APAR illuminates the target and the interceptor uses its on-board radar receiver to steer itself onto a collision course with the target [21].

2.2. Guidance Loop

Figure 8 presents a schematic overview of a general interceptor guidance loop [23]. External information, i.e. the target motion, is used as the input for the guidance loop. The missile seeker, the "target sensors" in this overview, sees the target in its own coordinate system (the Line-Of-Sight (LOS) coordinate system in subsection 2.5). In the real world, this information is noisy. Guidance filters, most often Kalman or alpha/beta filters are used to filter our the target motion and generate a smooth and accurate signal [23]. The measured relative target motion and the interceptor's own dynamics, measured by an on-board Inertial Reference Unit (IRU) in the "Inertial navigation" section, represent the engagement geometry and are fed into the guidance law section. A guidance law is applied to generate acceleration commands. The autopilot then takes the acceleration commands and translates these into aerodynamic control surface deflections to achieve the desired response. Interceptor information, such as velocity, altitude, time-varying mass and moments of inertia are also fed into the autopilot for appropriate gain scheduling. The resulting forces and moments, resulting in interceptor motion, are fed back to close the loop.

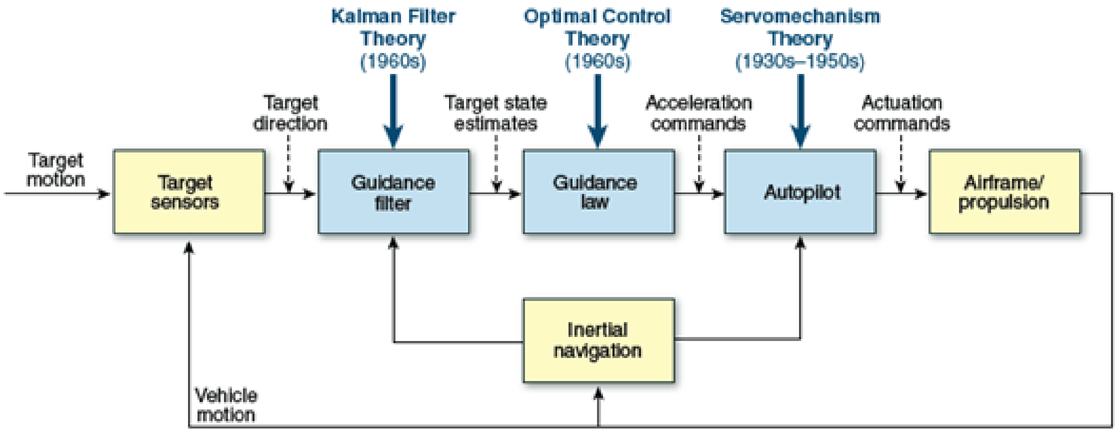

Figure 8: Simplified standard guidance loop consisting of a target sensor, guidance filter, guidance law, autopilot, accelerating airframe and an inertial navigation section [23].

2.3. Overview of Coordinate Frames

The kinematics of engagement scenarios are calculated in an inertial coordinate frame to calculate the acceleration-, velocity-, and position vectors of the interceptor and target. As multiple inertial coordinate frames exist, it should be mentioned what coordinate frames are used in this report.

Figure 9 presents the coordinate frames that are most used by the AIAA community [24], [25]. In this research, both the Launch-Centered Inertical Coordinate frame (LCIC frame) and Missile Body Coordinate frame (MBC frame) are used. The Eath-Centered Earth Fixed (ECEF) coordinate frame is not used due to the relative short intercept distances. However, the engagement geometry can easily be translated into ECEF coordinates to project the engagement geometry on an Earth model for visualisation purposes.

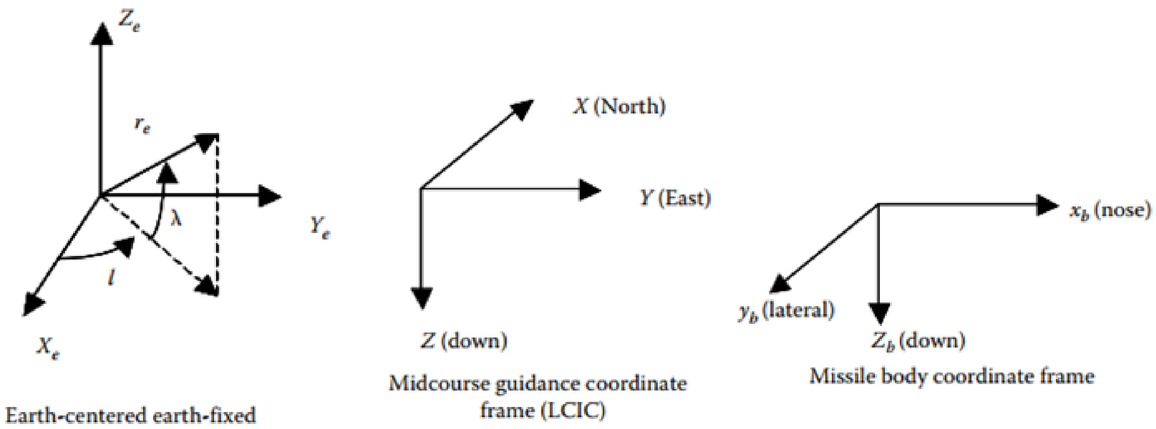

Figure 9: Coordinate Frames used in this research paper. The ECEF frame displays all geometry on an Earth model, the LCIC is the 'local' coordinate frame in which interceptions will be solved, the MBC frame is the frame in-line with the missile body and the SC frame is in-line with the missile seeker [24].

2.3.1. Coordinate frames used in this report

The designer of a missile interceptor simulation has to decide in what coordinate frame the engagement geometry and Equations of Motion (EoM's) are solved. Broadston recommends that for intercepts within ranges less than 200km, a Norh-East-Down (NED) coordinate frame is best suitable [26]. Boord and Hoffman recommend the use of the equivalent Launch-Centered Inertial Carthesian (LCIC) coordinate frame for midcourse guidance [24]. Since the SM-2 Surface-to-Air Missile (SAM) has a publicly reported maximum effective range of 167km [1] and most intercepts will occur well within this range, the LCIC coordinate frame will be used to solve the engagement kinematics in this research.

In the modified point mass simulations of this report, the missile's trajectory is calculated in the LCIC frame by solving the force equations, but not explicitly modelling the missile's yaw, pitch, and roll angles. The aerodynamic forces and propulsive are modelled in the local Missile Body Coordinate frame (MBC frame), resulting from the implicit angles of attack and sideslip that are required to obtain the commanded accelerations. In modified point mass simulations, the Missile Body Coordinate frame (MBC frame) is constructed originating from the velocity vector, where the local X-axis is aligned with the velocity vector and the local Y- and Z-axes point to the 'right' and 'down'. The forces acting in the MBC frame are translated to the LCIC by means of a coordinate transformation step, as explained in subsubsection 2.3.3 and subsubsection 2.3.4. Figure 10 presents the LCIC frame and how the MBC frame is positioned in the LCIC frame.

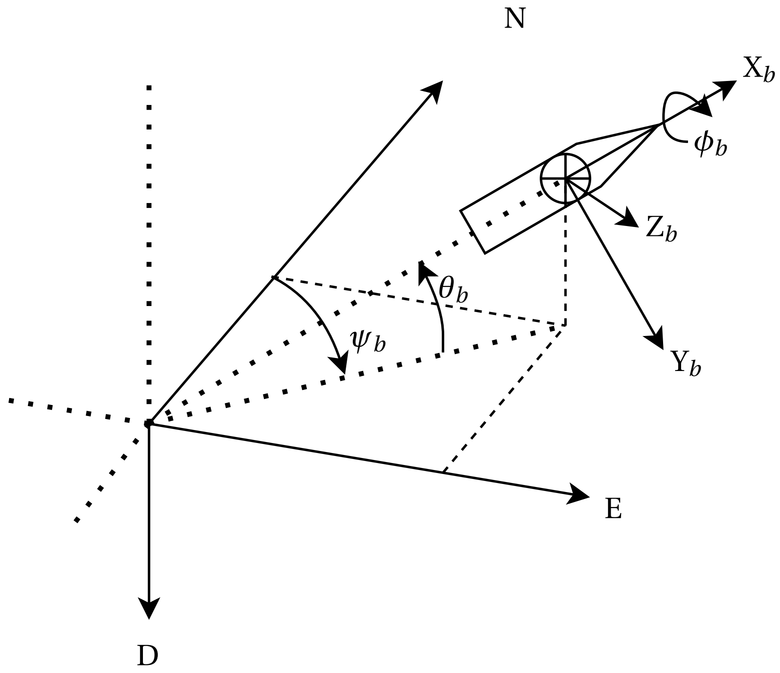

Figure 10: Visualization of the LCIC and MBC coordinate frames. The LCIC coordinate frame points North, East, and down. The MBC frame originates from the interceptor's center of gravity and is constructed 'forward', 'right' and 'down' with respect to the interceptor's roll axis. The MBC frame is oriented with respect to the LCIC frame by the roll, pitch, and yaw angles ϕ, θ, and ψ.

Acceleration commands generated by the guidance section are either given with respect to the Line of Sight (LOS) in the case of Proportional Navigation (see subsection 2.5), or are directly given in the MBC frame, as is the case for Kappa guidance during the midcourse phase (see subsection 2.4). When acceleration commands are given with respect to the LOS, the acceleration commands are translated to the MBC frame by applying the LOS-to-MBC transformation matrix found in Equation 15. The acceleration commands in the MBC frame are used as inputs to the autopilot, explained in subsection 3.4, which models the 'real' second-order acceleration response and approximates it by a first-order transfer function. The resulting first-order acceleration response in the MBC frame is then translated to the LCIC frame through the quaternion rotation matrix given by Equation 8.

2.3.2. Coordinate frames in 6 Degrees of Freedom simulations

In 6-DOF simulations, the missile's three translational and three rotational degrees of freedom are all explicitly modelled. The missile's state vector is thus described by its position, velocity, and acceleration in the inertial frame, its Euler angles that orient the MBC frame with respect to the LCIC frame and their time derivatives, and the local velocities and rotational velocities and accelerations in the MBC frame. The Missile Body Coordinate (MBC) frame originates at the missile's center of mass and has its x-axis pointed along the missile's longitudinal axis, towards its nose [24]. The Y- and Z-axes point to the 'right' and 'down', respectively, making the MBC frame a right-handed coordinate frame.

2.3.3. Transformation matrix

To translate vectors from the LCIC frame to the MBC frame, the LCIC-MBC transformation matrix described by Equation 1 is used [24], [27].

$$[A]_{LCIC}^{MBC} = \begin{bmatrix} c(\theta_b)c(\psi_b) & c(\theta_b)s(\psi_b) & -s(\theta_b) \\ \begin{matrix} s(\phi_b)s(\theta_b)c(\psi_b)- \\ c(\phi_b)s(\psi_b) \end{matrix} & \begin{matrix} s(\phi_b)s(\theta_b)s(\psi_b)+ \\ c(\phi_b)c(\psi_b) \end{matrix} & s(\phi_b)c(\theta_b) \\ \begin{matrix} c(\phi_b)s(\theta_b)c(\psi_b)+ \\ s(\phi_b)s(\psi_b) \end{matrix} & \begin{matrix} c(\phi_b)s(\theta_b)s(\psi_b)- \\ s(\phi_b)c(\psi_b) \end{matrix} & c(\phi_b)c(\theta_b) \end{bmatrix}, \tag{1}$$

where c is short for the cosine operator and s is short for the sine operator. ψ_b is the missile body yaw (azimuth) angle with respect to the LCIC frame, θ_b the pitch angle and ϕ_b is the roll angle.

To transform from the MBC to the LCIC frame, the transpose of the transformation matrix is applied, as the transformation matrix is orthogonal [24].

2.3.4. Quaternions

Euler angles are usually an effective method to describe the attitude of aircraft and missiles in modified point mass and 6-DOF simulations. Euler angles allow for relatively fast calculations and an intuitive geometrical interpretation. However, a mathematical singularity occurs in Euler angle notation when the vehicle's orientation is vertical with respect to the inertial horizon ($\theta = 90°$) [28]. Because the SM-2 is launched vertically, this would be the case for the present thesis. Therefore, it is decided to describe the rotation matrix using quaternions. To implement the quaternion method, the derivation methodology according to Armesto [29] is followed.

First, the rotation vectors $\boldsymbol{q}_x(\phi)$, $\boldsymbol{q}_y(\theta)$, and $\boldsymbol{q}_z(\psi)$ are defined by

$$\boldsymbol{q}_x(\phi) = \begin{bmatrix} \cos\left(\frac{\phi}{2}\right) \\ \sin\left(\frac{\phi}{2}\right) \\ 0 \\ 0 \end{bmatrix}, \tag{2}$$

$$\boldsymbol{q}_y(\theta) = \begin{bmatrix} \cos\left(\frac{\theta}{2}\right) \\ 0 \\ \sin\left(\frac{\theta}{2}\right) \\ 0 \end{bmatrix}, \tag{3}$$

and

$$\boldsymbol{q}_z(\psi) = \begin{bmatrix} \cos\left(\frac{\psi}{2}\right) \\ 0 \\ 0 \\ \sin\left(\frac{\psi}{2}\right) \end{bmatrix}, \tag{4}$$

with ϕ, θ, and ψ the interceptor's roll, pitch, and yaw angles, respectively. The rotation vectors are later used to construct the quaternion, $\boldsymbol{q}$. The rotation vectors $\boldsymbol{q}_x$, $\boldsymbol{q}_y$, and $\boldsymbol{q}_z$ are now multiplied by

$$\mathbf{q} = \boldsymbol{q}_z(\psi) \odot \boldsymbol{q}_y(\theta) \odot \boldsymbol{q}_x(\phi), \tag{5}$$

in order to construct the quaternion $\mathbf{q}$, which in turn is used to construct the MBC frame-to-LCIC quaternion rotation matrix, $Q_{LCIC}^{MBCframe}$. The multiplication operation $\boldsymbol{q}_1 \odot \boldsymbol{q}_2$ between two vectors $\boldsymbol{q}_1 = [q_{1,w}, q_{1,x}, q_{1,y}, q_{1,z}]^T$ and $\boldsymbol{q}_2 = [q_{2,w}, q_{2,x}, q_{2,y}, q_{2,z}]^T$ is defined using by [29]:

$$\boldsymbol{q}_1 \odot \boldsymbol{q}_2 = \begin{bmatrix} q_{1,w}q_{2,w} - q_{1,x}q_{2,x} - q_{1,y}q_{2,y} - q_{1,z}q_{2,z} \\ q_{1,w}q_{2,x} + q_{1,x}q_{2,w} + q_{1,y}q_{2,z} - q_{1,z}q_{2,y} \\ q_{1,w}q_{2,y} - q_{1,x}q_{2,z} + q_{1,y}q_{2,w} + q_{1,z}q_{2,x} \\ q_{1,w}q_{2,z} + q_{1,x}q_{2,y} - q_{1,y}q_{2,x} + q_{1,z}q_{2,w} \end{bmatrix}. \tag{6}$$

After the two vector multiplication operations, $\boldsymbol{q}_z(\psi) \odot \boldsymbol{q}_y(\theta)$ and $\left(\boldsymbol{q}_z(\psi) \odot \boldsymbol{q}_y(\theta)\right) \odot \boldsymbol{q}_x(\phi)$, the resulting quaternion $\boldsymbol{q}$ is obtained [29]:

$$\mathbf{q} = \begin{bmatrix} q_w \\ q_x \\ q_y \\ q_z \end{bmatrix}. \tag{7}$$

Finally, the quaternion rotation matrix $Q_{MBCframe}^{LCIC}$ is constructed by [29]:

$$[Q]_{MBCframe}^{LCIC} = \begin{bmatrix} 1 - 2q_y^2 - 2q_z^2 & 2q_xq_y - 2q_zq_w & 2q_xq_z + 2q_yq_w \\ 2q_xq_y + 2q_zq_w & 1 - 2q_x^2 - 2q_z^2 & 2q_yq_z - 2q_xq_w \\ 2q_xq_z - 2q_yq_w & 2q_yq_z + 2q_xq_w & 1 - 2q_x^2 - 2q_y^2 \end{bmatrix} \tag{8}$$

2.4. Midcourse Guidance: Explicit Guidance

The goal of a midcourse guidance law is to generate acceleration commands for the interceptor to steer itself to a calculated PCP along a trajectory that improves the energy at impact, compared to trying to intercept a target by flying to the PCP in a straight line. The SM-2 set to T2 mode uses the Explicit Guidance midcourse guidance law [21]. Explicit Guidance is a form of Optimal Control where the solution to a cost function, consisting of multiple weighted objectives, is calculated. Not only is the missile guided to the PCP, but a terminal intercept angle can also be specified [21], [24], [30]. The guidance law will thus try to shape the intercept course such that the missile flies through the PCP at the given intercept angle. Trajectory shaping is typically performed only in the vertical plane [24], with the horizontal path from the launcher to the PCP being a straight line.

2.4.1. Explicit Guidance acceleration commands

Ohlmeyer and Phillips [31] have developed a form of the Explicit Guidance navigation kown as Generalized Explicit Guidance (GENEX). Explicit Guidance may also be known as 'Kappa guidance' [32], [33], [34]. Lin [30], Zarchan [32] and Serakos and Lin [33] propose solutions to the Kappa guidance principle. Boord and Hoffman [24] further consider Lin's solution to the Kappa guidance law in their Book. Equation 9 shows Lin's solution to the Kappa guidance law, as developed by Lin and presented by Boord and Hoffman [24], [30]:

$$\mathbf{a}_c^{LCIC} = \frac{K_1}{T_{go}^2}[\mathbf{R}_{PCP} - \mathbf{R}_M - \mathbf{V}_M T_{go}] + \frac{K_2}{T_{go}}[\mathbf{V}_{MF} - \mathbf{V}_M], \tag{9}$$

where $\mathbf{a}_c$ is the commanded acceleration vector in LCIC coordinates, K_1 and K_2 are time-varied weighing factors which are further discussed in subsubsection 2.4.3 [30]. T_{go} is the time-to-go and is approximated using a time-to-go approximation algorithm, as the interceptor's velocity varies greatly along the trajectory to the PCP, which itself is not a straight line. The time-to-go is approximated in appendix A.1 due to its lengthy derivation. $\mathbf{R}_{PCP}$ is the range vector from the LCIC frame origin to the PCP, $\mathbf{R}_M$ is is the range vector from the LCIC frame origin to the missile c.g., $\mathbf{V}_M$ is the current missile velocity vector, and $\mathbf{V}_{MF}$ is the estimated missile velocity vector at the PCP. It is the product of the specified interception direction unit vector $\mathbf{i}_{MF}$ and the estimated missile velocity at the PCP, V_{MF}, which is estimated in appendix A.2.

Figure 11 presents an example of an arbitrary interceptor's resulting flyout trajectories towards specified PCP's, following the implementation of the Kappa guidance law as presented by Boord and Hoffman [24]. Boord and Hoffman recommend intercepting low flying (< 10km) targets such as cruise missiles at a ground angle of 75 degrees, which is "appropriate for a cruise missile defense strategy" [24]. Intercepting terminal phase ballistic missiles should occur at a local ground angle of 45 degrees [24]. However, the designer is free to specify his or her own terminal intercept angle.

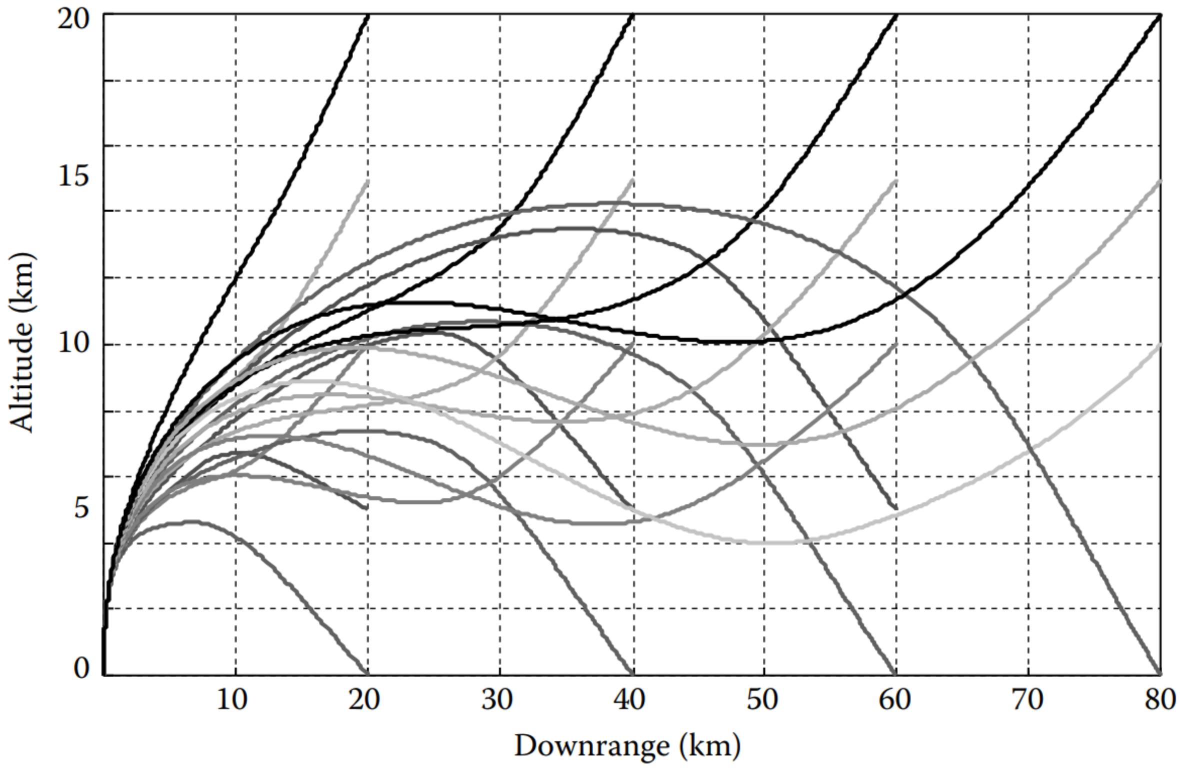

Figure 11: Example of interceptor flyout geometries using Kappa guidance [24] for an arbitrary interceptor. Targets below 10km altitude are set to be intercepted at an absolute ground angle of 75 degrees. Targets at or above 10km altitude are set to be intercepted at a ground angle of 45 degrees. The missile launch occurs vertically.

2.4.2. Simplified calculation of acceleration commands

Lin, together with Serakos, later published a closed-form solution to the Kappa Guidance principle, in which the calculated acceleration commands are now independent of the time-to-go, T_{go}, and the estimated velocity vector at the PCP, $\mathbf{V}_{MF}$. Boord and Hoffman state that the performance of the closed-form formulation is close to the performance of the full methodology that includes the time-to-go and estimated final velocity vector at the PCP [24]. Equation 10 presents the closed-form formulation for the acceleration command normal to the velocity vector in the vertical plane [24]:

$$a_c = -\frac{K_1}{R_{MPCP}}\left[V_M^2 \sin(\delta)\right] + \frac{K_2}{R_{MPCP}}\left[V_M^2 \sin(\mu)\cos(\delta)\right] \tag{10}$$

where a_c is now the acceleration command normal to the interceptor's velocity vector in the vertical plane at a given timestep, R_{MPCP} is the range from the interceptor's current position to the PCP, δ is the angular deviation from the collision course in the vertical plane (the angular error between the interceptor velocity vector and interceptor-to-PCP line of sight) and μ is the angular deviation between the current velocity vector and the specified terminal intercept angle at the PCP in the vertical plane [24]. Figure 12 visually shows the definitions of δ and μ.

In Equation 10, only the specified vertical terminal intercept angle at the PCP is required. Though less advanced than Equation 9, which implements T_{go} and V_{MF} estimations found in appendix A.1 and appendix A.2, Equation 10 may be more approximate to the midcourse guidance algorithm implemented on board the SM-2 Block IIIA, given the age of the SM-2 Block IIIA and due to Equation 10's simplicity, robustness, lower computational costs and absence of the advanced T_{go} and V_{MF} estimations that were only developed since the 2000's.

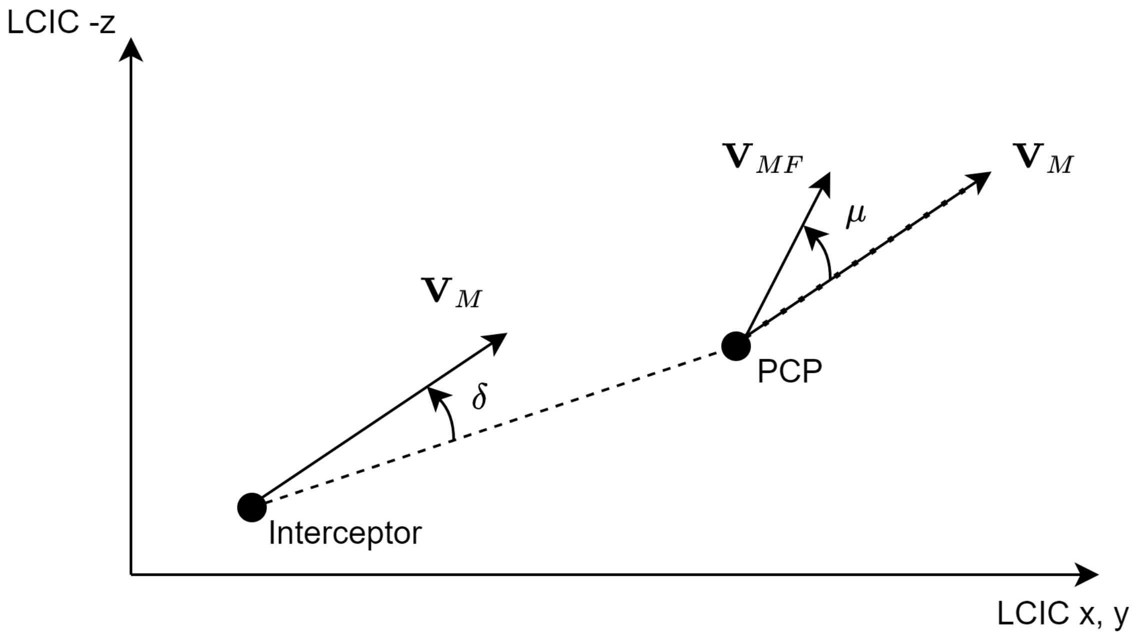

Figure 12: Midcourse guidance geometry specifying the definitions of δ and μ in the LCIC frame

As the interceptor is fired towards the PCP with a constant heading angle over the whole trajectory, no steering commands in the horizontal engagement plane are expected. In real life, the interceptor needs to compensate for wind loads steering the interceptor off-course. In a perfect simulation environment, no such wind loads exist. Regardless, for completeness, a horizontal steering command equation is implemented. One can implement Equation 10 in the horizontal plane, or implement a Proportional Navigation scheme. In this report, Proportional Navigation is implemented for horizontal-plane guidance. Proportional Navigation will be discussed in detail in subsection 2.5.

2.4.3. Calculating K_1 and K_2

The weighing factors K_1 and K_2 are time-varying functions of the magnitude of the interceptor-to-PCP range and the trajectory-shaping coefficient ω, which is presented Equation 11 and Equation 12. The equations for calculating K_1 and K_2 change depending on whether the generated thrust is larger or smaller than the zero-lift drag force and whether a terminal intercept angle is specified or not. The four cases for calculating K_1 and K_2 are:

- Case 1: Thrust smaller than or equal to zero-lift drag, with a specified intercept angle at the PCP
- Case 2: Thrust smaller than or equal to zero-lift drag, no specified intercept angle at the PCP
- Case 3: Thrust larger than zero-lift drag, with a specified intercept angle at the PCP
- Case 4: Thrust larger than zero-lift drag, no specified intercept angle at the PCP

For each case, Lin covers the complete mathematical derivations for the optimal equations for K_1 and K_2 [30]. Only the resulting equations are presented here. The reader is referred to Lin [30] for the full mathematical derivations. Table 1 describes the equations for calculating K_1 and K_2 for the four cases:

$T <= D_0$, with angle	$K_1 = \dfrac{2\omega^2 R_{MPCP}^2 - \omega R_{MPCP}(e^{\omega R_{MPCP}} - e^{-\omega R_{MPCP}})}{e^{\omega R_{MPCP}}(\omega R_{MPCP} - 2) - e^{-\omega R_{MPCP}}(\omega R_{MPCP} + 2) + 4}$
	$K_2 = \dfrac{\omega^2 R_{MPCP}^2 (e^{\omega R_{MPCP}} + e^{-\omega R_{MPCP}} - 2)}{e^{\omega R_{MPCP}}(\omega R_{MPCP} - 2) - e^{-\omega R_{MPCP}}(\omega R_{MPCP} + 2) + 4}$
$T <= D_0$, no angle	$K_1 = 0$
	$K_2 = \dfrac{\omega^2 R_{MPCP}^2 (e^{\omega R_{MPCP}} + e^{-\omega R_{MPCP}})}{e^{\omega R_{MPCP}}(\omega R_{MPCP} - 1) + e^{-\omega R_{MPCP}}(\omega R_{MPCP} + 1)}$
$T > D_0$, with angle	$K_1 = \dfrac{\omega R_{MPCP}(sin(\omega R_{MPCP}) - \omega R_{MPCP})}{2 - 2\cos(\omega R_{MPCP}) - \omega R_{MPCP}\sin(\omega R_{MPCP})}$
	$K_2 = \dfrac{\omega^2 R_{MPCP}^2 (1 - \cos(\omega R_{MPCP})}{2 - 2\cos(\omega R_{MPCP}) - \omega R_{MPCP}\sin(\omega R_{MPCP})}$
$T > D_0$, no angle	$K_1 = 0$
	$K_2 = \dfrac{\omega^2 R_{MPCP}^2 \sin(\omega R_{MPCP})}{\sin(\omega R_{MPCP}) - \omega R_{MPCP}\cos(\omega R_{MPCP})}$

Table 1: Equations for calculating K_1 and K_2 for four scenario's. T is the thrust force, D_0 is the zero-lift drag force, R_{MPCP} is the interceptor-to-PCP range, and ω is a trajectory-shaping coefficient

In Table 1, T is the generated thrust force, D_0 is the zero-lift drag force, R_{MPCP} is the magnitude of the interceptor-to-PCP range, and ω is a time-varying trajectory-shaping coefficient and is "known as the trajectory-shaping coefficient and is a first-order function of the aerodynamic and propulsive forces in that plane when attempting to minimize energy loss for a missile flight" [24]. The coefficient ω does not depend on the terminal intercept angle, but two different equations are used depending on whether the thrust is larger or smaller than the zero-lift drag:

- **Case 1: Thrust smaller than drag**

In the case where the generated thrust is smaller than the zero-lift drag, ω is calculated using Equation 11 [30]:

$$\omega^2 = \frac{D_0 L_\alpha \left(\frac{T}{L_\alpha} + 1\right)^2}{m^2 V_M^4 \left(2\eta + \frac{T}{L_\alpha}\right)}, \tag{11}$$

- **Case 2: Thrust larger than drag**

In the case where the generated thrust force is larger than the zero-lift drag, ω is calculated using Equation 12 [30]:

$$\omega^2 = \frac{L_\alpha (D_0 - T) \left(\frac{T}{L_\alpha} + 1\right)^2}{m^2 V_M^4 \left(2\eta + \frac{T}{L_\alpha}\right)} \tag{12}$$

In these equations, D_0 is the zero-lift drag force, L_α is the lift-curve slope, V_M is the missile velocity magnitude, η is an aerodynamic efficiency factor that can be determined empirically, or set to 1 in case of a simplified model, C_{L_α} is the dimensionless lift-curve slope, T is the time-varying thrust force and m is the time-varying missile mass [24].

2.4.4. Gravity compensation

The total acceleration command normal to the velocity vector in the vertical frame is calculated by adding a gravity compensation term to the Kappa midcourse acceleration command, defined in Equation 9 or Equation 10 [30]. Implementing the gravity compensation term can be done simply by taking the cosine of the missile's pitch angle θ (which in a modified point mass simulation is equivalent to the vertical flight path angle γ_v), thus:

$$\boldsymbol{g}_{comp}^{MBCF} = -g \cdot \begin{bmatrix} 0 \\ 0 \\ \cos(\theta) \end{bmatrix} \tag{13}$$

2.4.5. Maximum acceleration command limit

To optimize kinematic performance and minimize the total energy bleed due to drag along an intercept trajectory, it may be desirable for the interceptor to fly at higher altitudes.

Therefore, large lateral accelerations at the start of flight should be prevented, thus resulting in a slower pitch-over manoeuvre. The interceptor's kinematic performance is thus improved by setting a limit to the maximum allowed acceleration command generated by the midcourse Kappa guidance. Limiting the maximum pitch-over manoeuvre, however, does increase the minimum distance at which the interceptor can intercept targets. However, for very short range intercepts, short-range Surface-to-Air missiles such as the Evolved Sea Sparrow Missile (ESSM) or the point-defence Close-In Weapon System (CIWS) are utilized, allowing the Standard Missile family of SAM's to be kinematically optimized for medium to long range intercepts. The maximum acceleration command limit in the Simulink model is set to 10 g's for the first 20 seconds of flight.

An overall maximum acceleration command limit of 45 g's is given to prevent overstressing of the airframe. No open-source information could be found on the maximum g-force that the Standard Missile-2 Block IIIA is designed for. However, in consultation with the thesis supervisor, a value of 45 g's was chosen.

2.4.6. Long-Range Midcourse Guidance variant

In subsection 4.1, the Kappa guidance midcourse guidance algorithm is seen to give the SM-2 Block IIIA a maximum effective range of 83 km, falling short of the publicly reported maximum range of 167 km [35], [1]. The Standard Missile-2 Block IIIA is either kinematically unable to reach the reported 167km, or the implemented guidance algorithm limits the maximum range of the interceptor. To to able to fly very long ranges, the trajectory should be shaped such that the interceptor spends most of its trajectory in the very high atmosphere to minimize total energy bleed due to drag.

A simple modification to the Kappa midcourse guidance algorithm was implemented to first force the interceptor into the very high regions of the atmosphere before being guided towards a specified PCP. In this 'long-range mode', a constant pitch-over acceleration command of 3 g is given during the first 25 seconds of flight. The result is a gradual pitch-over manoeuvre that brings the missile to an altitude of 18.1 kilometers at a downrange position of 12.9 kilometers, as can be observed in Figure 45 and Figure 46, after which Kappa guidance is again used to guide the interceptor towards the specified PCP.

In subsection 4.1, flyout tables are also presented for the long-range Kappa guidance mode. The long-range Kappa guidance mode with no specified intercept angle achieves a maximum ground range of 173 km, very closely agreeing with the publicly reported maximum range of 167 km.

2.5. Terminal Guidance: Proportional Navigation

After the Standard Missile-2 has flown to the vicinity of the PCP using Kappa guidance, the interceptor enters the terminal homing phase (see Figure 7). Once the range from the interceptor to target is sufficiently small for the on-board radar receiver to detect the target, the guidance loop (see Figure 8) is activated and the interceptor is guided towards a collission course with the target using Proportional Navigation.

Proportional Navigation (PN) was first developed in the 1940's [24] and it and its variations are still the most widely used interceptor guidance laws to date. Over the years, variations of PN have been developed to add functionalities to the guidance law, including compensation factors for gravity and interceptor- and target accelerations. Due to increases in computational power, more complex guidance laws are developed and implemented, resulting in Proportional Navigation becoming dated. Regardless, PN remains a stable and robust guidance law with excellent intercept performance, especially when preceded by a proper midcourse guidance law that optimizes the initial conditions of the terminal homing phase. There may exist guidance laws that outperform PN under specific conditions, but they are often optimized only for those specific conditions [23]. Palumbo and Ross comment: "if the derivation assumptions become too specific, the resulting guidance law may work well if those assumptions actually hold, but performance might rapidly degrade as reality deviates from the assumptions" [23].

Figure 13 presents a schematic overview of a planar (two-dimensional) engagement geometry with respect to an inertial frame. Simplifying a complex three-dimensional engagement geometry into two uncoupled planar representations greatly simplifies the problem mathematically without diminishing performance. Most modern guidance law implementations use this approach [23].

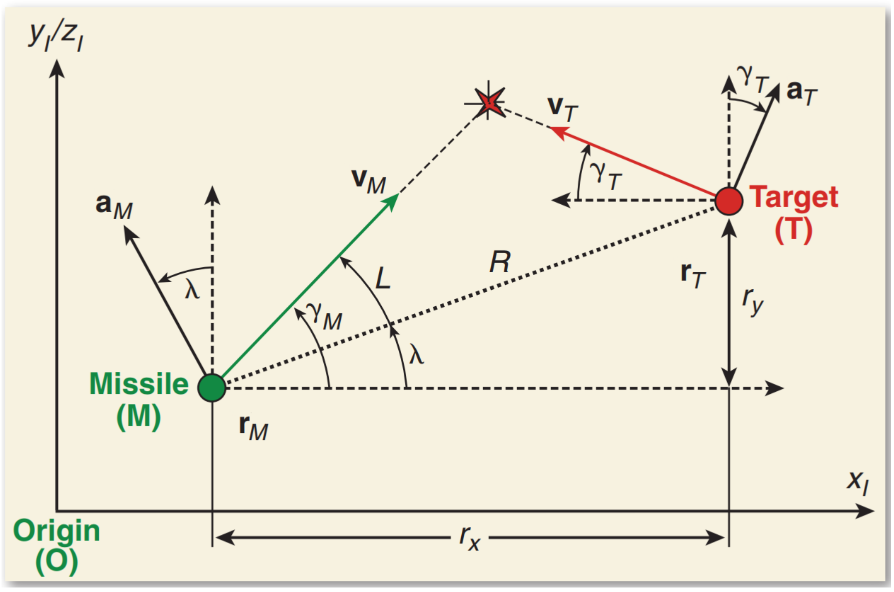

Figure 13: Planar interception geometry overview [23]

In Figure 13, γ_M is the missile flight path angle, γ_T is the target flight path angle, λ is the LOS angle, $\mathbf{r}_M$ is the missile inertial position vector, $\mathbf{r}_T$ is the target inertial position vector, $\mathbf{v}_M$ is the missile velocity vector, $\mathbf{v}_T$ is the target velocity vector, $\mathbf{a}_M$ is the missile acceleration normal to the LOS in the LCIC frame, $\mathbf{a}_T$ is the target acceleration normal to $\mathbf{v}_T$, L is the lead angle, r_x is the relative position in x-direction, r_y is the relative position in y direction and R is the range to the target [23].

PN aims the interceptor velocity vector in each plane such that, when added to the target velocity vector, the relative velocity vector between the interceptor and target is purely along the missile-to-target Line-Of-Sight (LOS) vector. The interceptor is on a direct collision course when the LOS angle does not change. A relative velocity that is not directly in line with the missile-to-target LOS has a component perpendicular to the LOS, thus resulting in an angular velocity of the measured LOS. This angular LOS velocity is used to compute the acceleration commands that realign the relative velocity to the LOS vector.

2.5.1. PN Acceleration command equations

Equation 14 presents the Proportional Navigation acceleration commands in the LOS frame:

$$\mathbf{a}_c^{LOS} = N' V_C \dot{\boldsymbol{\lambda}}, \tag{14}$$

where $\mathbf{a}_c^{LOS}$ is the acceleration command vector in the Line of Sight frame, N' is the navigation constant, V_C is the closing velocity and $\dot{\boldsymbol{\lambda}}$ holds the measured angular velocities of the LOS vector in the LCIC frame.

To obtain the acceleration command perpendicular to the MBC frame (which in a modified point mass simulation aligns with the velocity frame), a rotation matrix from the LOS frame to the MBC frame is applied:

$$T_{LOS}^{MBCF} = \begin{bmatrix} 0 & sin(L_{NE}) & cos(L_{NE})sin(L_v) \\ 0 & cos(L_{NE}) & sin(L_{NE})sin(L_v) \\ 0 & 0 & cos(L_v), \end{bmatrix} \tag{15}$$

where L_{NE} is the lead angle in the horizontal (North-East) plane and L_v is the lead angle in the vertical plane. Attention is called on the zeros in the first column. As the interceptor cannot throttle its thrust, the acceleration command in the MBC frame's x-direction is set to zero. In Equation 15, the acceleration command in MBC frame's x-direction is therefore not calculated.

The acceleration command vector in the MBC frame can now be calculated by multiplying the LOS-to-MBCF rotation matrix by the acceleration command vector with respect to the LOS frame, given by:

$$\boldsymbol{a}_c^{MBCF} = T_{LOS}^{MBCF} \cdot \boldsymbol{a}_c^{LOS}. \tag{16}$$

2.5.2. Values for the Navigation Gain N'

For interceptors, N' is usually between 3 and 5, depending on the type of target the missile is designed for. Deriving the Optimal Control equations and solving for minimum control effort, the optimal value of N' is found to be $N' = 3$ [34]. However, for manoeuvring targets, a navigation gain of $N' = 3$ may be insufficient to keep up with target manoeuvres, potentially resulting in a miss. Therefore, navigation gains of $N' = 4$ or $N' = 5$ are often used when intercepting manoeuvring targets. It is up to the missile designer to make a trade-off between minimizing energy expenditure and maximizing manoeuvrability. Variations on PN may incorporate a time-varying navigation gain scheme to minimize energy loss during the initial phase, while simultaneously allowing the missile to make sharp turns during terminal homing.

A separate midcourse guidance law may also replace the need for a time-varying Proportional Navigation scheme. During the midcourse flight phase, replacing PN with a navigation gain of $N' = 3$ by a dedicated midcourse guidance law may improve overall intercept performance by shaping the trajectory to optimize for desired intercept performance parameters, such as impact velocity or minimum time-to-intercept. In this report, Explicit Guidance, as explained in subsection 2.4, guides the missile towards an intercept course at a predefined intercept angle. PN with a high navigation gain, such as $N' = 5$, can then be used in the terminal homing phase to maximize interceptor accelerations, to allow for interception of manoeuvring targets.

2.5.3. Augmented Proportional Navigation

Augmented Proportional Navigation (APN) aims to improve some of Proportional Navigation's shortcomings. PN works best if the target velocity is constant. In that case, an initial lateral acceleration will quickly lead to the interceptor flying on a collision course with the LOS angle λ becoming constant. PN can deal with manoeuvring targets, whose movement results in a LOS angle rate, $\dot{\lambda}$, which is used as an input in Equation 14 to calculate the interceptor's acceleration commands.

Augmented Proportional Navigation (APN) expands on PN by including both interceptor and target acceleration. Augmented PN is "a simplification of an optimal guidance law that accounts for both target manoeuvre and missile dynamics" [26]. Provided that the missile's on-board seeker can measure target accelerations, APN can thus generate acceleration commands using the relative position, relative velocity, and target and interceptor accelerations [26]. Advanced filters such as Extended Kalman Filter or an Alpha-Beta-Gamma filter may provide sufficiently accurate target acceleration values [30], [34].

Modifying the original PN equation (given by Equation 14) to compensate for gravity and interceptor drag effects projected into the LOS plane results in "compensated PN" [34], [36] and is given by Equation 17 [34].

$$\mathbf{a}_c^{MBCF} = T_{LOS}^{MBCF} \cdot \left(N' V_C \dot{\boldsymbol{\lambda}} - \mathbf{a}_{long}^{LOS} \right) - \frac{N'}{2} \mathbf{g}^{MBCF}, \tag{17}$$

where $\mathbf{a}_c^{LOS}$ holds the acceleration command vector in the LOS frame, T_{LOS}^{MBCF} is the LOS-to-MBCF transformation matrix given by Equation 15, N' is the navigation gain, $\dot{\boldsymbol{\lambda}}$ holds the angular velocities of the LOS vector, $\mathbf{a}_{long}$ is the interceptor's longitudinal acceleration projected into the LOS plane, which is the sum of the missile's thrust and drag, and $\mathbf{g}^{MBCF}$ is the gravity vector in the MBC frame.

Further adding the target manoeuvring dynamics results in a full Augmented Proportional Navigation scheme. Equation 18 gives Lucacs and Yakimenko's APN acceleration commands equation that holds into account the LOS rate, target acceleration, interceptor acceleration, and gravity [34]. Equation 18 is rewritten symbolically from its original form to remain consistent with the symbols used in this work.

$$\mathbf{a}_c^{MBCF} = T_{LOS}^{MBCF} \cdot \left(N' V_C \dot{\boldsymbol{\lambda}} + \frac{N'}{2} \mathbf{a}_T^{LOS} - \mathbf{a}_{long}^{LOS} \right) - \frac{N'}{2} \mathbf{g}^{MBCF}, \tag{18}$$

where $\mathbf{a}_T^{LOS}$ is the target acceleration vector projected into the LOS plane.

Because APN is able to take into account interceptor and target accelerations, the navigation gain does not need to remain $N' = 5$ to keep up with target manoeuvres. The navigation gain can be set back to $N' = 3$ to comply with minimum control effort optimality [34] and maximize kinetic energy at intercept.

2.5.4. PN scheme used in this report

As the aim of this report is to construct engagement envelopes against non- (or barely) manoeuvring targets, a relatively simple Proportional Navigation scheme with gravity compensation is implemented in this report. Equation 19 presents the Proportional Navigation scheme implemented in this report:

$$\boldsymbol{a}_c^{MBCF} = T_{LOS}^{MBCF} \cdot \left(N' V_C \dot{\boldsymbol{\lambda}} \right) - \frac{N'}{2} \mathbf{g}^{MBCF} \tag{19}$$

2.5.5. PN maximum acceleration command

As is the case for Kappa guidance (see subsubsection 2.4.5), the Proportional Navigation guidance acceleration command is limited to a maximum of 45 g's to prevent overstressing of the airframe.

2.6. Equations of Motion in modified point mass simulations

As mentioned in subsection 2.3, a modified point mass model is used to solve the kinematic equations in the Launch-Centered Inertial Coordinate Frame. The interceptor's accelerations in the LCIC frame are derived by solving the dynamic equations of motion (EoM's) at every discrete timestep of the simulation. The aerodynamic and propulsive forces are modeled in the Missile Body Coordinate frame (MBC frame) and are translated to the LCIC frame by applying the quaternion rotation matrix explained in subsubsection 2.3.4. Because a modified point mass model is used in this report, which uses implicit, rather than explicit angles of attack and sideslip, both the MBC frame and LCIC frame are inertial frames. The force equations can thus be solved directly in the MBC frame and the angular rates about the axes of the MBC frame do not need to be taken into account, as would be the case for 6-DOF simulations.

2.6.1. Velocity vectors in Missile Body Coordinate Frame

The interceptor's velocity vector in the MBC frame, $\mathbf{V}^b$, consists of three components; u, v, and w, defined along the directions of the missile body axes X_b, Y_b, and Z_b, respectively. The interceptor's velocity in the MBC frame is expressed by [28]:

$$\mathbf{V}^b = u\mathbf{i} + v\mathbf{j} + w\mathbf{k} = \begin{bmatrix} u \\ v \\ w \end{bmatrix}_b, \tag{20}$$

where $\mathbf{i}$, $\mathbf{j}$, and $\mathbf{k}$ are the unit vectors along the missile body axes X_b, Y_b, and Z_b [28].

2.6.2. Translational accelerations in Missile Body Coordinate Frame

Newton's second law stipulates that in an inertial reference frame, the time rate of change of an object's momentum is equal to the force acting on that object, in this case the interceptor. This can be mathematically expressed by:

$$\frac{d}{dt}(m\mathbf{V}) = \mathbf{F} = \begin{bmatrix} F_x \\ F_y \\ F_z \end{bmatrix}, \tag{21}$$

where m is the mass of the interceptor, $\mathbf{V}$ is its velocity vector and $\mathbf{F}$ is the force vector acting on the interceptor. Assuming the interceptor's mass remains constant or by taking m to be its instantaneous mass at timestep t when using numerical integration, Equation 21 can be rewritten to express the forces acting on the interceptor in the inertial MBC frame:

$$\mathbf{F}^b = m\dot{\mathbf{V}}^b = m(\dot{u}\mathbf{i} + \dot{v}\mathbf{j} + \dot{w}\mathbf{k}) = m \cdot \begin{bmatrix} \dot{u} \\ \dot{v} \\ \dot{w} \end{bmatrix}_b . \tag{22}$$

Rewriting Equation 22 to express the individual components of the interceptor's acceleration vector in the inertial MBC frame, $\dot{u}$,$\dot{v}$, and $\dot{w}$, results in:

$$\dot{u} = \frac{F_x}{m}, \tag{23}$$

$$\dot{v} = \frac{F_y}{m}, \tag{24}$$

and

$$\dot{w} = \frac{F_z}{m}, \tag{25}$$

where F_x, F_y, and F_z are the forces acting on the particle's centre of gravity in the local $x-$, $y-$, and $z-$ directions.

2.6.3. Accelerations in Launch-Centered Inertial Coordinate Frame

The translational acceleration equations in Equation 23 to Equation 25 are translated to the LCIC frame by applying the MBC-to-LCIC quaternion transformation matrix found in Equation 8, resulting in:

$$\dot{\mathbf{V}}^{LCIC} = \left([Q]^{LCIC}_{MBC}\right) \cdot \dot{\mathbf{V}}^b, \tag{26}$$

where $\dot{\boldsymbol{V}}^b$ is expressed as:

$$\dot{\boldsymbol{V}}^b = \begin{bmatrix} \dot{u} \\ \dot{v} \\ \dot{w} \end{bmatrix} . \tag{27}$$

2.7. Modelling Forces

The translational and rotational accelerations in the MBC frame, as expressed by Equation 23 to Equation 25, are functions of the forces- acting on the interceptor. The forces F_x^b, F_y^b, and F_z^b are the total forces acting on the interceptor's body in X_b, Y_b, and Z_b directions, respectively. The total forces are the sum of the individual propulsive and aerodynamic forces, as well as gravity. This is mathematically expressed as:

$$\mathbf{F}^b = \mathbf{F}_A^b + \mathbf{F}_p^b + \mathbf{F}_g^b, \tag{28}$$

where $\mathbf{F}_A^b$ are the aerodynamic forces acting along the missile's X_b, Y_b, and Z_b axes, $\mathbf{F}_p^b$ is the propulsive force vector in MBC coordinates, and $\mathbf{F}_g^b$ is the gravitational force vector in the MBC frame.

2.7.1. Aerodynamic forces

The aerodynamic forces acting along the MBC frame's axes are expressed as:

$$\mathbf{F}_A^b = F_{A_x}^b \mathbf{i} + F_{A_y}^b \mathbf{j} + F_{A_z}^b \mathbf{k} = \begin{bmatrix} F_{A_x} \\ F_{A_y} \\ -F_{A_z} \end{bmatrix}_b, \tag{29}$$

where:

$$\begin{bmatrix} F_{A_x} \\ F_{A_y} \\ F_{A_z} \end{bmatrix}_b = q_d \cdot S_{Ref} \cdot \begin{bmatrix} C_{N_x} \\ C_{N_y} \\ C_{N_z} \end{bmatrix}_b. \tag{30}$$

The aerodynamic force coefficients for all possible combinations of altitude, Mach number, and trim angle of attack are calculated using the semi-empirical aeroprediction code Missile DATCOM and are discussed in subsection 3.3.

2.7.2. Propulsive force

The propulsive force is assumed to always act perfectly along the missile's longitudinal axis (X_b-axis). Therefore, the propulsive force vector in the MBC frame can be expressed by:

$$\mathbf{F}_p^b = \begin{bmatrix} T \\ 0 \\ 0 \end{bmatrix}_b, \tag{31}$$

where T is the thrust force. Table 6 in subsubsection 3.1.2 presents the thrust over time of the SM-2 Block IIIA used in this report.

2.7.3. Gravitational force

The maximum altitude the interceptor will be flying at is 35 km. The gravitational acceleration g may thus be assumed to have a constant value of g = 9.81 m/s^2. The gravitational force acting on the missile in the LCIC frame may be expressed by:

$$\mathbf{F}_g^{LCIC} = \begin{bmatrix} 0 \\ 0 \\ mg \end{bmatrix}_{LCIC} \tag{32}$$

where m is the interceptor's (time-varying) mass. The gravity acting on the missile in the MBC frame is found by applying the LCIC-to-MBCF quaternion transformation matrix. Equation 33 now presents the gravity force acting on the missile in the MBC fame:

$$\mathbf{F}_g^b = \left([Q]_{LCIC}^{MBCF}\right) \cdot \mathbf{F}_g^{LCIC}, \tag{33}$$

where $[\mathrm{Q}]_{MBC}^{LCIC}$ is the quaternion transformation matrix as expressed by Equation 8.

2.8. Primary Command Point Calculation Procedure

The Primary Command Point is a point in space where the interceptor is expected to intercept a target. In this report, the Standard Missile-2 first uses Kappa guidance to fly towards the PCP before switching to semi-active homing using Proportional Navigation to manoeuvre onto a collision course.

To calculate the Primary Command Point, it must be known for any point in space around the launching ship how long it takes the interceptor to reach that point in space. To this end, flyout tables are constructed and displayed in subsection 4.1. The PCP is calculated iteratively. Selecting one of the flyout tables presented in subsection 4.1, the time-to-intercept can be found for any combination of downrange distance and altitude of an incoming target. Once the time-to-intercept to the target's current position is found, the expected future target position is extrapolated and a new time-to-intercept for the expected future target position is found. This procedure is continued until convergence, given the found Primary Command Point falls within the contours of the selected flyout table.

In the PCP calculation model used in this report, the target has a constant speed and acceleration in the North-East-Down frame. Using the Pythagorean theorem, the downrange and altitude positions of the target are calculated. For that given combination of downrange position and altitude, the time-to-intercept is found using one of the flyout tables presented in subsection 4.1. Then, given the resulting time-to-intercept and the target flying with a constant velocity and acceleration, a new target position in the NED frame can be calculated. For the updated position in the NED frame, the downrange position and altitude values are again calculated and plugged into the selected flyout table to find the new time-to-intercept value. This procedure is repeated until the time-to-intercept change decreases to a sufficiently small value.

Figure 14 presents the PCP calculation procedure schematically for one dimension.

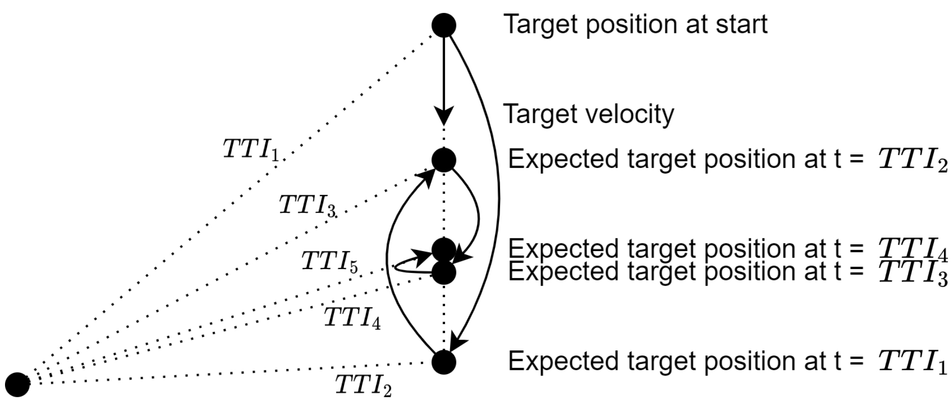

Figure 14: Schematic explanation of iterative procedure for calculating the Primary Command Point (PCP). PCP is found when consecutive values for time-to-intercept are sufficiently small.

2.9. Simulink model block diagrams

To simulate the interceptions of targets by the Standard Missile-2 Block IIIA, a MatLab Simulink code was developed. Similar to the guidance loop presented in subsection 2.2, a functional block diagram of the Simulink code consists of a loop that is iterated at each timestep. Figure 15 presents a functional block diagram of the Simulink model used in this report.

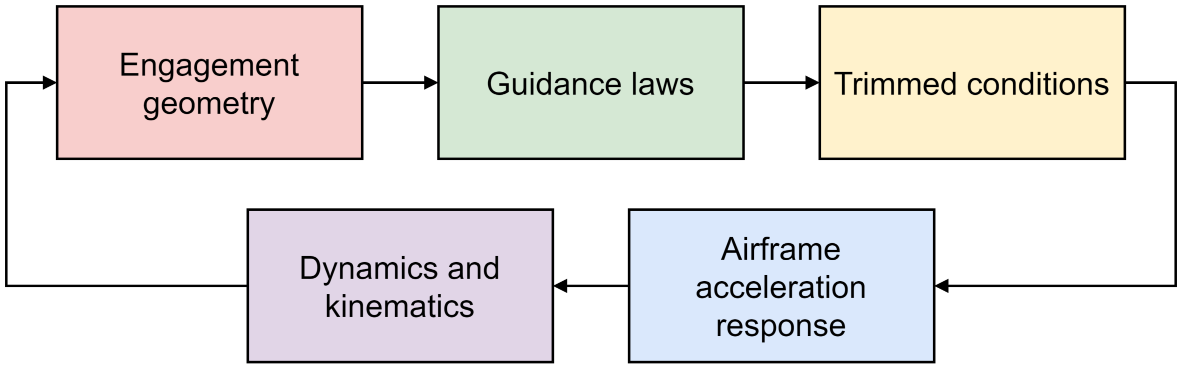

Figure 15: Simulink simulation loop used in this report

To start, the engagement geometry is established in the Launch-Centered Inertial Coordinate frame. The position, velocity, and acceleration vectors of the Standard Missile-2 and the target are given, as well as the position of the Primary Command Point. The relative geometries between the interceptor and PCP and between the interceptor and target are calculated and the resulting variables are used as inputs to the guidance section. Figure 16 presents the internal block diagram of the engagement geometry:

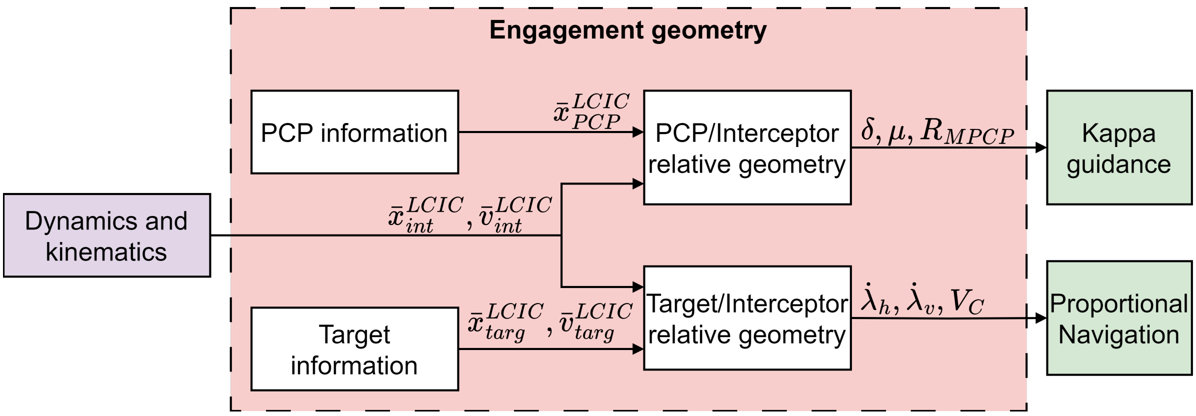

Figure 16: Engagement geometry block diagram

The guidance law section, whose functional block diagram is presented in Figure 17, calculates the interceptor's acceleration commands using information derived from the engagement geometry. During the midcourse phase, Kappa guidance is used. Once the interceptor is close enough to the target, the guidance section switches to Proportional

Navigation. Both Kappa guidance and Proportional Navigation output the interceptor's acceleration command with respect to the interceptor's velocity vector.

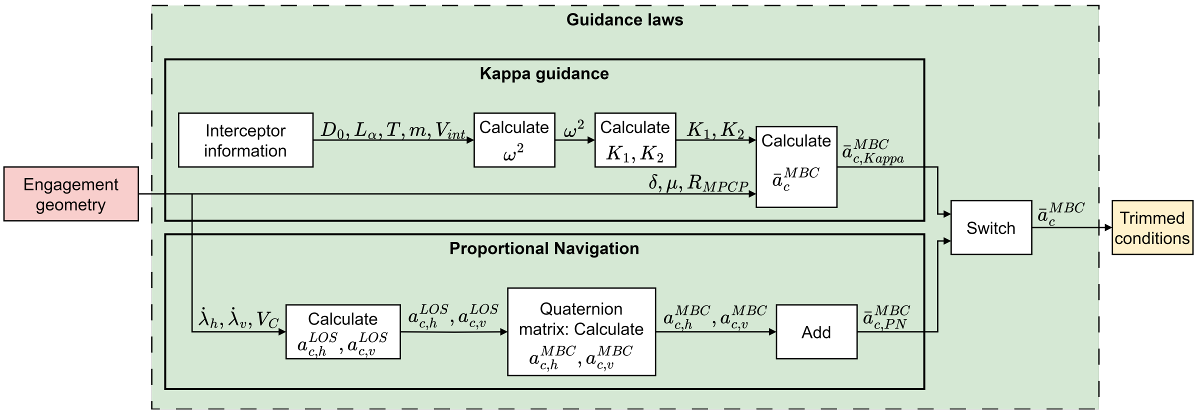

Figure 17: Guidance law block diagram

The resulting acceleration commands are input to the aerodynamic trim conditions section. The aerodynamic trim conditions section uses the aerodynamic database described in subsection 3.3, in which the airframe's trimmed lift- and drag coefficients are given for any combination of center of gravity position, Mach number, and trimmed angle of attack. Using the interceptor's mass and dynamic pressure, the commanded acceleration is translated into a required lift coefficient, which, using the aerodynamic database, translates to a required angle of attack, α_{trim}, and tail fin deflection angle, δ_{trim}. The interceptor can not fly at angles of attack larger than the maximum trimmed angle of attack. In case the commanded acceleration exceeds the maximum achievable acceleration command at $\alpha_{trim,max}$, the commanded acceleration is limited to what can be achieved at $\alpha_{trim,max}$. Consequently, the commanded $\alpha_{trim,max}$ is translated back to the trimmed acceleration command, which is used as an input for the airframe acceleration response section.

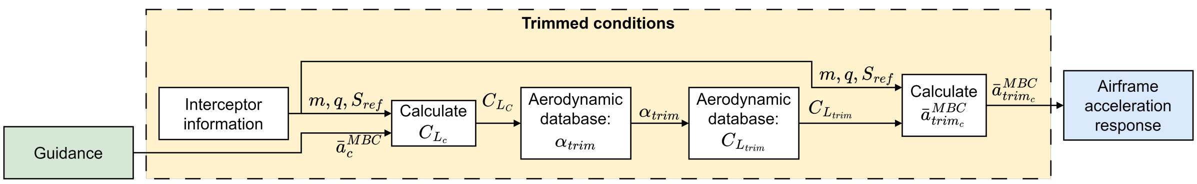

Figure 18: Trimmed conditions block diagram

The flight altitude, Mach number, and trimmed acceleration command are used as inputs to model the airframe's acceleration response. The altitude, Mach number, and trimmed acceleration command are used as inputs to the database returning the first-order acceleration response time delay constant τ, described in subsection 3.4. The airframe's acceleration response is modelled through the implementation of a first-order transfer function, in which the τ is updated at every timestep. The resulting acceleration response has an associated drag value through the consultation of the aerodynamic database. The drag force is translated to an acceleration and both the achieved trimmed acceleration response and deceleration due to drag are passed on to the dynamics and kinematics section.

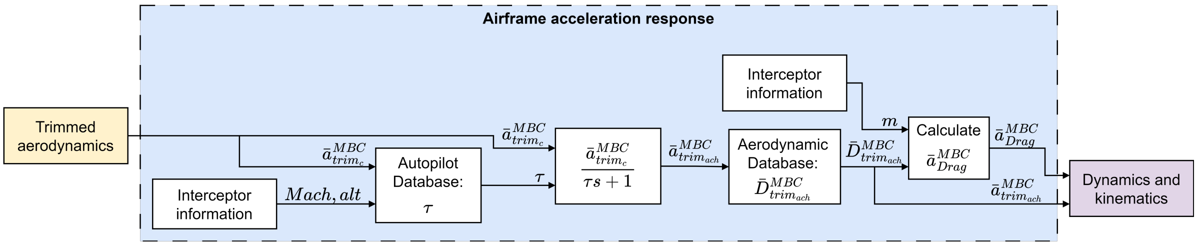

Figure 19: Airframe response block diagram

In the dynamics and kinematics section, the achieved trimmed acceleration response and acceleration vector resulting from drag are first translated from their values with respect to the velocity vector into the LCIC frame. The quaternion transformation matrix between the MBC frame (which is aligned with the velocity frame) and the LCIC frame is used to this extent, resulting in a 'total aerodynamic acceleration vector'. The airframe's aerodynamic acceleration vector is added to the thrust- and gravity acceleration vectors, resulting in the total interceptor acceleration in the LCIC frame at the given timestep. Finally, the total interceptor acceleration is integrated forward in time, resulting in the velocity and position vectors in the LCIC frame, completing the Simulink loop. The Simulink loop is iterated until a successful intercept occurs or termination conditions are met.

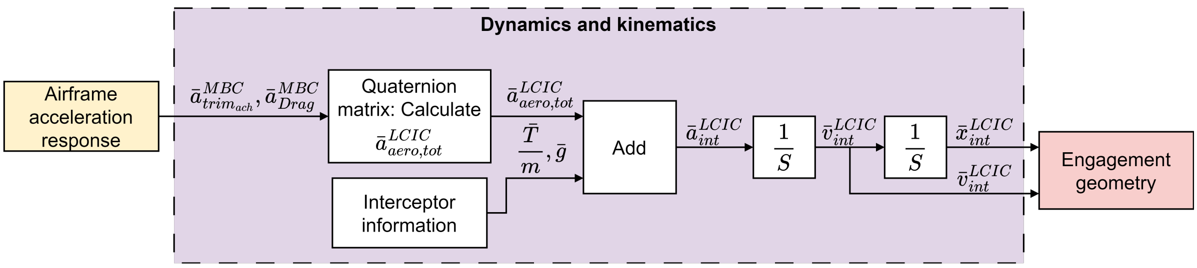

Figure 20: Kinematics block diagram

2.10. Verification of Simulink model

The Simulink model is verified to ensure no modelling errors have been made. The implementation of the kinematic equations, static aerodynamics coefficients, proportional navigation, and transformation matrices were verified by comparing the base Simulink model to the thesis supervisor's own interceptor model. The final Simulink model implements many new functionalities that are central to this thesis, including, but not limited to, Kappa midcourse guidance, the airframe's delayed acceleration response, time-varying airframe mass and time-varying aerodynamic coefficients. Therefore, not all final functionalities were verified.

2.10.1. Simulink model verification

Using airframe- and aerodynamic data for the AIM-7 Sparrow provided by the thesis supervisor, simulations were run in both Simulink models. To initiate the simulation, Table 2 and Table 3 present the initial conditions of the target and AIM-7 Sparrow, respectively:

Initial position	10000 m Southward 10000 m Westward 50 m Altitude
Initial Velocity	200 m/s
Initial Heading	30 deg (North-West)
Initial Ground angle	25 deg (upwards)

Table 2: Verification setup: Initial target state

Initial altitude	3000 m
Initial Velocity	275 m/s
Initial Direction	Towards target initial position
Guidance mode	Proportional Navigation
Guidance turns on after	1 second
Proportional Navigation gain N'	3
Gravity compensation	Yes: N'/2

Table 3: Verification setup: AIM-7 Sparrow initial state

The simulation results, including intercept location, time-to-intercept, interceptor velocity, and interceptor attitude at intercept are presented in Table 4. The positional error at intercept does not exceed 0.06%, the time-to-intercept error is 0.11%, the interceptor velocity at intercept is 0.07%, and the attitude at intercept error is 5.0%. The interceptions are visualized in Figure 21. The models use different models to visualize the results, but Figure 21 presents the reader with a qualitative visualization of the great similarities between both interception geometries. Though independently developed, the results of the Simulink models were nearly identical. This verifies the correct working of the base Simulink model, after which the additional functionalities were added.

Parameter	Author's results	Supervisor's results	Error (%)
Intercept location	-4952.4 N -9558.4 E -1407.7 D	-4949.3 X -9558.4 Y -1408.4 Z	0.06 0 0.05
Time to intercept	17.485	17.497	0.11
Interceptor velocity at intercept	557.855 m/s	557.336 m/s	0.07
Interceptor attitude at intercept	-13.429 deg	-14.138 deg	5.01

Table 4: Verification of base Simulink model: Comparison of interception results between thesis supervisor and author

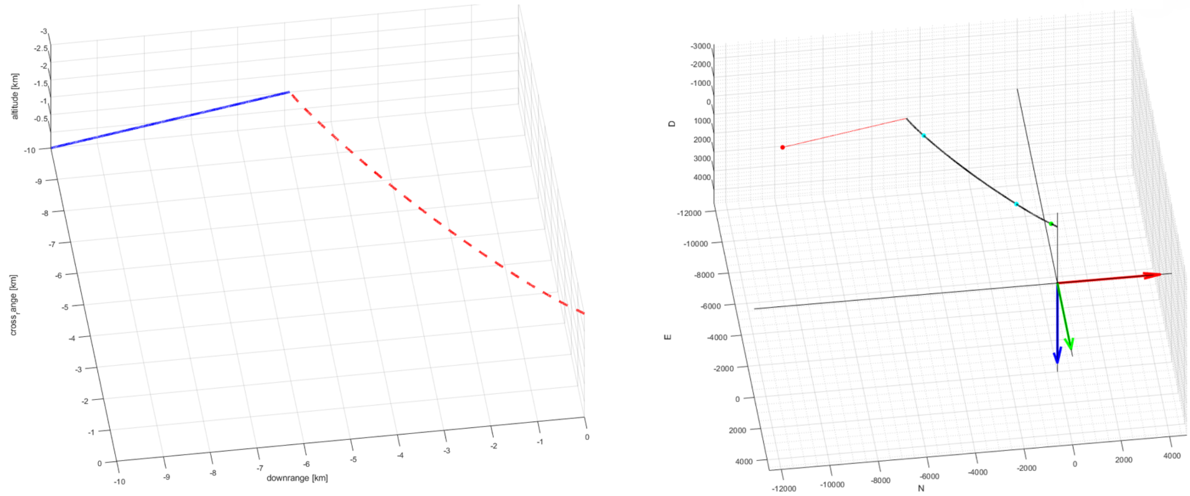

(a) Dr. Savelsberg's intercept geometry

(b) Author's intercept geometry

Figure 21: Visualization of verification of base Simulink model: AIM-7 Sparrow intercepting a flying target

2.10.2. Standard Missile-2 performance verification

The full Simulink model and SM-2 interceptor information were verified by constructing flyout tables and comparing the found maximum range, burnout Mach number, and service ceiling to the information found in the public literature. Repeating the information found in the introduction section, the Standard Missile-2 Block IIIA has a maximum range of 167 km, a burnout Mach number of 3.0 to 3.5, and a service ceiling of 20km [1] [35]. The flyout table for Kappa guidance with no specified intercept angle, found in Figure 37, confirms the found sea-level adjusted burnout Mach number of 3.8 and service ceiling of 20 km to 25 km are comparable to the values found in the public literature. However, the maximum ground range of 83 km is short of the publicly reported range of 167 km.

The Kappa midcourse guidance algorithm was modified to obtain a longer range, by forcing the interceptor to first fly through the atmosphere at higher altitudes. The modified Kappa guidance algorithm commands a constant pitch-over acceleration of 3 g for the first 25 seconds of flight, after which 'normal' Kappa guidance is activated. The resulting maximum range against sea-skimming targets increased to 173 km, very closely aligning with the publicly disclosed maximum range of 167 km.

3. Interceptor Modelling and threat descriptions

To properly analyse the SM-2's kinematic performance and simulate engagements of incoming threats, the interceptor and threats must be modelled in sufficient detail. The SM-2's MK104 Dual-Thrust Rocket Motor, internal and external body geometry, wing and tail fin geometry, actuators, time-varying mass, time-varying centre of gravity, and time-varying pitching moment of inertia are described in this section. Subsequently, an aerodynamic database of the SM-2 is constructed using Missile DATCOM98 and the SM-2's autopilot and acceleration response to a commanded acceleration are described. Finally, the threats described in the introduction of this report are described and quantified in order to properly simulate interception scenarios.

3.1. Interceptor Properties

Public information on the Standard Missile-2's general and geometric properties is sufficient to allow for reasonably detailed and accurate modeling. The SM-2 Block IIIA has a length of 4.72m, a diameter of 0.343m, a mass of 706.7kg, and uses the MK104 MOD1 Dual-Thrust Rocket Motor (DTRM) for propulsion [1], [37], [35], [38] .

3.1.1. MK104 DTRM and propellant properties

Janes Naval Weapon Systems Issue 54 from 2011 [35] reports that the SM-2 Block II has a propellant mass of 381.4kg. In a more recent posting in Janes Naval Weapons from 2017-2018, it is reported that the SM-2 Block IIIA has a propellant mass of 358kg [1].

Table 5 presents the properties of the MK104 rocket engine that propels the SM-2 (ER) presented by Shen et al. [39]. For completeness, the information by Shen et al. on the SM-2 (ER)'s additional MK72 booster has also been provided in Table 5, although it should be repeated that this report focuses on the SM-2 Block IIIA (Medium Range) without the MK72 booster. The information on the MK104 by Shen et al. seems to be referring to a variant of the MK104, as the original MK104 engine is a Dual Thrust Rocket Motor, consisting of a boost phase and a sustain phase. Shen et al.'s reported constant thrust output of 22kN for a duration of 40 seconds seems too little thrust for too much time. However, considering that the first stage of the SM-2 ER is the MK72 Booster, it may be reasonable to assume that the original MK104 has been replaced by a variant that only operates in sustain mode, with the propellant mass being equal to the original MK104 DTRM. Nevertheless, Shen's reported propellant mass of 358.5kg confirms Janes' SM-2 Block IIIA's propellant mass of 358kg.

3.1.2. Mass and thrust values used in this report

Both Janes [1] and Shen et al. [39] report a propellant mass of 358kg. Based on the advice of the supervisor of this report, Dr.ir. Ralph Savelsberg, and considering the MK104 is indeed

MK72 booster parameter	Value	Unit	MK104 engine parameter	Value	Unit
Booster mass	787.7	kg	Engine mass	567.3	kg
Propellant mass	474.6	kg	Propellant mass	358.5	kg
Working time	6	s	Working time	40	s
Thrust	174	kN	Thrust	22	kN
Specific impulse	224.3	s	Specific impulse	254.9	s

Table 5: MK72 booster and MK104 engine properties of the SM-2 (ER) according to Shen et al. [39]

a Dual-Thrust Rocket Motor, the MK104 DTRM engine properties operating in the boost- and sustain phases used in this report are presented in Table 6.

Booster Properties	Value	Unit	Sustainer properties	Value	Unit
Propellant mass	160	kg	Propellant mass	200	kg
Thrust	138.65	kN	Thrust	40	kN
Working time	3	s	Working time	13	s
Specific impulse	265	s	Specific impulse	265	s

Table 6: SM-2 Block IIIA mass and thrust values used in this report

3.1.3. Geometry of SM-2 Block IIIA

Brown and Herman [38] present a detailed report presenting the geometry of the SM-2 Block I and mass properties of all components. The geometry of the Standard Missile-2 is used to estimate the center of mass and moment of inertia properties of the interceptor. Appendix A.5 presents Brown and Herman's diagrams outlining the missile geometry [38]. The missile described in the report is believed to be an SM-2 Block I because the gap between the wings and tail fins is shorter than that of modern variants. The missile described in the report has a total length of 4.03 m and a diameter of 0.343 m [38]. The missile has a propellant section length of 83.3 cm and holds 124.73 kg of propellant with a density of 1.74383 g/cm^3 [38].

The SM-2 Block II and block III variants are lengthened from 4.03 to 4.72 meters. This is externally visible from the increased gap length between the main wings and tail fins. Assuming the 358kg of propellant as reported by Janes [1] is accurate, the propellant density has remained the same, and the inner diameter of the propellant section as reported by Brown and Herman is 0.3306 m, the internal propellant section is lengthened to 239.1 cm.

The rocket motors of the Block II and Block III variants are upgraded from the MK56 to the MK104 DTRM [1]. It is assumed that for the MK104 rocket motor, the propellant section ends at the leading edge of the root of the tail fins to leave sufficient space for the rocket engine nozzle to expand the outflowing combustion gases to supersonic speeds and for space around the throat to be used for the tail fin actuators. The SM-2 Block IV as presented by Montoya [40] shows that the propellant section of the Block IV's MK104 MOD2 engine also ends at the start of the tail fins, with the nozzle taking up the remaining length of the tail section. The nozzle diameter of the MK56 as found by Brown and Herman is 9.64cm [38].

Although the MK104 DTRM may have a different nozzle diameter, it is assumed that the nozzle diameter of the MK104 has remained at 9.64cm.

3.1.4. Geometric model used in this report

The geometric model presented by Brown and Herman (appendix A.5) is used as a starting point to develop a digital model that can be used to calculate aerodynamic coefficients in Missile DATCOM. Figure 22 presents a reproduction of the SM-2 described in the report by Brown and Herman, including the modification that lengthens the gap between the main wing and tail fins. The internal propellant section has been been lengthened from 83.3cm to 235cm and ends at the leading edge of the root of the tail fins. A propellant section length of 235cm is chosen instead of 239.1cm to keep the starting position of the propellant section consistent with Brown and Herman's report, as well as its end being at the start of the tail fin, under which the nozzle is located. The geometric specifications of the Standard Missile-2 Block IIIA are presented in Figure 22.

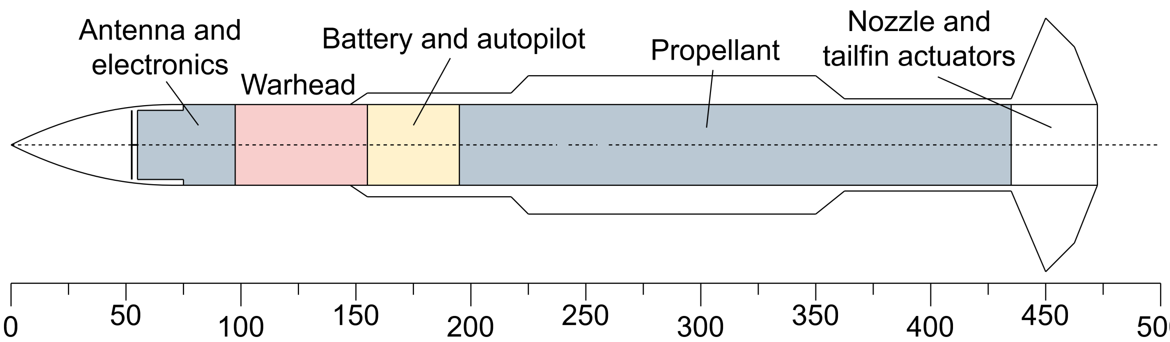

Figure 22: Digital reproduction of Brown and Herman's geometric model of the SM-2 [38]. Includes modification that lengthens the gap between the main wing and tail fins to the dimensions of the SM-2 Block II and Block III series, as well as a lengthened propellant section.

3.1.5. Internal component arrangement

Table 7 presents the axial locations of the start of each subcomponent of the interceptor as described by Brown and Herman [38]. Note that the starting location of each subcomponent is also the end location of the previous component.

Component name	Axial location start of component (m)	Length of component (m)
Antenna and electronics	0.55	0.42
Warhead	0.97	0.58
Battery and autopilot	1.55	0.46
Propellant	2.01	2.35
Nozzle and tailfin actuators	4.36	0.36

Table 7: Axial location of start and length of interceptor components. These values are used to calculate the interceptor's center of gravity and moments of inertia [38].

3.1.6. Main wing and tail fin geometry

The planform and cross-sectional geometry of the main wings and tail fins are discussed in this section. Using Figure 22 based on Brown and Herman's report (appendix A.5 [38]) and open-source photos of the main wing's cross section (appendix A.6), the main wing and tail fin planforms and cross-sections are described in Figure 23, Table 8, Figure 24, and Table 9. The variables and values found in Table 8 and Table 9 correspond to the inputs of the Missile DATCOM98 input file. Due to inherent geometric limitations of Missile DATCOM98, the main wing strake is given a small sweep angle in the input file. Ideally, the radial location of the third Leading Edge location, $SSPAN3$ in Figure 23, should coincide with the radial location of the second Leading Edge, $SSPAN2$.

Both the main wing and tail fin planform measurements were taken from Brown and Herman [38]. The main wing's cross sectional values at the four stations were estimated using Figure 55 and Figure 56 in subsection A.6. The tail fin cross-sectional geometry could not be estimated accurately. An iterative method was applied to find a hexagonal cross-sectional geometry that improved the lift-to-drag ratio compared to the standard Missile DATCOM98 cross-sectional geometry. Figure 24 and Table 9 presents the planform and cross-sectional geometry chosen for the Missile DATCOM98 inputs.

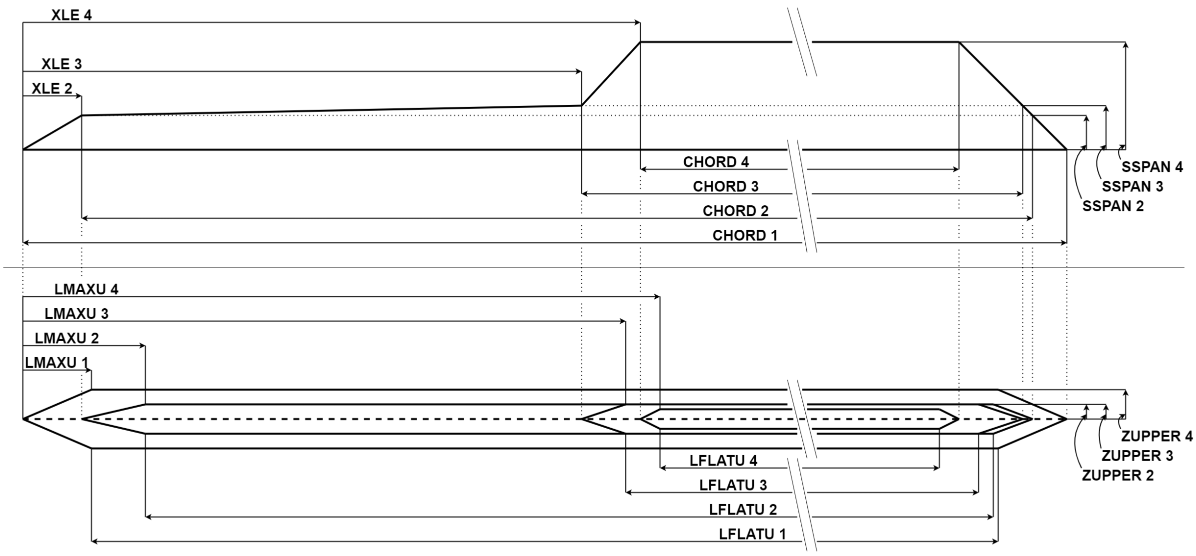

Figure 23: Main wing planform and cross-sectional geometry used in this report

DATCOM input variable	**Value**	**Unit**
XLE1, XLE2, XLE3, XLE4	1.4793, 1.5521, 2.1881, 2.2677	(m)
SSPAN1, SSPAN2, SSPAN3, SSPAN4	0.0, 0.045, 0.055, 0.136	(% chord)
CHORD1, CHORD2, CHORD3, CHORD4	2.1515, 2.0387, 1.3876, 1.2270	(m)
LMAXU1, LMAXU2, LMAXU3, LMAXU4	0.04, 0.04, 0.04, 0.04	(% chord)
ZUPPER1, ZUPPER2, ZUPPER3, ZUPPER4	0.019, 0.009, 0.0125, 0.007	(% chord)
LFLATU1, LFLATU2, LFLATU3, LFLATU4	0.92, 0.92, 0.92, 0.92	(% chord)

Table 8: Planform and cross-section descriptions of main wings used in this report

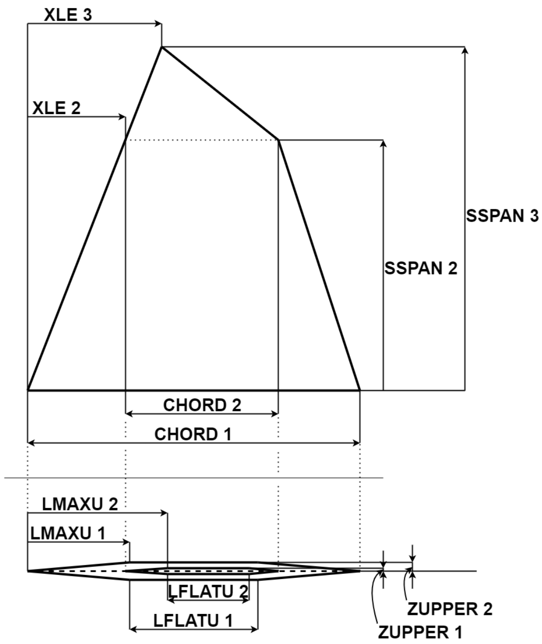

Figure 24: Tail fin planform and cross-sectional geometry used in this report

DATCOM input variable	Value	Unit
XLE1, XLE2, XLE3	4.3560, 4.4596, 4.4996	(m)
SSPAN1, SSPAN2, SSPAN3	0.0, 0.266, 0.3684	(% chord)
CHORD1, CHORD2, CHORD3	0.3640, 0.1667, 0.0	(m)
LMAXU1, LMAXU2, LMAXU3	0.3, 0.3, 0.3	(% chord)
ZUPPER1, ZUPPER2, ZUPPER3	0.025, 0.020, 0.020	(% chord)
LFLATU1, LFLATU2, LFLATU3	0.4, 0.4, 0.4	(% chord)

Table 9: Planform and cross-section descriptions of tail fins used in this report

3.1.7. Actuator properties

Tail-controlled interceptors respond to acceleration commands by deflecting the tail fins, resulting in the interceptor obtaining the required (trimmed) angle of attack after some delay. To accurately model the interceptor's acceleration response to a commanded acceleration signal, the tail fins must be modeled in sufficient detail.

Goldshine and Lacy [41] present a detailed paper outlining the high-response electromechanical control actuator in use by the Standard Missile family in 1968. It is expected that since 1968, improvements have been made to the electromechanical control actuators. However, as only the 'external' behaviour of the control actuator, e.g. the tail rate and damping is modeled, not the internal behaviour and control loops, the findings of Goldshine and Lacy's report are still used to approximate the actuator behaviour in subsection 3.4. Figure 25 presents an overview of the actuators used in the Standard Missile family of interceptors as presented by Goldshine and Lacy [41]. Table 10 presents the control actuator properties that are used to model the actuator response from commanded control surface deflection to actual control surface deflection as a second-order transfer function in the SIMULINK model [41].

Parameter	Requirement
Maximum deflection angle	± 50 deg
Transport delay time (from applied control signal to actuator reversal at full rate)	3 ± 1 ms
No-load tail rate	200 ± 50 deg/s
Load sensitivity (tail drift rate/in.-lb of applied external hinge moment)	0.05 deg/s/in.-lb

Table 10: Standard Missile-2 electromechanical control actuator properties [41]

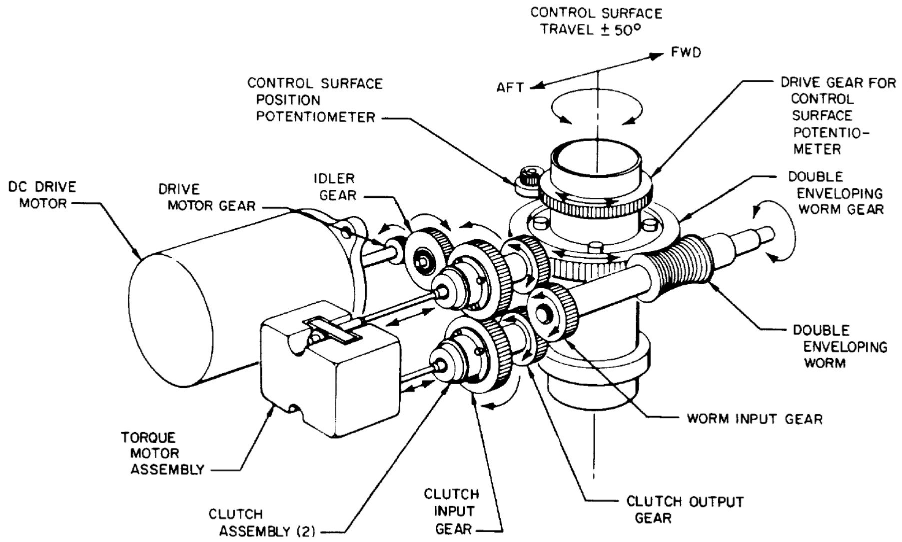

Figure 25: Electromechanical control actuator used in the Standard Missile family. Source: Goldshine and Lacy [41]

3.2. Interceptor Mass, Center of Gravity, and Moments of Inertia

During the initial boost and sustain phase, the propellant, which accounts for more than half of the interceptor's starting mass, is burned up. The center of gravity shifts forward and the moments of inertia change significantly. These non-trivial effects must be taken into account explicitly when modeling the kinematics of the Standard Missile-2 Block IIIA.

3.2.1. Modelling interceptor mass over time

The Standard Missile-2's mass is modeled as a function of time while the MK104 boost-sustain engine fires. Strickland models an interceptor's instantaneous mass as a function of the specific impulse and produced thrust according to [42]:

$$m(t) = m_0 - \frac{1}{I_{sp} g_0} \int_0^{t_{burnout}} F_p dt, \tag{34}$$

where m_0 is the interceptor's mass as t = 0, I_{sp} is the specific impulse, g_0 is the gravitational acceleration at sea level, and F_p is the produced thrust. I_{sp} is defined as:

$$I_{sp} \equiv \frac{F}{\dot{m} g_0}. \tag{35}$$

Modifying Equation 34 slightly to model the interceptor mass as a function of the empty mass and propellant mass results in:

$$m(t) = m_{empty} + m_p(t), \tag{36}$$

where m_p is the propellant mass, modeled as:

$$m_p(t) = m_{p_0} - \frac{1}{I_{sp} g_0} \int_0^{t_{burnout}} F_p dt, \tag{37}$$

where F_p varies between the boost and sustain phases following Table 6. The simulated propellant mass as a function of time thus becomes:

$$
\begin{cases}
m_p(t) &= m_{p_0} - \frac{1}{I_{sp} g_0} \int_0^{t_{end,boost}} F_{p,boost} dt, & \text{Boost phase} \\
m_p(t) &= m_{p_{start,sustain}} - \frac{1}{I_{sp} g_0} \int_{t_{end,boost}}^{t_{end,sustain}} F_{p,sustain} dt, & \text{Sustain phase} \\
m_p(t) &= 0, & \text{Unpowered flight}
\end{cases}
\tag{38}
$$

Using the SM-2 Block IIIA's mass- and thrust values as described in Table 6, Figure 26 presents the resulting interceptor mass as a function of time. Table 11 lists the values in table format.

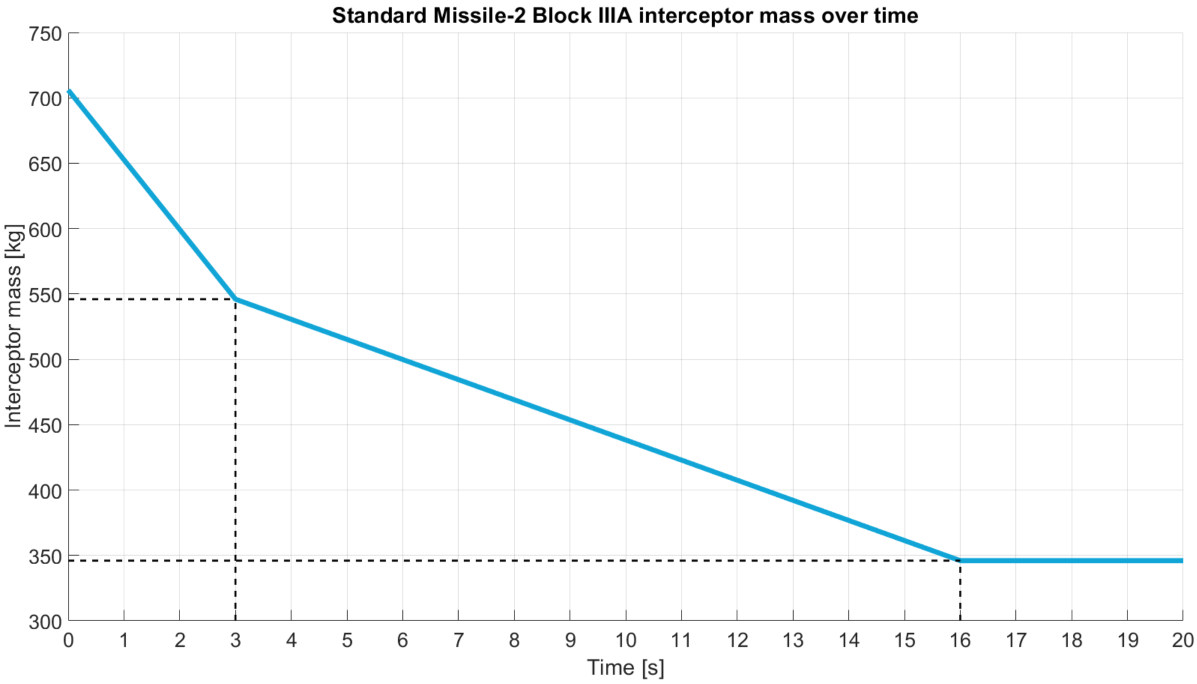

Figure 26: Standard Missile-2 Block IIIA mass over time. Time is shown until t = 20s. At t = 0s, the interceptor has a mass of 706kg. At t = 3s, the interceptor's mass is 546kg. At t = 16s, the MK104 DTRM burns out and the interceptor's mass remains constant at 346kg.

Timestep	Interceptor mass (kg)	Propellant mass (kg)
t = 0 s (start boost)	706	360
t = 3 s (end boost phase)	546	200
t = 16 s (end sustain phase)	346	0

Table 11: Interceptor and propellant mass at start of boost phase, end of boost phase, and end of sustain phase

3.2.2. Modelling interceptor center of gravity over time

The center of gravity shifts over time as the propellant is burned through. The propellant is modeled to burn radially from the centerline outwards. Thus, the axial center of gravity of the propellant section does not shift over time. The center of gravity of the propellant does not coincide with the center of gravity of the empty interceptor. Thus, the time-varying center of gravity of the whole interceptor is a function of the centers of gravity of each component, as expressed by:

$$X_{CG}(t) = \frac{\sum m_i(t) \cdot X_{CG_i}}{\sum X_{CG_i}} \tag{39}$$

where $X_{CG}(t)$ is the interceptor's center of gravity, m_i(t) is the (time-varying) mass of each component and X_{CG_i} is the center of gravity position of each component, where Table 12 expresses the values of m and X_{CG} for each interceptor component:

Component name	**Mass (kg)**	**X_{CG}**
Front section	277.56	1.28
Rear section	68.44	4.54
Propellant section at t = 0 s	360	3.185
Propellant section at t = 3 s	200	3.185
Propellant section at t = 16	0	3.185

Table 12: Mass and center of gravity position for each of the Standard Missile-2 Block IIIA's components. Front section is from the antenna to the autopilot. Rear section consists of the nozzle and tailfin actuators.

Applying the values found in Table 12 to Equation 39, the Standard Missile-2 Block IIIA's center of gravity is calculated at each timestep. Figure 27 presents the resulting center of gravity of the SM-2 Blk. IIIA as a function of time:

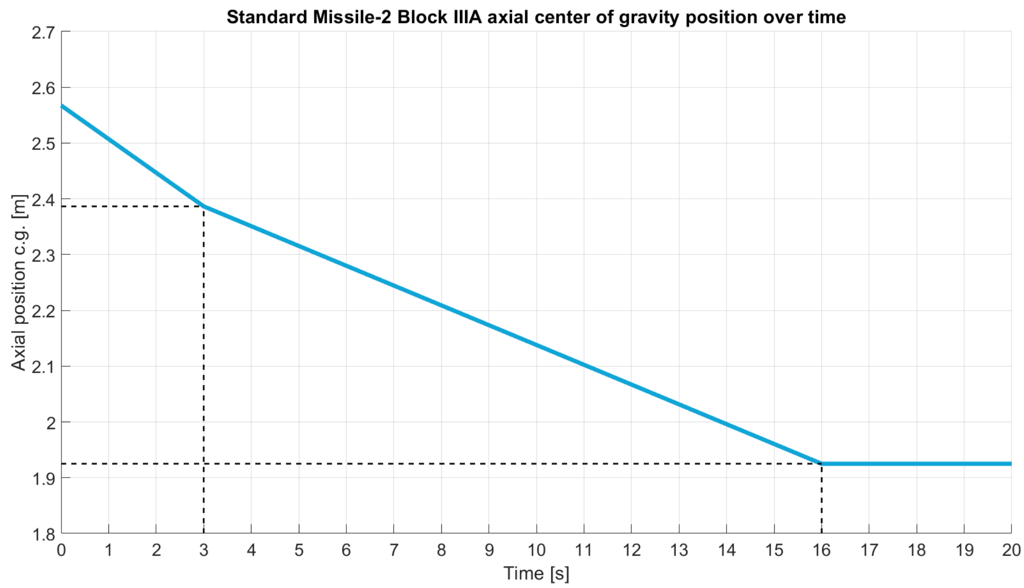

Figure 27: Center of gravity position of the Standard Missile-2 Block IIIA over time

Figure 28 visually presents the results in relation to the missile geometry and Table 13 presents the results in table format.

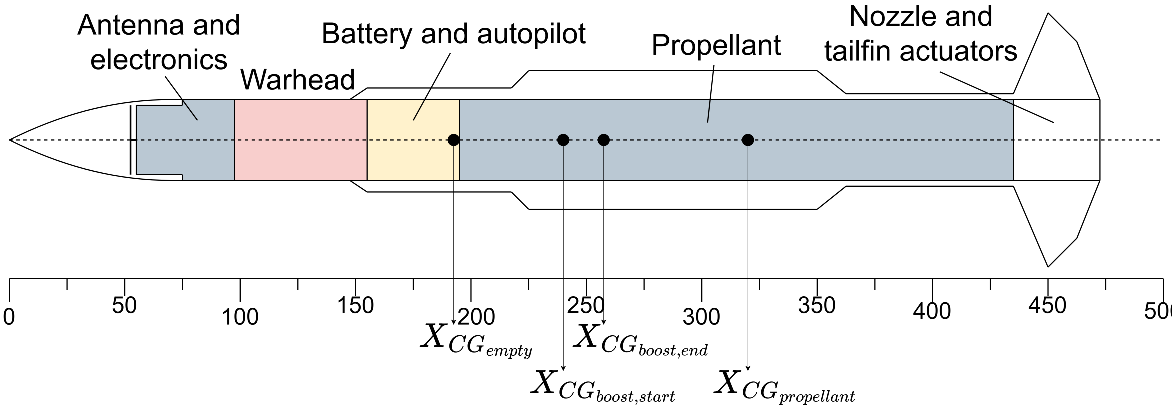

Figure 28: Center of gravity position of propellant, at start and end of boost phase, and of empty interceptor

Property	**Value (m)**
$X_{CG_{propellant}}$	3.185
$X_{CG_{boost,start}}$ (t = 0 s)	2.568
$X_{CG_{boost,end}}$ (t = 3 s)	2.387
$X_{CG_{empty}}$ (t = 16 s)	1.925

Table 13: Center of gravity position of propellant, at start and end of boost phase, and of empty interceptor

3.2.3. Modelling pitch and yaw moments of inertia over time

The moments of inertia about the interceptor's shifting center of gravity in the pitch- and yaw planes are found by adding the contributions of each of the interceptor's components, mathematically expressed as:

$$I_{y_{CG,tot}}(t) = I_{z_{CG,tot}}(t) = \sum I_{y,i} + m_i \cdot \left(X_{CG}(t) - X_{CG,i}(t)\right)^2 \tag{40}$$

where $I_{y_{CG,tot}}(t)$ and $I_{z_{CG,tot}}(t)$ are the interceptor's time-varying total moments of inertia about the Y-, and Z-axes originating from the (time-varying) center of gravity of the interceptor. Because the interceptor is symmetric, $I_{y_{CG,tot}}$ and $I_{z_{CG,tot}}$, are the equal. $I_{y,i}$ is each component's pitching moment of inertia about its own center of gravity, m_i is each component's mass, $X_{CG}(t)$ is the interceptor's time-varying center of gravity, and $X_{CG,i}$ is each component's (time-varying) center of gravity.

Assuming each of the interceptor's components are modeled as a solid cylinder whose diameter is equal to the interceptor's diameter, the pitching moment of inertia of each of the interceptor's components is calculated using the standard mechanics of materials equation for solid cylinders:

$$I_{y,i} = \frac{1}{16} m_i D^2 + \frac{1}{12} m_i L_i^2, \tag{41}$$

where m_i is the component's mass found in Table 12, D is the interceptor's outer diameter, and L_i is the component's length found in Table 7.

Given the propellant burns radially, the propellant section is modeled as an annular cylinder whose pitching moment is calculated using:

$$I_{y,propellant} = \frac{m_p(t)\left(D_{inner,p}^2(t) + D_{outer}^2(t)\right)}{16} + \frac{m_p(t) L_p^2}{12}, \tag{42}$$

in which $m_p(t)$ is the propellant's time-varying mass, D_{outer} is the interceptor's outer diameter, L_p is the propellant section length, and D_{inner} is the propellant's inner diameter, calculated using:

$$D_{inner,p}(t) = \sqrt{D_{outer}^2 - \frac{m_p(t)}{\rho_p} \frac{4}{\pi} \frac{1}{L_p}}, \tag{43}$$

where ρ_p is the propellant density.

Table 14 presents each component's pitching moment of inertia about its own center of gravity, the component's parallel axis theorem moment of inertia contribution to the interceptor's time-varying center of gravity, and the resulting total pitching moment of inertia about the interceptor's time-varying center of gravity:

Component	**$I_{y,i}$ (kgm^2)**	**$m_i \cdot (X_{CG}(t) - X_{CG,i}(t))$ (kgm^2)**	**I_{yCG} at t = 0 s (kgm^2)**	**I_{yCG} at t = 3 s (kgm^2)**	**I_{yCG} at t = 16 s (kgm^2)**
Front section	51.35	460.10	511.45	391.24	166.82
Rear section	2.56	266.28	268.84	319.92	470.56
Propellant at t = 0 s	72.96	137.27	210.23	-	-
Propellant at t = 3 s	41.14	127.49	-	168.63	-
Propellant at t = 16 s	0	0	-	-	0

Table 14: Pitching moment of inertia of each component, parallel axis theorem moment of inertia contributions, and total pitching moment of inertia about interceptor's time-varying center of gravity for each component

The resulting total time-varying moments of inertia about the interceptor's pitch- and yaw-axes of the time-varying center of gravity is presented in Figure 29. Table 15 presents the results in table format.

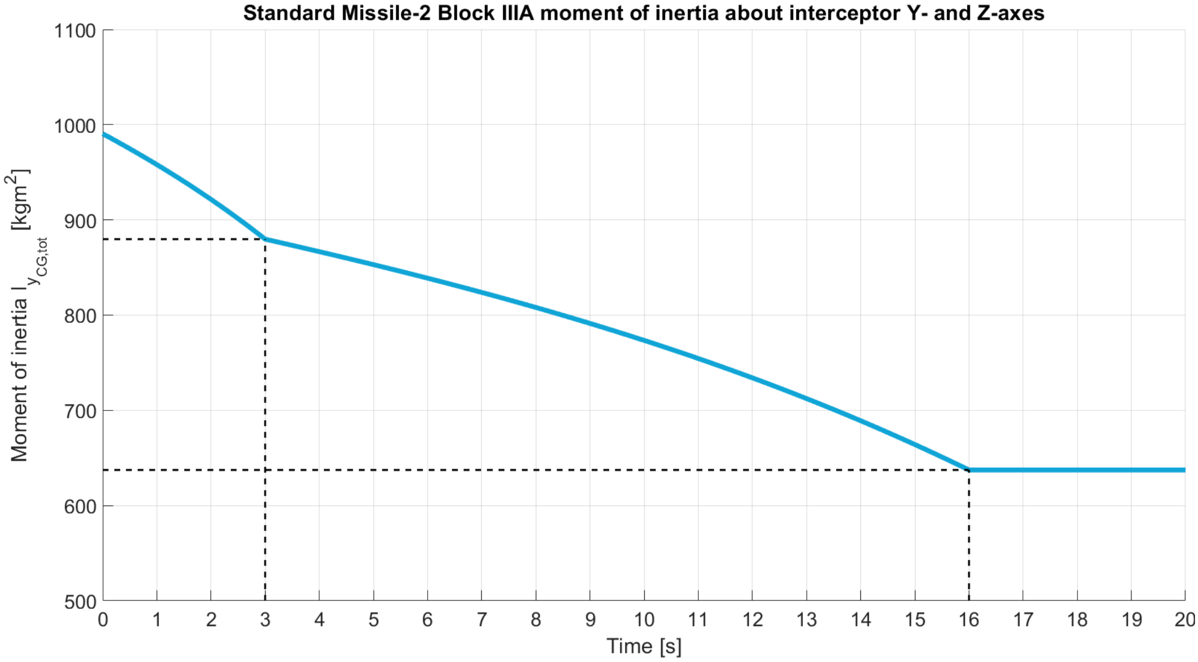

Figure 29: Moment of inertia about the SM-2 Block IIIA's Y- and Z-axes, $I_{y_{CG,tot}}$ and $I_{z_{CG,tot}}$

Timestep	$\boldsymbol{I_{Y_{CG,tot}}}$ **(kgm^2)**	$\boldsymbol{I_{Z_{CG,tot}}}$ **(kgm^2)**
Start boost phase (t = 0 s)	990.51	990.51
End boost phase (t = 3 s)	879.79	879.79
End sustain phase (t = 16 s)	637.38	637.38

Table 15: Moments of inertia about the SM-2 Block IIIA's center of gravity at the start of the boost phase, end of the boost phase, and end of the sustain phase

3.3. Aerodynamic Analysis

In this subsection, the Standard Missile-2's aerodynamics are analysed. To properly simulate the SM-2's flyout behaviour, an aerodynamic database is developed that presents for any combination of centre of gravity location, Mach number, and trimmed angle of attack the trimmed tailfin deflection angle δ, lift coefficient C_L, and drag coefficient C_D. Missile DATCOM98, a semi-empirical aeroprediction software developed for the United States Air Force, is used to construct this aerodynamic database.

3.3.1. Trimmed conditions Free Body Diagram

Figure 30 presents a Free Body Diagram of the Standard Missile-2 flying at trimmed conditions. In this report, the definition of 'trimmed conditions' is that the interceptor achieves a constant acceleration perpendicular to the current velocity vector, with the sum of all (aerodynamic) moments acting on the airframe adding up to zero. in Figure 30, the interceptor flies at a certain vertical flight path angle γ, angle of attack α, and body pitch angle θ. The lift- and drag forces are modeled to originate from the centres of pressure of the main body and the tail fins. The centre of pressure of the main body shifts axially for varying Mach numbers and angles of attack. For each combination of centre of gravity location, Mach number, and angle of attack, the tailfin deflection angle required to achieve a net-zero moment about the interceptor's centre of gravity, δ_{trim}, and associated aerodynamic forces, C_{Ltrim} and $C_{D_{trim}}$, are calculated.

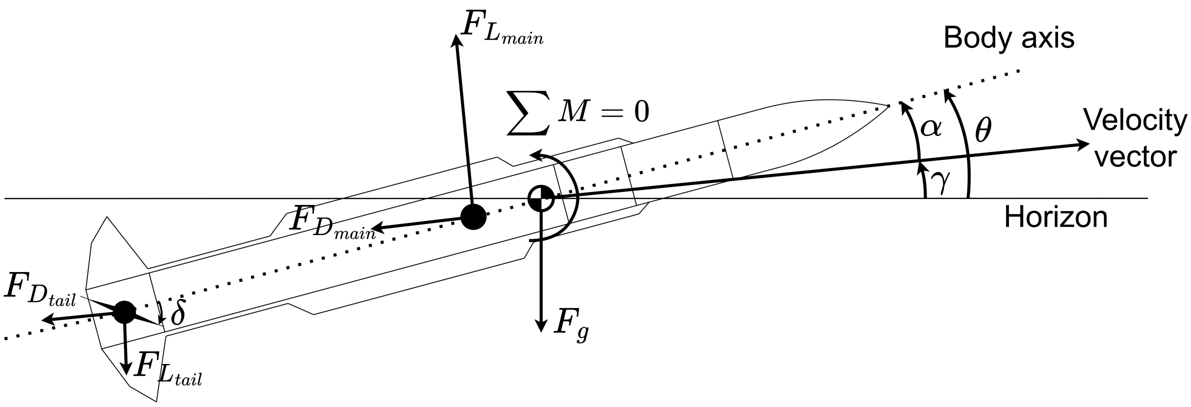

Figure 30: SM2 Free Body Diagram

3.3.2. Trimmed Aerodynamic Coefficient Database

Figure 31 to Figure 33 present the trimmed tailfin deflection angle δ_{trim}, lift coefficient $C_{L_{trim}}$, and drag coefficient $C_{D_{trim}}$ for combinations of Mach number and α_{trim} at centre of gravity locations of X_{CG} = 1.925 m, 2.387 m, and 2.567 m, respectively. The centre of gravity location of X_{CG} = 1.925 m corresponds to the empty interceptor's centre of gravity location and X_{CG} = 2.568 m and X_{CG} = 2.387 m correspond to the centres of gravity at the start and end of the boost phase.

In the upper-left subfigure of Figure 31, the trimmed tailfin deflection angle, δ_{trim}, becomes increasingly negative with an increase in angle of attack at each Mach number. As the main body experiences an increasingly stronger lift force at higher angles of attack, an increasingly stronger resulting restorative pitching moment tries to push the SM-2's nose back down. To keep the SM-2 flying at the desired trimmed angle of attack, the tailfins need to generate an increasingly stronger downward lift force to pitch the nose back up. With increasing Mach numbers, the maximum achievable trimmed angle of attack decreases.

The trimmed lift- and drag coefficients are presented in the upper-right and lower-left subfigures. A near-linear trend between the angle of attack and trimmed lift coefficient is observed, up to an angle of attack of α_{trim} = 25 degrees. Beyond 25 degrees, the lift coefficients first increase more strongly, before flattening off. These effects are most likely explained due to Missile DATCOM98 switching to a different solution strategy for $\alpha > 25°$ and are thus likely not the result of real-world aerodynamic effects. The maximum lift coefficient is $C_{L_{trim}}$ = 12.35 at an angle of attack of α_{trim} = 48 degrees and a Mach number of Ma = 1.0. The drag coefficient increases exponentially with an increase in angle of attack at every Mach number, as is expected.

The lower-right subfigure presents the L/D ratio at combinations of trimmed angle of attack and Mach number. It is immediately clear that at Mach numbers of Ma = 1.0 and Ma = 1.5, the maximum L/D ratio is lower than at subsonic and high-supersonic Mach numbers. The interceptor achieves a maximum L/D ratio of 2.9 at an angle of attack of α_{trim} = 10 degrees at a Mach number of Ma = 4.25. The lowest maximum L/D ratio is 2.2 at an angle of attack of α_{trim} = 16 degrees and a Mach number of Ma = 1.5.

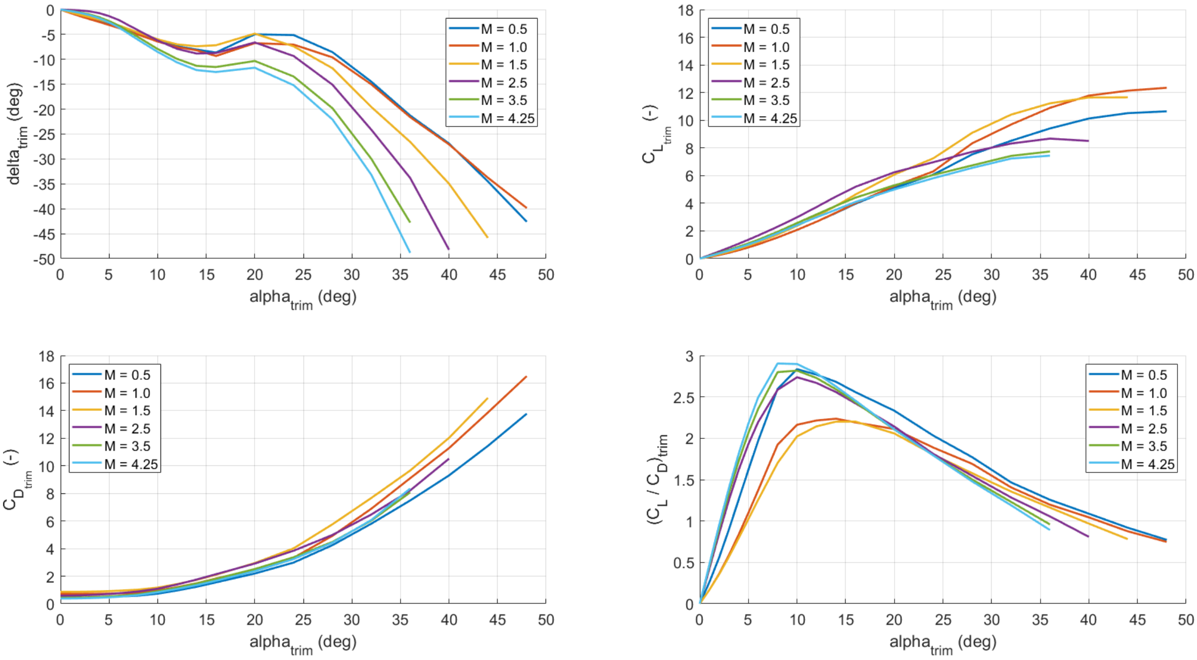

Figure 31: Trimmed tailfin deflection angle δ_{trim} and trimmed aerodynamic coefficients $C_{L_{trim}}$, $C_{D_{trim}}$, and L/D ratio for X_{CG} = 1.925 m

Figure 32 presents the trimmed tailfin deflection angle, lift coefficient, drag coefficient, and L/D ratio at combinations of angle of attack and Mach number for a centre of gravity position of X_{CG} = 2.387 m. In the upper-left subfigure, it becomes immediately clear that the tailfin deflection angle does not monotonously decrease with an increase in angle of attack. For Mach numbers of Ma = 2.5 and higher, the trimmed tailfin deflection angle is positive up to α_{trim} = 35 to 40 degrees, indicating that for these conditions, the centre of pressure of the main body lies in front of the centre of gravity of X_{CG} = 2.387 m. The interceptor is statically unstable and the tailfins need to actively work to keep the nose pushed down. At larger angles of attack, the tailfin deflection angles become negative at all Mach numbers, except at Ma = 0.5. The excessive 'up-and-down' behaviour of the required trimmed tailfin deflection angle as a function of angle of attack at Ma = 0.5 shows the inherent solver limitations of Missile DATCOM98. At each Mach number, the SM-2 can be successfully trimmed at angles of attack up to α_{trim} = 48 degrees, with the required trimmed tailfin deflection angle not exceeding δ_{trim} = plus minus 20 degrees.

The trimmed lift coefficients are plotted in the upper-right subfigure. The maximum lift coefficient has increased to $C_{L_{trim}}$ = 17.45 at an angle of attack of α_{trim} = 48 degrees and a Mach number of Ma = 1.5. Because the tailfins need to provide less downward lift to generate a pitch-up moment as the centres of pressure and centre of gravity are positioned closer together than for X_{CG} = 1.925 m, the airframe is aerodynamically more efficient. Again, the drag coefficient increases exponentially with the angle of attack, as is expected.

The lift-to-drag ratio L/D is plotted in the lower-right subfigure. The maximum L/D ratio has increased to 3.1 at an angle of attack of α_{trim} = 12 degrees at a Mach number of Ma = 0.5 and at an angle of attack of α_{trim} = 10 degrees at a Mach number of Ma = 4.25. At Mach numbers of 1.0 and 1.5, a reduction in aerodynamic efficiency can still be observed, with the lowest maximum L/D ratio being 2.4 at an angle of attack of α_{trim} = 14 degrees and a Mach number of Ma = 1.5.

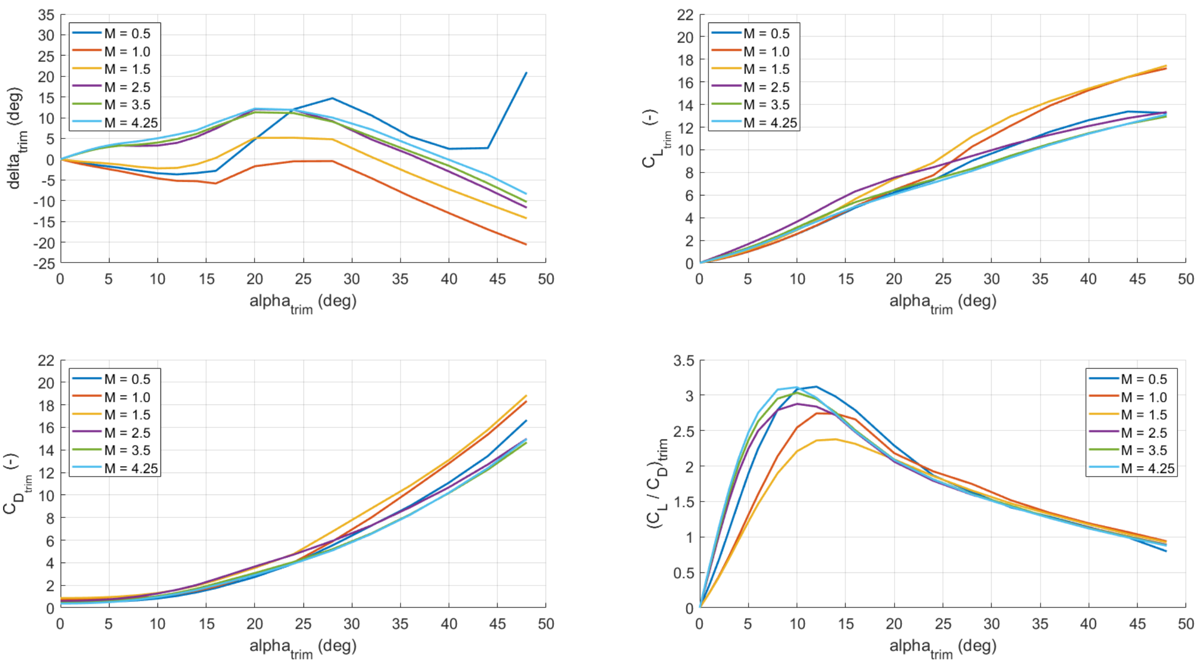

Figure 32: Trimmed tailfin deflection angle δ_{trim} and trimmed aerodynamic coefficients $C_{L_{trim}}$, $C_{D_{trim}}$, and L/D ratio for X_{CG} = 2.387 m

Figure 33 presents the trimmed aerodynamic conditions for combinations of trimmed angle of attack and Mach number at a centre of gravity location of $X_{CG} = 2.568$ m. Considering the centre of gravity is positioned even further aft than at $X_{CG} = 2.387$, the required δ_{trim} to achieve trimmed conditions is also more positive. The SM-2 is statically more unstable than at $X_{CG} = 2.568$ m. At a Mach number of $Ma = 0.5$, the maximum achievable trimmed angle of attack is $\alpha_{trim} = 24$ degrees. This, however, is not a problem, as the only moment in time that the SM-2 has a centre of gravity position close to $X_{CG} = 2.568$, it is still in the vertical boost phase before midcourse guidance is turned on and has no angle of attack yet.

In the upper-right subfigure, the maximum lift coefficient has increased to $C_{L_{trim}} = 18.75$ at an angle of attack of $\alpha_{trim} = 48$ degrees and a Mach number of $Ma = 1.0$. The maximum lift-to-drag coefficient in the lower-right subfigure is 3.1 at an angle of attack of $\alpha_{trim} = 10$ degrees and a Mach number of $Ma = 0.5$.

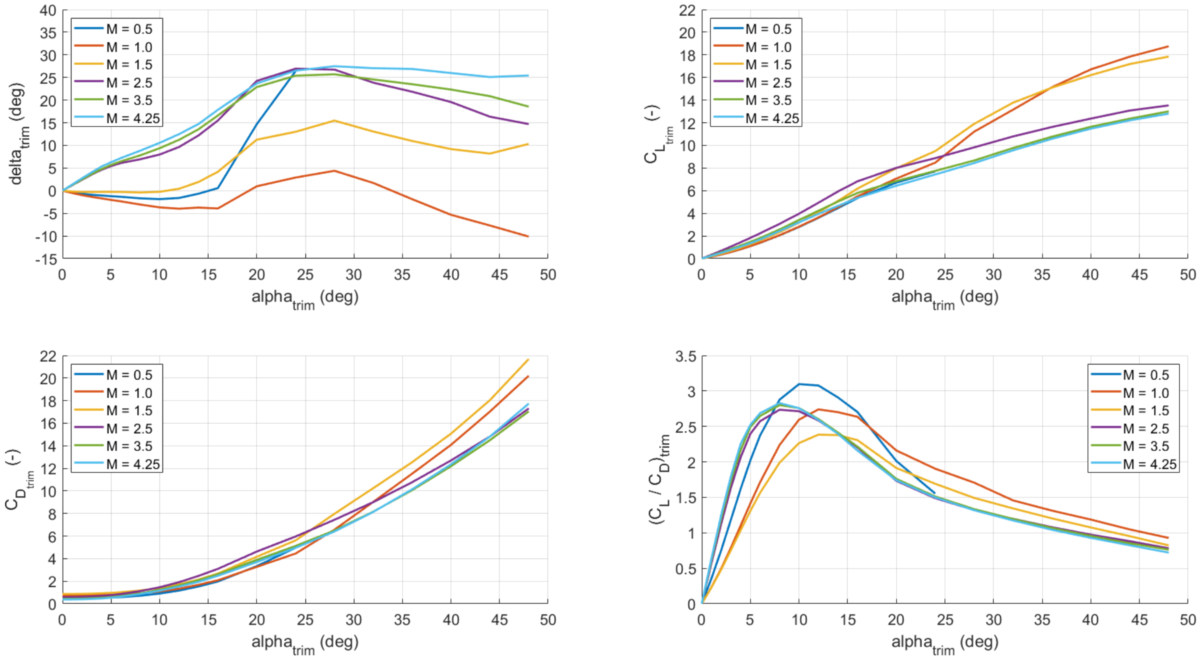

Figure 33: Trimmed tailfin deflection angle δ_{trim} and trimmed aerodynamic coefficients $C_{L_{trim}}$, $C_{D_{trim}}$, and L/D ratio for $X_{CG} = 2.568$ m

3.4. Autopilot Design

The autopilot is part of the guidance loop seen in Figure 8. The autopilot translates acceleration commands generated by the guidance law into control surface deflections based on desired flight characteristics.

In this thesis, the autopilot is indirectly implemented in the Simulink model. As described in subsection 2.9, the "autopilot and acceleration response" section uses as inputs the flight altitude, Mach number, and total acceleration command and returns the first-order time-delay constant τ. Using the first-order time-delay constant τ, the airframe's response to the acceleration commands is modeled. To achieve this, a database is constructed that returns this time-delay constant τ for any combination of altitude, Mach number, and acceleration command for altitudes between 0 m and 40000 m, Mach numbers between 0.25 and 5.0, and acceleration commands from 0 g to 45 g. This section explains how the autopilot is modeled and how the first-order time-delay database is constructed.

The Standard Missile-2's autopilot in this thesis is designed as a three-loop autopilot and follows the design procedure found in Zarchan's book [32]. The acceleration commands of both the horizontal and vertical manoeuvre planes are added together, resulting in a 'total acceleration command'. To achieve this acceleration command, the interceptor has to fly at trimmed conditions in the direction of the total acceleration command. In case the commanded acceleration exceeds the maximum achievable acceleration command at $\alpha_{trim,max}$, the commanded acceleration is limited to what can be achieved at $\alpha_{trim,max}$. The pitch behaviour of the interceptor in the direction of the total acceleration command is modeled using three-loop autopilot described in this section. Because the kinematic model used in this report is a modified point mass model with no aerodynamic cross coupling, no aerodynamic roll moments are generated. The autopilot is thus limited to the pitch channel.

Zarchan implements an analytical approach to obtain the airframe's aerodynamic coefficients and their derivatives with respect to α and δ. In this report, Zarchan's analytical values for $C_{N_{trim}}$, C_M, α_{trim}, δ_{trim}, C_{N_α}, C_{N_δ}, C_{M_α}, and C_{M_δ} are replaced by the aerodynamic derivative database resulting from Missile DATCOM 98, as described in subsection 3.3.

3.4.1. Three-loop autopilot

Three-loop autopilots use two feedback loops to feed back the pitch rate $\dot{\theta}$ and the airframe acceleration n_{ach}. Figure 34 presents the autopilot with airframe response transfer functions as described by Zarchan [32]. The acceleration command n_c is the input of the system and the output is the achieved acceleration n_{ach}. This model assumes that the airframe aerodynamics are represented by transfer functions based on the interceptor's aerodynamic coefficients and their derivatives; $C_{N_{trim}}$, C_M, C_{N_α}, C_{M_α}, C_{N_δ}, and C_{M_δ} at a given α_{trim} and δ_{trim}, which are obtained from the aerodynamic database presented in subsection 3.3.

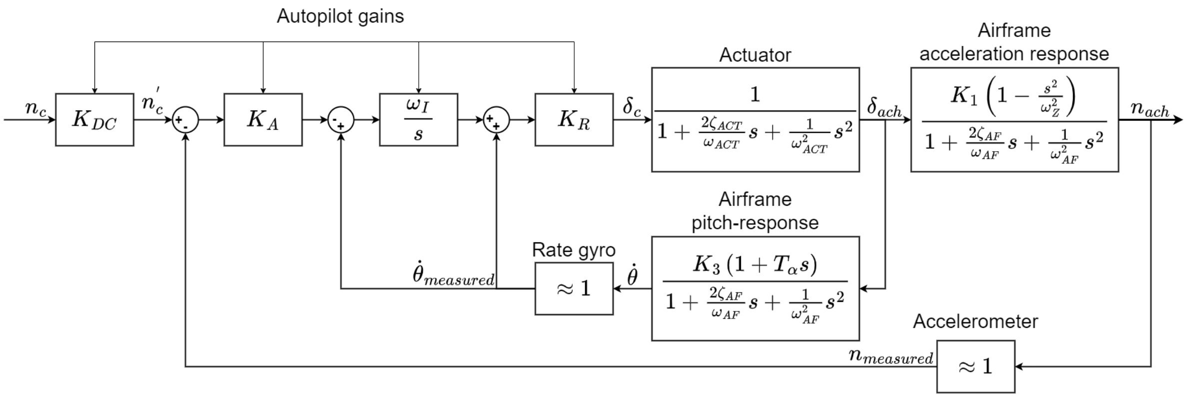

Figure 34: Three-loop autopilot block diagram. Author-made copy of original figure found in Zarchan [32]. Includes transfer function for actuator response.

3.4.2. Calculating autopilot gains K_{DC}, K_A, ω_I, and K_R

The three-loop autopilot model in Figure 34, together with the interceptor's aerodynamic coefficients and their derivatives with respect to α and δ at α_{trim} and δ_{trim} and the interceptor's mass and moment of inertia are used to calculate the autopilot gains K_{DC}, K_A, ω_I, and K_R and to represent the airframe dynamics through transfer functions.

The procedure to calculate the three-loop autopilot gains is presented in Equation 44 to Equation 59 [32]. The procedure is a synthesis of the algebraic manipulations found in chapters 22 and 23 of Zarchan's book and serves as a straight-to-the-point set of equations that, when implemented and calculated in the correct order, results in the autopilot gains.

For this procedure, it is assumed the aerodynamic force- and moment coefficient derivatives are represented by subsection 3.3. First, the airframe zero ω_z, the aerodynamic acceleration gain K_1, the aerodynamic body rate gain K_3, the turning rate constant T_α and the airframe's natural frequency ω_{AF} and damping ζ_{AF} are calculated using [32]:

$$\omega_z = \sqrt{\frac{M_\alpha N_\delta - M_\delta N_\alpha}{N_\delta} \cdot \frac{1}{I_y}} \tag{44}$$

$$K_1 = -\frac{1}{m}\frac{M_\alpha N_\delta - M_\delta N_\alpha}{M_\alpha} \tag{45}$$

$$K_3 = \frac{K_1}{V_M} \tag{46}$$

$$T_\alpha = mV_M \frac{M_\delta}{M_\alpha N_\delta - M_\delta N_\alpha} \tag{47}$$

$$\omega_{AF} = \sqrt{-\frac{M_\alpha}{I_y}} \tag{48}$$

$$\zeta_{AF} = \frac{N_\alpha \omega_{AF}}{2M_\alpha} \cdot \frac{I_y}{mV_M} \tag{49}$$

The intermediary values ω, ω_0, ζ_0, and K_0 are calculated as shown in Equation 50 to Equation 53 [32]:

$$\omega = \frac{\left[\tau\omega_{CR}\left(1 + \frac{2\zeta_{AF}\omega_{AF}}{\omega_{CR}}\right) - 1\right]}{(2\zeta\tau)} \tag{50}$$

$$\omega_0 = \frac{\omega}{\sqrt{\tau\omega_{CR}}} \tag{51}$$

$$\zeta_0 = 0.5\omega_0 \left[\frac{2\zeta}{\omega} + \tau - \frac{\omega_{AF}^2}{\omega_{CR}\omega_0^2}\right] \tag{52}$$

$$K_0 = \frac{-\omega^2}{\tau\omega_{AF}} \tag{53}$$

The second set of intermediary values, K_C and K, are now calculated using Equation 54 and Equation 55 [32]:

$$K_C = \frac{-\left(\frac{\omega_0^2}{\omega_z^2}\right) - 1 + 2\zeta_0\omega_0 T_\alpha}{1 - 2\zeta_0\omega_0 T_\alpha + \omega_0^2 T_\alpha^2} \tag{54}$$

$$K = \frac{K_0}{K_1(1 + K_C)} \tag{55}$$

Finally, the autopilot gains K_{DC}, K_A, ω_I, and K_R are calculated [32]:

$$K_{DC} = 1 + K_C \tag{56}$$

$$K_A = \frac{K_3}{K_C K_1} \tag{57}$$

$$\omega_I = \frac{T_\alpha K_C \omega_0^2}{1 + K_C + \frac{\omega_0^2}{\omega_z^2}} \tag{58}$$

$$K_R = \frac{K}{K_A \omega_I} \tag{59}$$

3.4.3. Example airframe acceleration response graph

Figure 35 presents the interceptor's acceleration response to a 10g step-command at a flight speed of Mach 1.5 at an altitude of 5.0km. After 0.1318 seconds, the achieved acceleration response, visualized by the blue line, reaches 63% of the commanded acceleration. In the kinematic simulation, the airframe's acceleration response for this specific example is thus modeled as a first-order transfer function with a time-constant τ value of 0.1318 seconds. Similar simulations are run for any combination of altitude, Mach number, and acceleration command, the resulting value of τ is stored in the database.

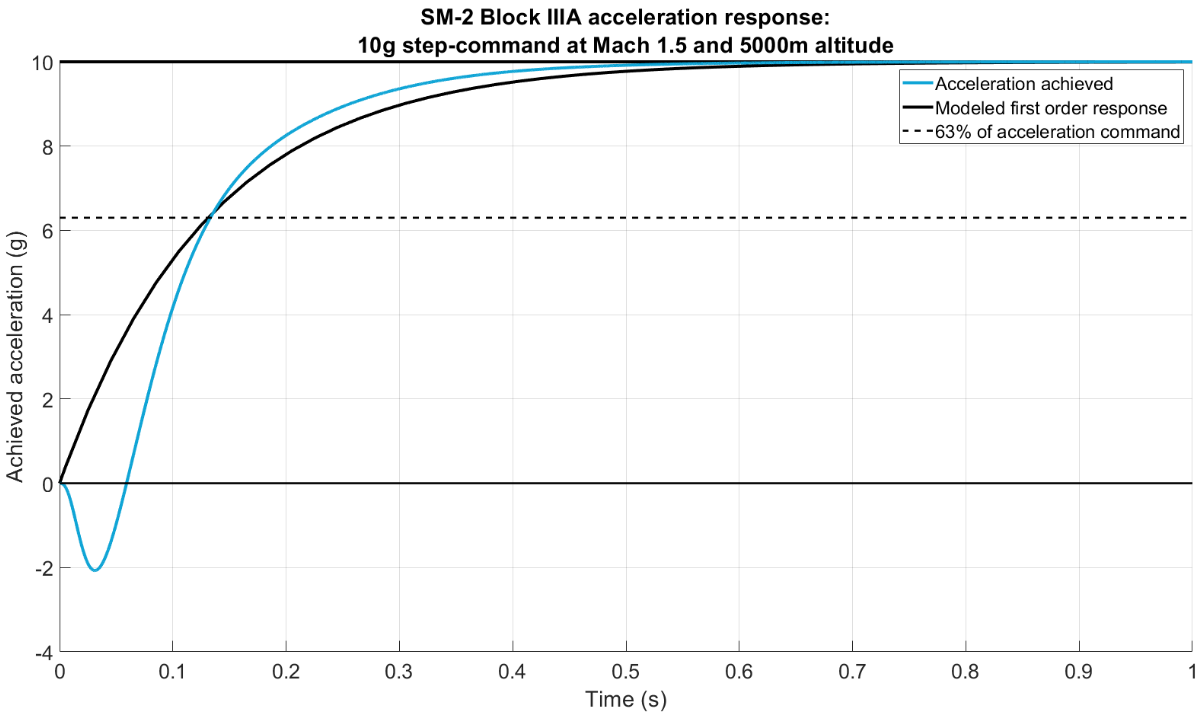

Figure 35: Acceleration response to a 10g step-command at an altitude of 5.0km and a speed of Mach 1.5. After 0.1318 seconds, the second-order response signal has reached 63% of the commanded value.

3.5. Threat descriptions

In the introduction, three threat types have been discussed: 1) Low and slow flying drones, 2) Low and fast flying Anti-Ship Cruise Missiles, and 3) High and fast flying targets. The Samad-2 and C-802 "Al-Mandab 2" are chosen as the "low and slow" and "low and fast" threats, respectively, due to their great relevance to the Houthi threat in the Red Sea. Additionally, the AS-5 "Kelt" is chosen to model a fast-flying, high-altitude target to develop engagement envelopes against.

3.5.1. Threat 1: Samad-2

The supervisor of this thesis, Dr. Savelsberg, together with Dr. Voskuijl and T. Dekkers, performed a flight performance analysis of the Samad-2 in the context of Houthi strikes against Saudi targets [43]. The Samad-2 has a ground cruise speed of 75 knots [43], translating to 38.5 meters per second and has a terrain-following cruising altitude of 250 meters [43]. The screenshot of the video of the French armed forces taking out a Houthi Samad-2 in the Red Sea in the introduction section of this report (Figure 4) shows the Samad-2 flying close to the surface, at an altitude much lower than 250 meters. Perhaps the drone was in its final phase of attack (the video insinuates the Samad-2 being close to impacting a commercial ship), and therefore flew close to the surface.

Two flight scenario's are created for the Samad-2 and shall be:

1. A cruise altitude of 10 meters and a velocity of 38.5 meters per second.
2. A cruise altitude of 250 meters and a velocity of 38.5 meters per second.

3.5.2. Threat 2: C-802 "Ghadir/Al-Mandab 2"

As discussed in the introduction section, the Anti-Ship Cruise Missile arsenal of the Houthi's consist of the "Noor" and "Ghadir"/"Al-Mandab 2" versions of the C-802 ASCM with ranges of 120km and 300km, respectively, as well as the "Sayyad" and "Quds Z-0" Anti-Ship versions of the Quds-1 LACM with ranges of 800km. The C-802 family of cruise missiles have a maximum velocity of Mach 0.9 and fly at a cruise altitude of 25 metres [7], [8]. The Quds family of cruise missiles fly at a slower speed of 735 km/h [7], translated to 204m/s, or Mach 0.6. It is therefore decided to use the Ghadir/Al-Mandab 2 versions of the C-802 cruise missile to model the Anti-Ship Cruise Missile threat, as encountering this missile type would be the "worst-case scenario" between the two cruise missile types.

The flight scenario for the C-802 Al-Mandab 2 shall be:

3. A cruise altitude of 25 meters and a velocity of 306 meters per second.

3.5.3. Threat 3: As-5 "Kelt"

The AS-5 "Kelt" is a Soviet-era cruise missile flying at a cruise speed of 1250 kilometers per hour (347 meters per second) at altitudes between 1.5 km and 10.0 km and has a maximum operational range of 220km [19].

Two flight scenarios are created for the AS-5 "Kelt" and shall be:

4. A cruise altitude of 1500 meters and a velocity of 347 meters per second.

5. A cruise altitude of 10000 meters and a velocity of 347 meters per second.

3.5.4. APAR Radar Horizon against flying targets

In order for a target to be tracked and illuminated by the radar on the ship, the target needs to be above the radar horizon. It needs to be calculated at what point the target crosses the radar horizon such that it can be detected, tracked, and illuminated.

The Air Defence and Command Frigates (ADCF's) of the Royal Netherlands Navy use the Thales Active Phased Array Radar (APAR) X-Band Multi-function radar with a maximum effective range of 150km to track and illuminate targets [44]. Targets can only be tracked and illuminated by the APAR once they are above the radar horizon. Using Figure 57 in appendix A.7, the APAR's height is estimated to be 27.25 meters above sea level.

The radar horizon (RH) as a function of radar and target height is given by [45]:

$$RH = \sqrt{2\frac{4}{3}R_0 \cdot H_R} + \sqrt{2\frac{4}{3}R_0 \cdot H_T}, \tag{60}$$

where RH is the radar horizon in km, R_0 is the Earth's radius in m, H_R is the radar height in m, and H_T is the target altitude in m.

Figure 36 presents the resulting radar horizon distance as a function of target altitude, including results for the Samad-2, Al-Mandab 2, and AS-5 Kelt.

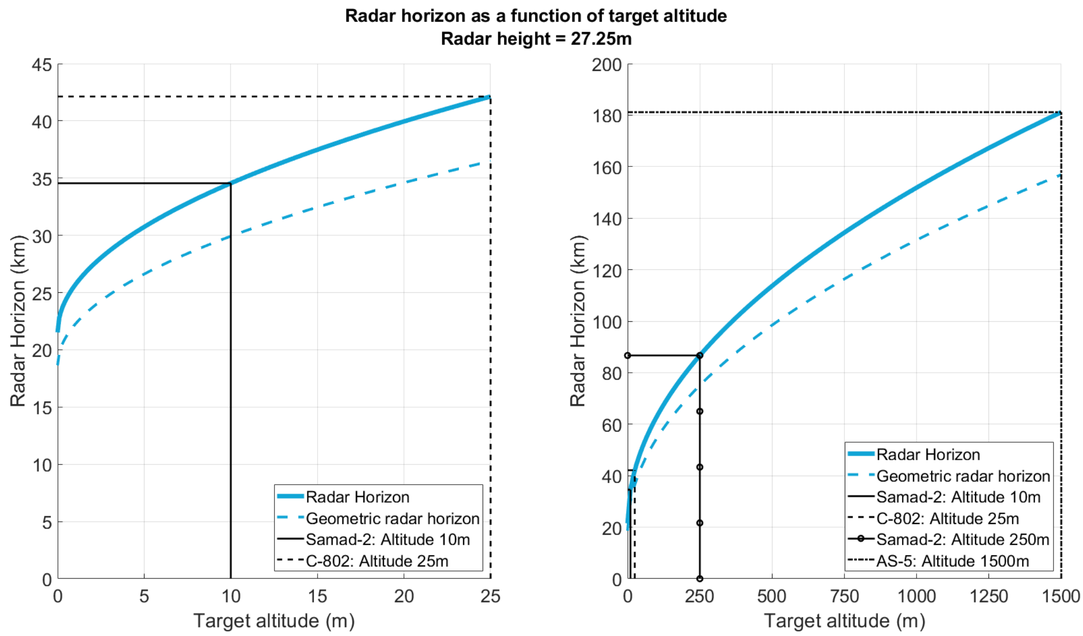

Figure 36: Radar horizon with atmospheric refraction and geometric radar horizon as functions of target altitude. Radar height: 27.25m above sea level.

Table 16 lists each target's name, flight altitude, and resulting radar horizon distance.

Threat name	**Flight altitude (m)**	**Radar horizon (km)**
Samad-2	10	34.6
C-802 Al-Mandab 2	25	42.1
Samad-2	250	86.7
AS-5 Kelt	1500	181.7
AS-5 Kelt	10000	433.7

Table 16: Flight altitudes and corresponding radar horizon distances for each threat scenario

4. Results

4.1. Flyout Tables and flyout trajectories

In this section, the resulting flyout tables and flyout trajectories of the SM-2 Block IIIA flying to specified Primary Command Points (PCP's) are presented. The interceptor is modeled flying towards each specified PCP using the selected Kappa guidance mode. At intercept, relevant information such as miss distance, interceptor velocity, Mach number, flight path angle, and the interceptor's position over time are saved. Flyout tables are then constructed presenting the time-to-intercept and interceptor Mach number at the PCP, as well as for the maximum divert capability and interceptor velocity at the PCP. Additionally, flyout trajectories are presented for multiple PCP's that intuitively visualize the interceptor's flyout behaviour, based on the specified intercept angles.

Flyout tables and flyout trajectories are presented for four Kappa guidance modes, listed below. From hence onwards, each mode will be referred to by its abbreviated name:

(1) KAP_NORM: Normal Kappa guidance - No specified interception angle at PCP

(2) KAP_NORM_75: Normal Kappa guidance - Specified interception angle at PCP: -75 degrees

(3) KAP_LONG: Long range mode - No specified interception angle at PCP

(4) KAP_LONG_75: Long range mode - Specified interception angle at PCP: -75 degrees

The resulting flyout tables and flyout trajectories for the four Kappa guidance modes are presented insubsubsection 4.1.1 to subsubsection 4.1.3. Flyout tables and flyout trajectories for a specified intercept angle of +45 degrees are presented in the appendix (Appendix A.8), as these results are not directly used for the engagement scenarios in this report.

4.1.1. Flyout tables: Time-to-intercept and Mach number

The time-to-intercept flyout tables, listed from Figure 37 to Figure 40, present the time-to-intercept and interceptor Mach number at intercept for Primary Command Points at any combination of downrange distance and altitude, provided the interceptor is kinematically able to reach the PCP. The resolution of the figures is 1 km by 1km. The black contour lines denote the time-to-intercept contour lines and the colored surface plot displays the local Mach number at intercept of the PCP.

Figure 37 presents the time-to-intercept and local Mach number at intercept for the SM-2 implementing Kappa guidance with no specified intercept angle, mode KAP_NORM. The interceptor achieves a maximum ground range of 83 km and the minimum engagement distance against sea-skimming targets is 9 km. Due to the figure's resolution, a maximum range of 81 km is visualised at an altitude of 1 km. At altitudes of 15 km to 20 km, the maximum service ceiling of most modern fighter jets, the SM-2 has a maximum range of 62 km. The SM-2's maximum local burnout velocity, achieved when flying perfectly vertically for the first 16 seconds of flight, is Mach 4.4. This translates to a sea-level adjusted Mach number of 3.8. The SM-2 is shown to be kinematically able to reach altitudes of 35 km. However, due to the air density at such high altitudes, the interceptor will not be able to manoeuvre, as is further discussed in subsubsection 4.1.2.

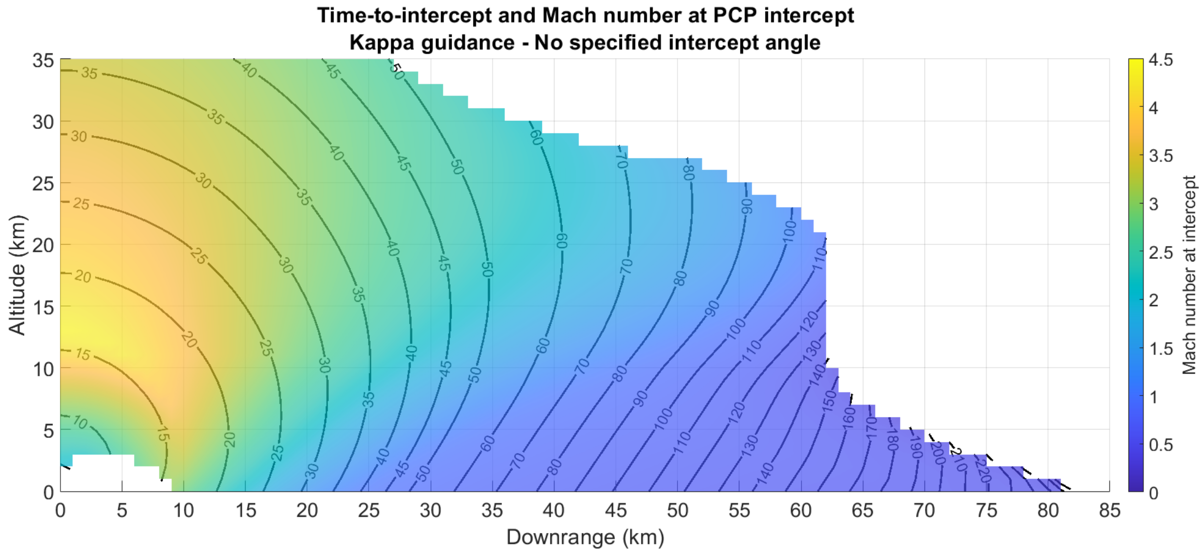

Figure 37: Time-to-intercept and interceptor Mach number at PCP intercept for Kappa guidance with no specified intercept angle. Time-to-intercept contour lines are constructed every 5 seconds for time-to-intercept = [5:50] seconds and every 10 seconds for time-to-intercept = [50:280] seconds.

Figure 38 presents the time-to-intercept and Mach number at intercept flyout table for KAP_NORM_75. Comparing KAP_NORM_75 to KAP_NORM, the maximum range

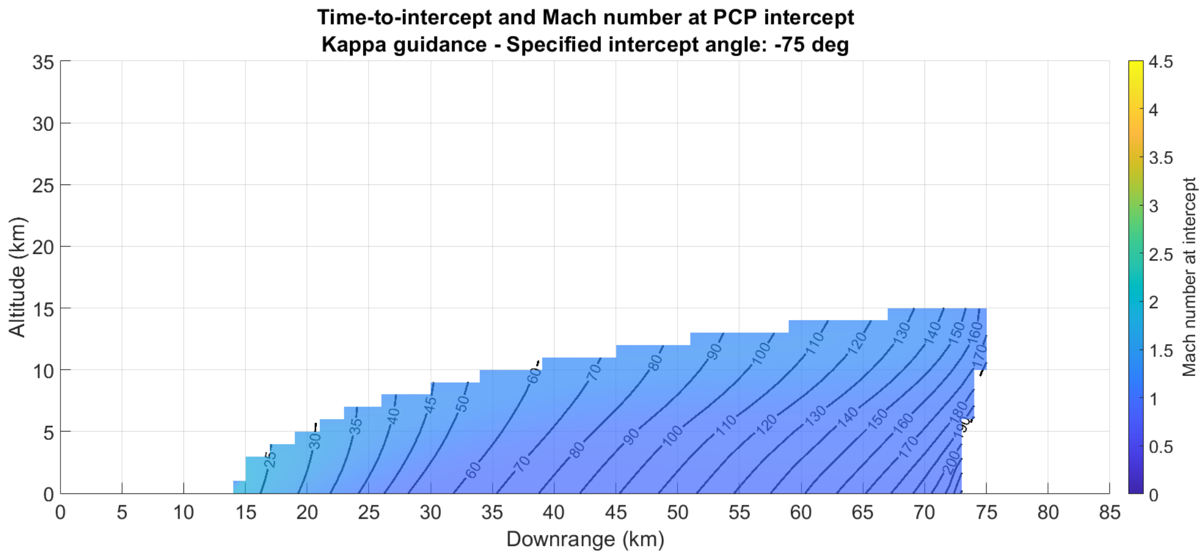

Figure 38: Time-to-intercept and interceptor Mach number at PCP intercept for Kappa guidance with a specified intercept angle of -75 degrees. Time-to-intercept contour lines are constructed every 5 seconds for time-to-intercept = [25:50] seconds and every 10 seconds for time-to-intercept = [50:230] seconds.

against sea-skimming targets is reduced to 73 km, although at altitudes of 10 km to 15 km, the maximum range has increased from 62 km to 75 km. The minimum engagement distance against sea-skimming targets has increased from 9 km to 14 km. The flyout table's boundary at the left-hand side of the flyout contour is the result of the guidance algorithm not yet being able to properly shape the flyout trajectory without unacceptable miss distances. In the region where KAP_NORM and KAP_NORM_75 both have successful intercepts, the overall Mach number for KAP_NORM_75 is higher. KAP_NORM_75 forces the SM-2 to remain at higher altitudes throughout its flight, before pitching down and flying trough the PCP at the desired intercept angle. Overall, the time-to-intercept contour lines are very similar between KAP_NORM and KAP_NORM_75.

Figure 39 presents the time-to-intercept and Mach number flyout table for KAP_LONG. Compared to the default flyout table, KAP_NORM, the maximum range against sea- skimming targets has increased greatly to 173 km. Due to the 1 km by 1 km resolution of the figure, the maximum displayed range is 169 km against targets at 1 km altitude. At altitudes of 10 km to 20 km, the maximum service ceiling of most modern fighter jets, the SM-2 has a maximum range of 130 km to 150 km. The minimum intercept distance against ground targets has increased to 29 kilometers. The constant 3g pitch-over manoeuvre during the initial 25 seconds of flight positions the interceptor at an altitude of 18.1 km and a downrange position of 12.9 km, displayed as the left-most point of the flyout table. During this pitch-over manoeuvre, the burnout Mach number at 16 seconds is Mach 4.3, translated to a ground Mach number of 3.7. Comparing the time-to-intercept contour lines of KAP_LONG to KAP_NORM and KAP_NORM_75, KAP_LONG results in a shorter time-to-intercept from a downrange distance of 40 km onward at all altitudes. KAP_LONG greatly increases the Mach number at intercept at all altitudes for downrange distances greater than 30 km.

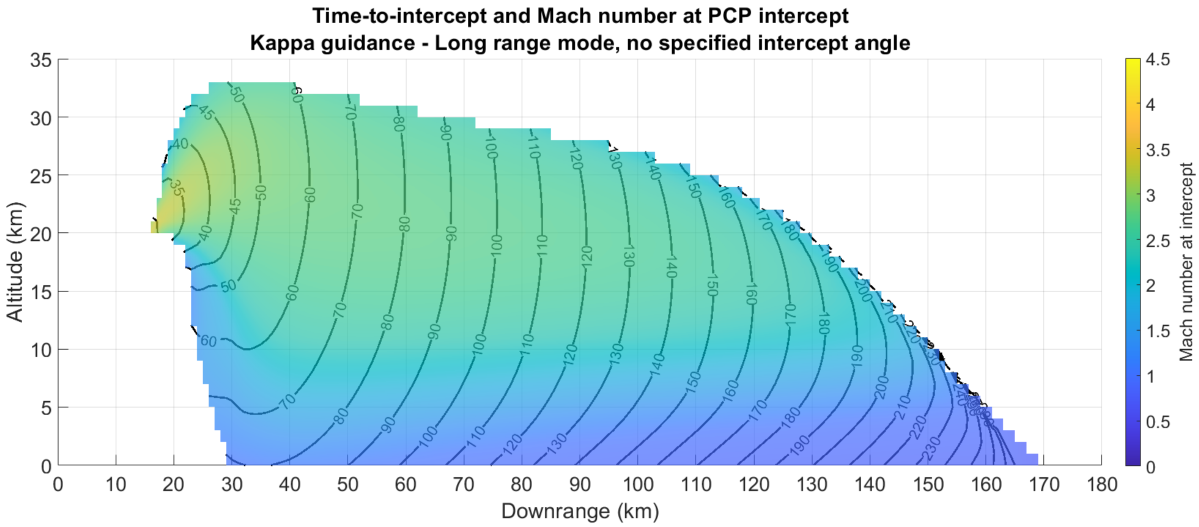

Figure 39: Time-to-intercept and interceptor Mach number at PCP intercept for long range mode Kappa guidance with no specified intercept angle. Time-to-intercept contour lines are constructed every 5 seconds for time-to-intercept = [30:50] seconds and every 10 seconds for time-to-intercept = [50:280] seconds. NOTE: Axis aspect ratio is 2:1.

Figure 40 presents the time-to-intercept and Mach number at intercept flyout table for KAP_LONG_75. Comparing KAP_LONG_75 to KAP_NORM_75, the maximum range against sea-skimming targets has increased from 73 to 141 km. The minimum intercept range against sea-skimming targets has also increased, from 14 km to 26 km. Similar to KAP_NORM_75, the upper boundary in Figure 40 is the result of the guidance algorithm not being able to properly shape the flyout trajectory without unacceptable miss distances. For downrange distances of 40 km and greater, the time-to-intercept for KAP_LONG_75 is less than KAP_NORM_75 at all altitudes. The long-range mode greatly increases the Mach number at PCP intercept at all altitudes starting at a downrange distance of 30 km.

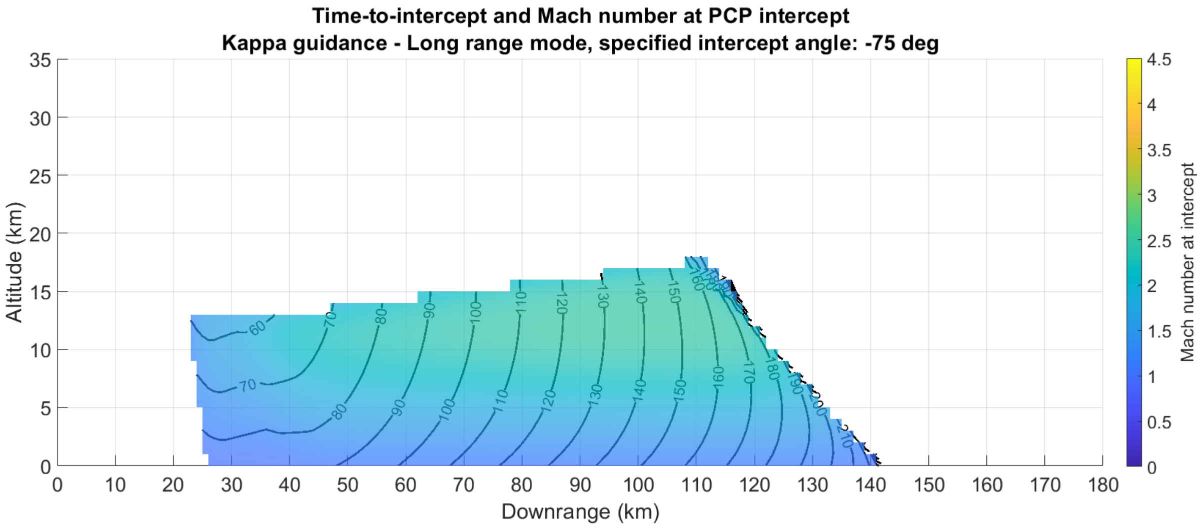

Figure 40: Time-to-intercept and interceptor Mach number at PCP intercept for long range mode Kappa guidance with a specified intercept angle of -75 degrees. Time-to-intercept contour lines are constructed every 10 seconds for time-to-intercept = [60:220] seconds. NOTE: Axis aspect ratio is 2:1.

4.1.2. Flyout tables: Remaining divert capability and velocity

The divert capability flyout tables, listed from Figure 41 to Figure 44, present the SM-2's remaining divert capability in g's and interceptor velocity at PCP intercept. The resolution of the figures is 1 km by 1 km. The black contour lines denote the remaining divert capability contour lines and the colored surface plot displays the interceptor velocity at PCP intercept. Divert capability contour lines are given up to 45 g's, as this is the SM-2's assumed maximum allowed acceleration command. The remaining maximum divert capability at intercept is an important performance metric for guided missiles, as targets may employ evasive manoeuvres to avoid being intercepted. Therefore, it is important to know not only if a target can be reached, but how much manoeuvrability the interceptor has left. The interceptor should always have a manoeuvrability advantage over the target.

Figure 41 presents the SM-2's maximum remaining divert capability and interceptor velocity at PCP intercept for KAP_NORM. At its maximum range of 83 km, the SM-2 has a remaining manoeuvrability of 4 g. Non-manoeuvring targets, such as very slow flying drones that do not have radar warning receivers that initiate evasive manoeuvres) can theoretically still be intercepted. Very manoeuvrable, high-value targets, such as fighter jets, can only be intercepted with a 3:1 divert ratio advantage up to a downrange distance of 20-25 km. Though the SM-2 using KAP_NORM can kinematically reach altitudes of 30-35 km, it only has a remaining divert capability of around 1 g due to the very thin air at such high altitudes, notwithstanding a very sluggish acceleration response from the airframe acceleration response section.

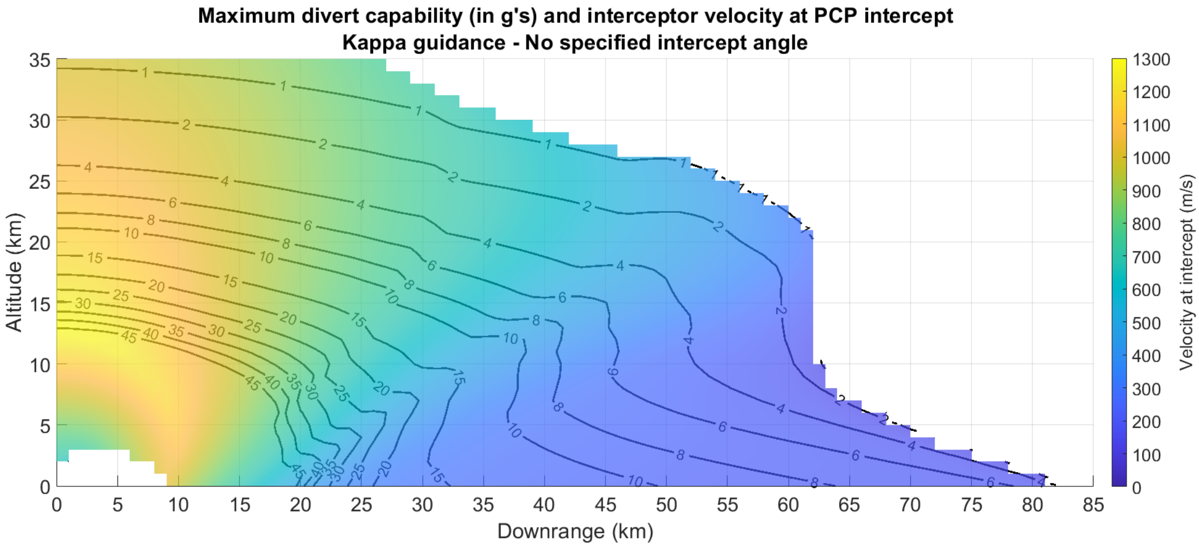

Figure 41: Maximum divert capability (in g's) and interceptor velocity at PCP intercept for Kappa guidance with no specified intercept angle. Maximum divert contour lines are constructed at maximum divert = 1g, every 2 g's for maximum divert = [2:10], and every 10 g's for maximum divert = [15:45].

Figure 42 presents the remaining divert capability and interceptor velocity at PCP intercept for KAP_NORM_75. Comparing the divert capability contour lines to KAP_NORM, it is immediately clear that KAP_NORM_75 retains a higher maximum divert capability in the region where both KAP_NORM and KAP_NORM_75 have successful PCP intercepts.

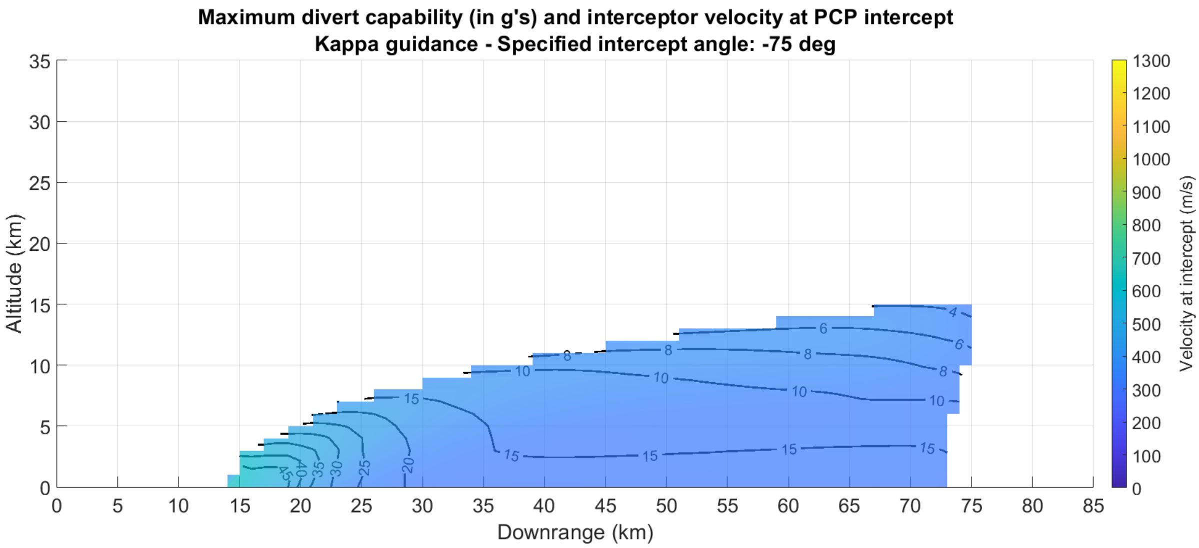

Figure 42: Maximum divert capability (in g's) and interceptor velocity at PCP intercept for Kappa guidance with a specified intercept angle of -75 degrees. Maximum divert contour lines are constructed at maximum divert = 1g, every 2 g's for maximum divert = [2:10], and every 10 g's for maximum divert = [15:45].

Against sea-skimming targets, the SM-2 retains a maximum divert capability of more than

15 g's up to its maximum engagement distance of 73 km, compared to KAP_NORM's maximum divert capability against sea-skimming targets falling below 15 g's after a downrange distance of 33 km and having a divert capability against sea-skimming targets at 70 km downrange of only 6 to 8 g's.

Figure 39 presents the remaining divert capability and interceptor velocity at PCP intercept for KAP_LONG. Besides a significant increase in operational range compared to KAP_NORM, the SM-2's remaining divert capability throughout the flyout envelope remains significant below altitudes of 20 km. At its maximum ground range of 173 km, the SM-2 retains a divert capability of 10 g's. At an altitude of 10 km, around the service ceilings of AWACS platforms, such as the Boeing E-3 Sentry or Beriev A-50, the SM-2 retains a divert capability of 14 to 15 g's up to a downrange distance of 150 km. The SM-2 has a divert capability of around 6 g's at an altitude of 20 km, reducing to 2 to 4 g's at an altitude of 25 km. The SM-2 could theoretically intercept non- or barely manoeuvring targets cruising at 25 km altitude out to distances of 100 to 110 km.

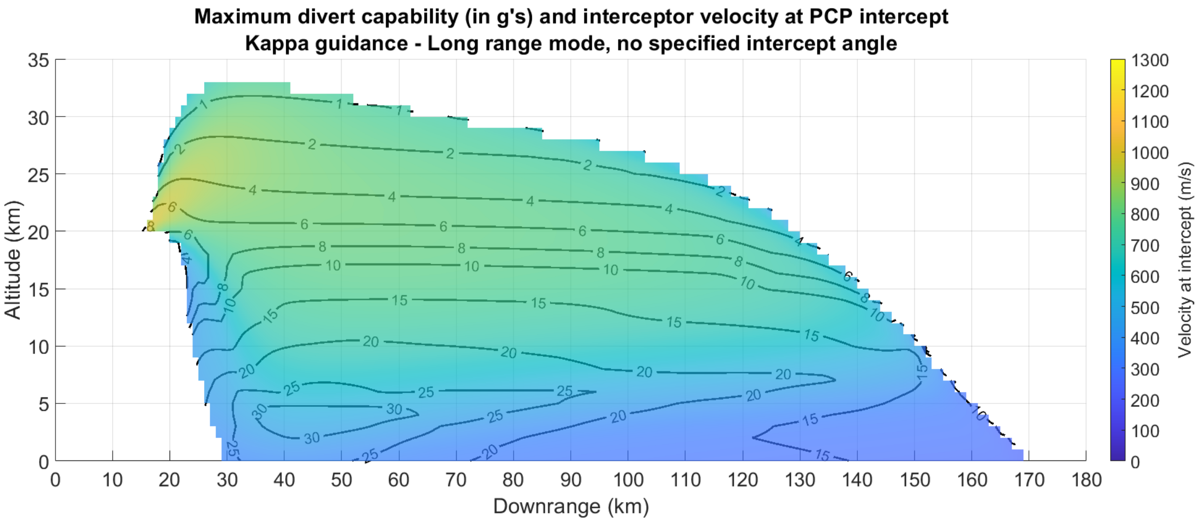

Figure 43: Maximum divert capability (in g's) and interceptor velocity at PCP intercept for long range mode Kappa guidance with no specified intercept angle. Maximum divert contour lines are constructed at maximum divert = 1g, every 2 g's for maximum divert = [2:10], and every 10 g's for maximum divert = [15:45].

Figure 44 presents the remaining divert capability and interceptor velocity at PCP intercept for KAP_LONG_75. Starting at a downrange distance of 40km, using KAP_LONG_75 results in the SM-2 retaining a larger divert capability at PCP intercept than KAP_LONG in the region where both guidance modes result in intercepts. This is due to the shaping of the flyout trajectories, where KAP_LONG_75 keeps the interceptor at higher altitudes before pitching over sharply to fly through the PCP. Up to a ground range of 140 km, KAP_LONG_75 allows the SM-2 to intercept sea-skimming targets with a remaining divert capability of at least 25 g's. At an altitude of 5 km, the SM-2 is able to intercept targets out to a range of 130 km with at least 30 g's of remaining divert capability, meaning the interceptor retains a manoeuvrability advantage of more than 3:1 even over highly manoeuvrable fighter jets. At an altitude of 10 km, the divert capability stays above 20 g's out to a range of 120 km.

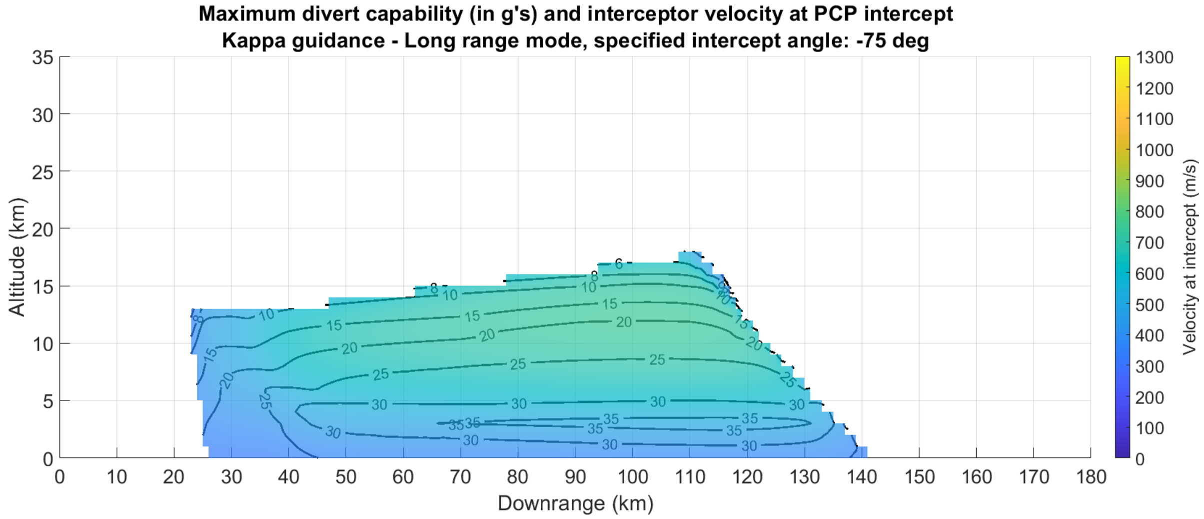

Figure 44: Maximum divert capability (in g's) and interceptor velocity at PCP intercept for long range mode Kappa guidance with a specified intercept angle of -75 degrees. Maximum divert contour lines are constructed at maximum divert = 1g, every 2 g's for maximum divert = [2:10], and every 10 g's for maximum divert = [15:45].

4.1.3. Flyout trajectories

The flyout trajectories towards each successfully intercepted Primary Command Point are saved for each Kappa guidance mode. Flyout trajectories are visualized to present the reader with an intuitive understanding of how the Standard Missile-2 implementing Kappa midcourse guidance flies out to intercept its targets.

Figure 45 presents flyout trajectories of the four Kappa guidance modes to a PCP located at sea level at a downrange distance of 35 kilometers, representing intercept trajectories against a static target at the APAR's radar horizon.

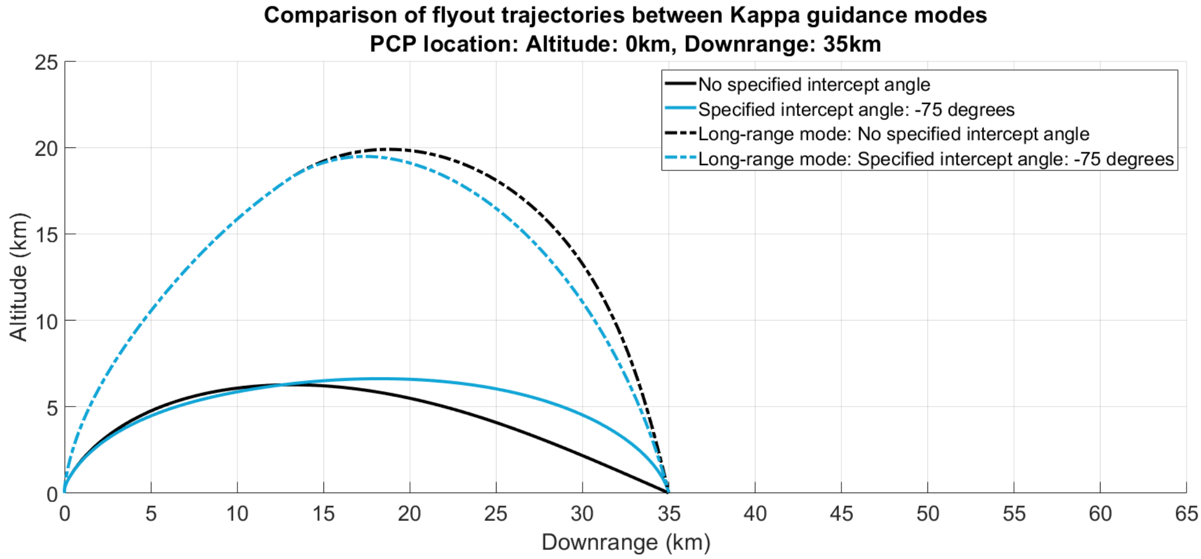

Figure 45: Comparison of flyout trajectories for Kappa guidance methods to the PCP located at 0 kilometers altitude and at a downrange distance of 35 kilometers, representing intercept trajectories against a static sea-level target at the APAR's radar horizon.

Comparing KAP_NORM to KAP_NORM_75, it is clear that after the vertical launch, KAP_NORM pitches the SM-2 over such that the resulting trajectory is aimed straight at the target, whereas KAP_NORM_75 keeps the SM-2 at higher altitudes, before sharply pitching over to intercept the PCP at the desired intercept angle. The two long-range guidance modes first make the interceptor gain significant altitude through the constant 3g pitch over manoeuvre for the first 25 seconds of flight, before pitching over further to intercept the specified PCP.

Figure 46 presents flyout trajectories of the four Kappa guidance modes to a PCP located at 10 kilometers altitude and a downrange distance of 60 kilometers, representing intercept trajectories against a target at 10 km altitude at the maximum range where all four guidance modes result in a successful intercept. Both KAP_NORM and KAP_LONG aim the interceptor directly at the PCP, whereas KAP_NORM_75 and KAP_LONG_75 keep the SM-2 at higher altitudes to achieve the desired intercept angle at intercept of -75 degrees.

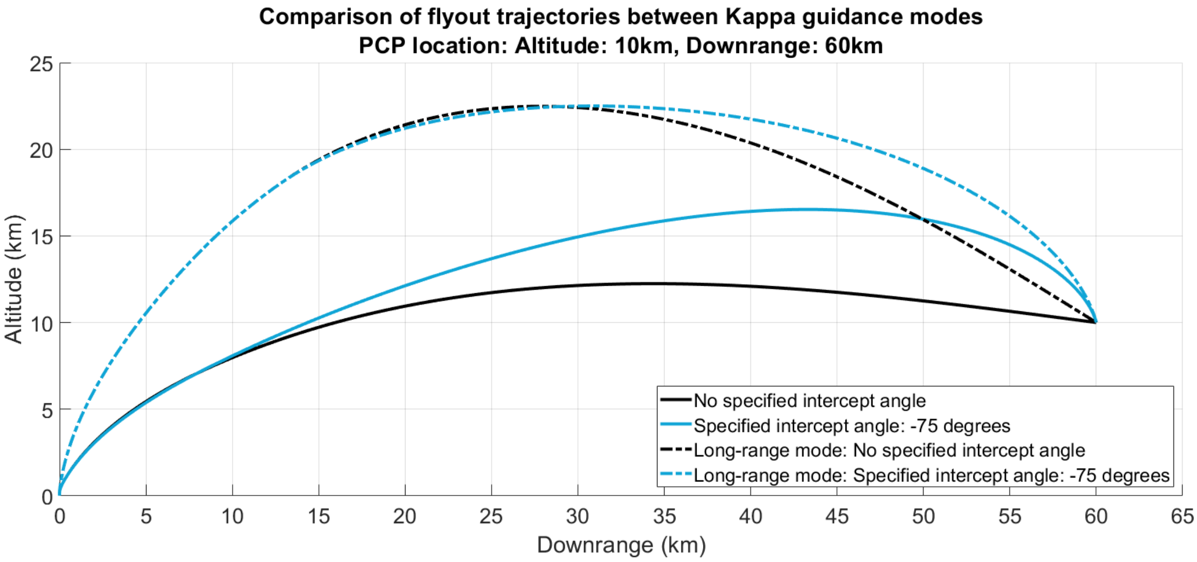

Figure 46: Comparison of flyout trajectories for Kappa guidance methods to the PCP located at 10 kilometers altitude and at a downrange distance of 60 kilometers, representing intercept trajectories against a high-altitude

4.2. Engagement Envelopes

Engagement envelopes are developed for the five threat types discussed in subsection 3.5. For each threat type, the engagement scenario is listed in Table 17. For each given threat engagement scenario, the individual targets are modeled to be dispersed over the target's respective radar horizon around the launching ship, from a bearing of 90° to 270° with respect to the threat's starting position in a head-on engagement. Figure 6 in the introduction presents a visual overview of the initialization of an engagement scenario and how the individual threats are dispersed over the radar horizon. The threats are dispersed at an interval of 1 degree, resulting in a total of 181 interception simulations per engagement scenario.

Scenario	Threat name	Cruise Altitude (m)	Cruise Speed (m/s)	Kappa guidance mode
1	Samad-2	10	38.5	KAP_NORM_75
2	Samad-2	250	38.5	KAP_LONG
3	C-802 Al-Mandab 2	25	306	KAP_NORM_75
4	AS-5 Kelt	1500	347	KAP_LONG_75
5	AS-5 Kelt	10000	347	KAP_LONG

Table 17: Threat name, cruise altitude, cruise speed, and specified intercept angle for each engagement scenario

In each interception simulation, the threat is initiated at its respective starting position on the radar horizon and flies "downward" (direction 180°). The threat is assumed to be detected and tracked instantly at the start of the simulation, without measurement errors. Using the time-to-intercept flyout table associated to the engagement scenario's specified Kappa midcourse flyout mode, the Primary Command Point is calculated and the Standard Missile-2 is launched towards the PCP. At an interceptor-to-target range of 6000 m, the SM-2 switches to gravity-compensated Proportional Navigation and manoeuvres to establish an intercept triangle in both manoeuvre planes.

For each individual interception simulation, the position-at-intercept in the LCIC frame and miss-distance are saved to determine whether the interception was successful or not. It is assumed that for miss distances of less than 10 meters, the SM-2 successfully intercepts the target. For each successful intercept, the intercept position is plotted, resulting in the engagement envelope for that engagement scenario.

4.2.1. Scenario 1: Samad-2 at cruise altitude 10m

Figure 47 presents the engagement envelope of the Standard Missile-2 Block IIIA against the Samad-2 flying at 10 m altitude. The SM-2 is guided towards the PCP by Kappa guidance with a specified intercept angle of -75 degrees. In the head-on engagement, the Samad-2 is intercepted at a ground range of 32.5 km after 60.8 seconds. Because the Samad-2 flies at very slow speeds, the Standard Missile-2 Block IIIA can intercept the Samad-2 even when detected at a large initial bearing. At an initial bearing of 85° and 275°, the Samad-2 is still intercepted within the radar horizon distance at a bearing of 90.3° and 269.7°, respectively.

The time-to-intercept of these interceptions simulations is 67.3 seconds. The engagement envelope nearly fully encompasses the area around the ship where the Samad-2 flying at 10 meters altitude can be detected.

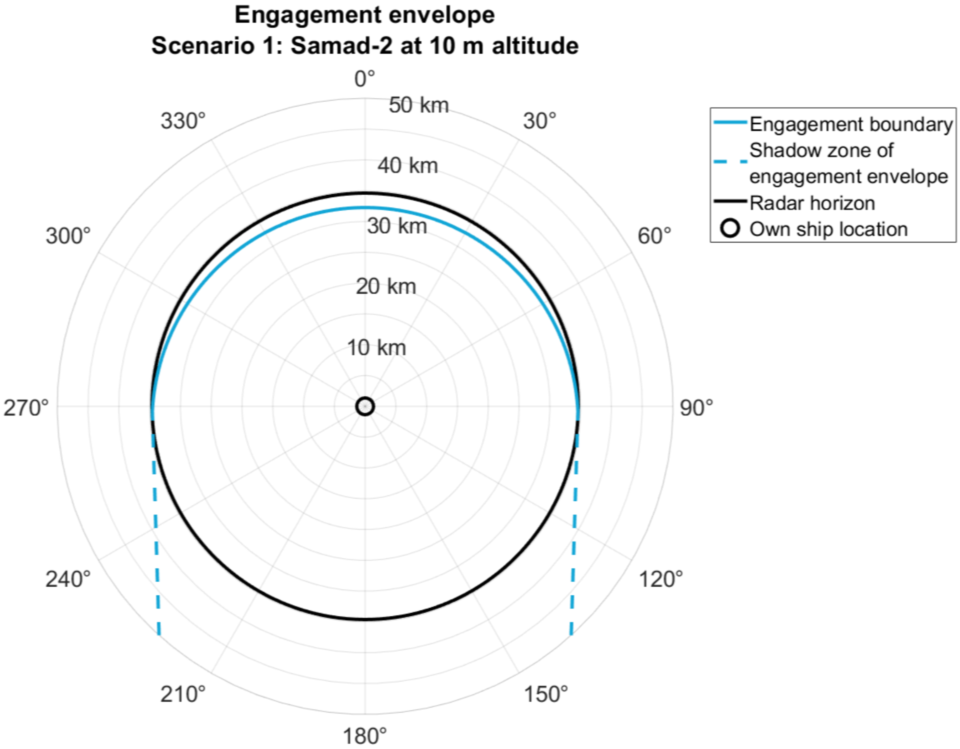

Figure 47: Engagement envelope for threat engagement scenario 1: Samad-2 at a cruise altitude of 10m and a cruise speed of 38.5m/s. Threats come in from the top of the figure and fly downward. Once the threat passes the radar horizon, it is immediately tracked and engaged with no delay.

4.2.2. Scenario 2: Samad-2 at cruise altitude 250m

Figure 48 presents the resulting engagement envelope of the SM-2 BlkIIIA intercepting the Samad-2 flying at a cruise altitude of 250 m. Compared to the Samad-2 flying at a cruise altitude of 10 m, the Samad-2 flying at 250 m altitude is initially detected at a much longer range of 86.7 km. Because the normal Kappa guidance modes KAP_NORM and KAP_NORM_75 can not reach targets out to 86.7 km, the long-range variant with no specified intercept angle, KAP_LONG, was used for midcourse guidance. Additionally, the fly-out table analysis in subsection 4.1 shows that KAP_LONG has a shorter time-to-intercept against ground targets than KAP_NORM and KAP_NORM_75 for ground distances greater than 40 km. At an intercept distance of roughly 80-85 km, close to, or exceeding the maximum range of KAP_NORM and KAP_NORM_75, there is a much shorter time-to-intercept when using KAP_LONG as the midcourse guidance mode.

In the head-on engagement, the Samad-2 is intercepted at a ground range of 81.5 km after 128.9 seconds. The SM-2 is able to engage and intercept the Samad-2 up to initial threat detection bearings of 88° and 272°. The threats are intercepted at the radar horizon distance of 86.7 km at bearings of 91.5° and 268.5°, respectively. For these simulations, the time-to-intercept is 135.6 seconds. Similar to the engagement scenario against the

Samad-2 flying at 10 m altitude, the engagement envelope nearly fully encompasses the area around the ship where targets flying at 250 m altitude can be detected.

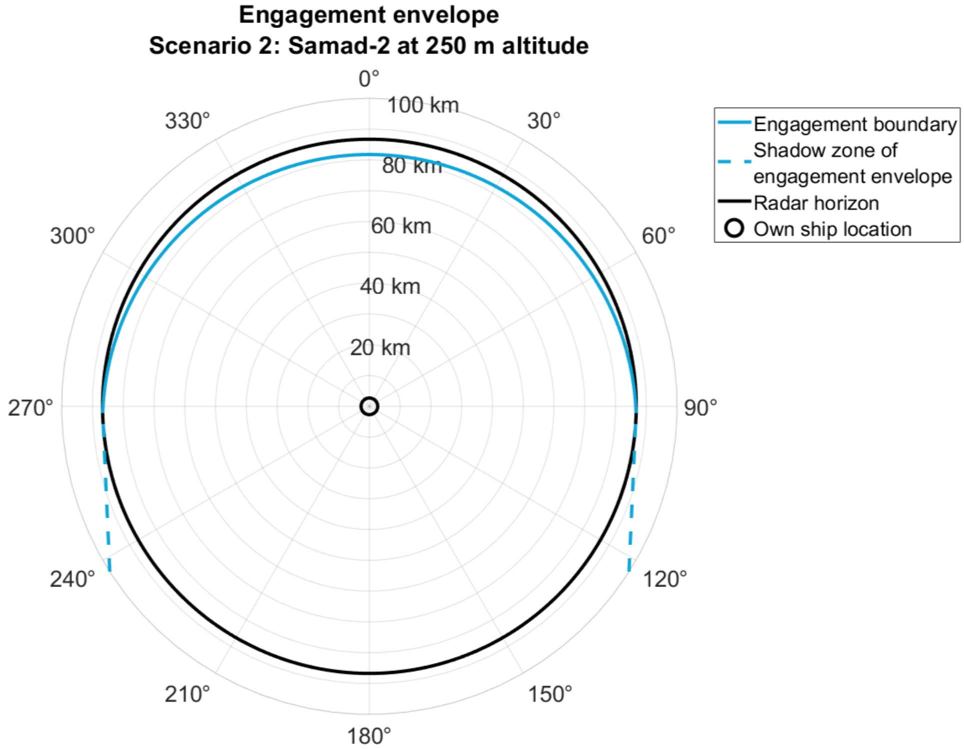

Figure 48: Engagement envelope for threat engagement scenario 2: Samad-2 at a cruise altitude of 250m and a cruise speed of 38.5m/s. Threats come in from the top of the figure and fly downward. Once the threat passes the radar horizon, it is immediately tracked and engaged with no delay.

4.2.3. Scenario 3: Al-Mandab 2 at cruise altitude 25m

Figure 49 presents the engagement envelope against the Al-Mandab 2 variant of the C-802 Anti-Ship Cruise Missile flying at a cruise altitude of 25 meters. The SM-2 uses the KAP_NORM_75 as the midcourse guidance mode to intercept the Al-Mandab 2 because in the Kappa guidance section, subsection 2.4, Boord and Hoffman recommend intercepting cruise missiles at a ground angle of 75 degrees [24]. Additionally, the maximum detection range against the Al-Mandab 2 flying at 25 m is 42.1 km, resulting in that the target falls well within the flyout table of KAP_NORM_75.

The Al-Mandab 2, flying at a cruise speed of 306 m/s, is much faster than the Samad-2 at 38.5 m/s. This difference becomes apparent when analysing the engagement envelope against the Al-Mandab 2. In the head-on scenario, the Al-Mandab 2 is intercepted at a ground range of 27.5 km after 47.9 seconds. If the SM-2 misses the threat during the first engagement, there is one more chance to engage the Al-Mandab 2 by immediately launching another SM-2 towards a PCP located at a downrange distance of 18.7 km, assuming no time is required to process and confirm a hit or a miss, which in the real world is not the case. If the SM-2 misses again, short-range defenses, such as the Evolved Sea Sparrow Missile, Rolling Airframe Missile or the Close-In Weapon System have to be engaged for self-defence.

In the (near-) perpendicular crossing target area-defence scenarios, the SM-2 can not engage and intercept the Al-Mandab 2 up to initial detection bearings as large as for the Samad-2. The SM-2 can engage the Al-Mandab 2 up to an initial detection bearing of 71° and 289°. In these scenarios, the Al-Mandab 2 is intercepted at a bearing of 109° and 251° after 89.9 seconds. The SM-2 intercepts the Al-Mandab 2 perpendicular to the threat's flight direction at bearings of 90° and 270° at a range of 36.1 km.

Overall, the engagement envelope against the Al-Mandab 2 is smaller than the engagement envelopes against the Samad-2. Regardless, as a rule of thumb, any to be defended asset placed 'behind' the launching ship (with respect to the threat vector) can be considered to be protected. If a frigate or destroyer were to be deployed in the Red Sea of Gulf of Aden to escort convoys, the ship should be placed between the convoy and the expected threat vector.

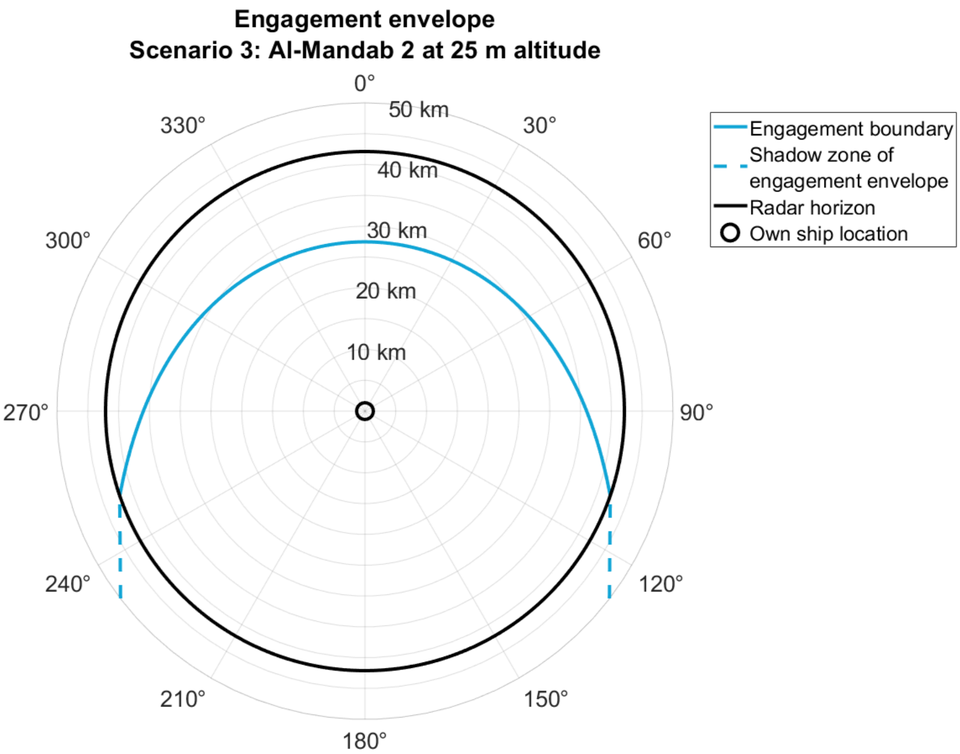

Figure 49: Engagement envelope for threat engagement scenario 2: Al-Mandab 2 at a cruise altitude of 25m and a cruise speed of 306 m/s. Threats come in from the top of the figure and fly downward. Once the threat passes the radar horizon, it is immediately tracked and engaged with no delay.

4.2.4. Scenario 4: AS-5 Kelt at cruise altitude 1500m

Figure 50 presents the engagement envelope against the AS-5 Kelt flying at a cruise speed of 347 m/s at an altitude of 1500 m. Though the radar horizon range for targets at an altitude of 1500 m is 181.7 km, the APAR's maximum effective range is 150 km. The AS-5 can thus only be tracked and illuminated once it is within 150 km of the ship. The *KAP_LONG_75* Kappa guidance mode is used to guide the SM-2 during the midcourse phase. *KAP_LONG_75* has a maximum range of 140 km against targets flying at an altitude of 1500m. However, as the SM-2 still has a remaining divert capability of 25 g's at a range of 140 km and threats are only engaged at these distances at the outermost regions of the engagement envelope, the KAP_LONG_75 guidance mode was chosen.

In the head-on engagement scenario, the AS-5 Kelt is intercepted at a ground range of 99.6 km after 145.3 seconds. If the first engagement results in a miss, there are two more opportunities to re-engage the threat before the AS-5 passes through the flyout table's minimum intercept range. In the unlikely scenario where this does happen, the short-range Kappa guidance modes KAP_NORM and KAP_NORM_75 can still be used to re-engage the threat within a ground range of 25 km.

Engaging crossing targets in area-defence is possible up to initial threat detection bearings of 59° and 301°. In these scenarios, the AS-5 Kelt is intercepted at a range of 129.1 km and bearings of 85.0° and 270.0°, respectively, after 189.9 seconds. For initial threat detection bearings between 59° and 65° (301° and 295°), the SM-2 is kinematically able to reach the target, but the miss distance is larger than 10 meters. The interceptor is unable to properly accelerate in both manoeuvre planes to achieve interception triangles, resulting in unacceptable miss distances. Perpendicular to the direction of flight of the AS-5 Kelt, at bearings of 90° and 270°, the SM-2 is able to provide coverage up to a range of 128.0 km.

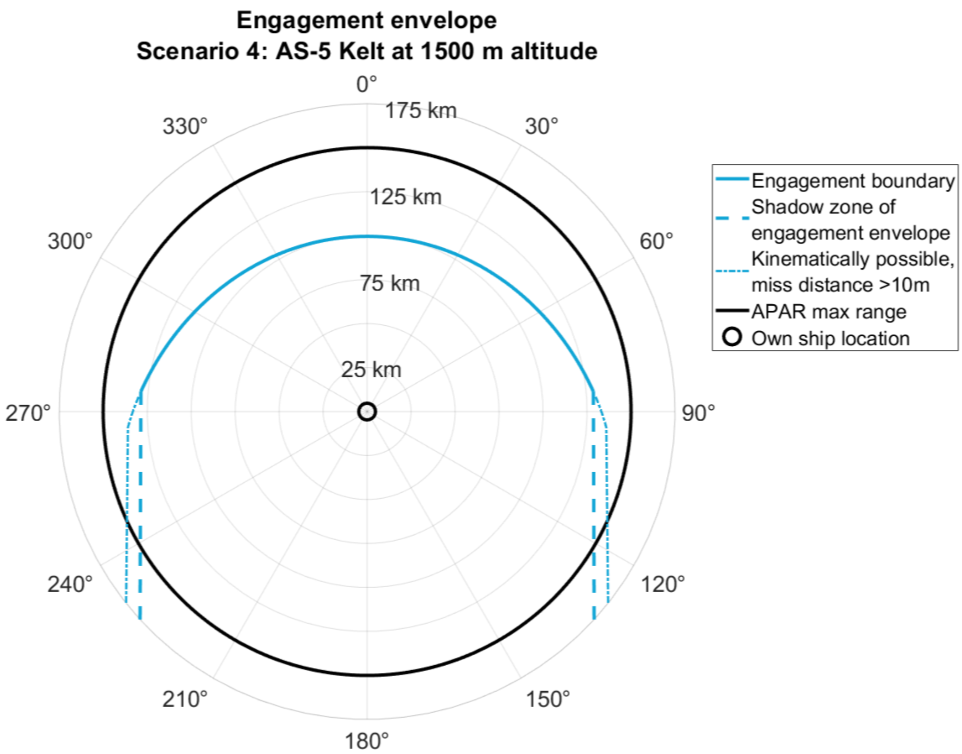

Figure 50: Engagement envelope for threat engagement scenario 2: AS-5 Kelt at a cruise altitude of 1500m and a cruise speed of 347 m/s. Threats come in from the top of the figure and fly downward. Once the threat passes the radar horizon, it is immediately tracked and engaged with no delay.

4.2.5. Scenario 5: AS-5 Kelt at cruise altitude 10000m

Figure 51 presents the engagement envelope against the AS-5 Kelt flying at a cruise altitude of 10000 m. The maximum radar range is again limited to 150 km, the maximum effective range of the APAR. The KAP_LONG Kappa midcourse guidance mode is used to perform the interceptions. The engagement envelope is similar in shape to the engagement envelope against the AS-5 Kelt flying at 1500 m. This is explained due to the fact that between ground ranges of 100 km and 140 km, the time-to-intercept for KAP_LONG against targets at 10 km altitude is very similar to the time-to-intercept of KAP_LONG_75 against targets at 1500 m altitude.

In the head-on scenario, the AS-5 Kelt is intercepted at a ground range of 102.3 km after 137.5 seconds. The maximum bearings at which the crossing threat can be intercepted are 76° and 284°. In these scenarios, the threats are intercepted at the APAR's maximum effective range of 150 km at a bearing of 105.5° and 254.5°, respectively. The time-to-intercept for these scenario's is 227.8 seconds. Perpendicular to the direction of flight of the AS-5 Kelt, at bearings of 90° and 270°, the SM-2 is able to provide coverage out to 135.0 km.

Similar to the engagement envelope against the Al-Mandab 2, the Standard Missile-2 Block IIIA is able to defend any friendly asset placed behind the launching ship. The SM-2 can defend friendly assets up to a range of 100 km in the direction of the threat vector, but any friendly asset beyond a range of 27.5 km cannot be defended in the case of an strike by an Al-Mandab 2.

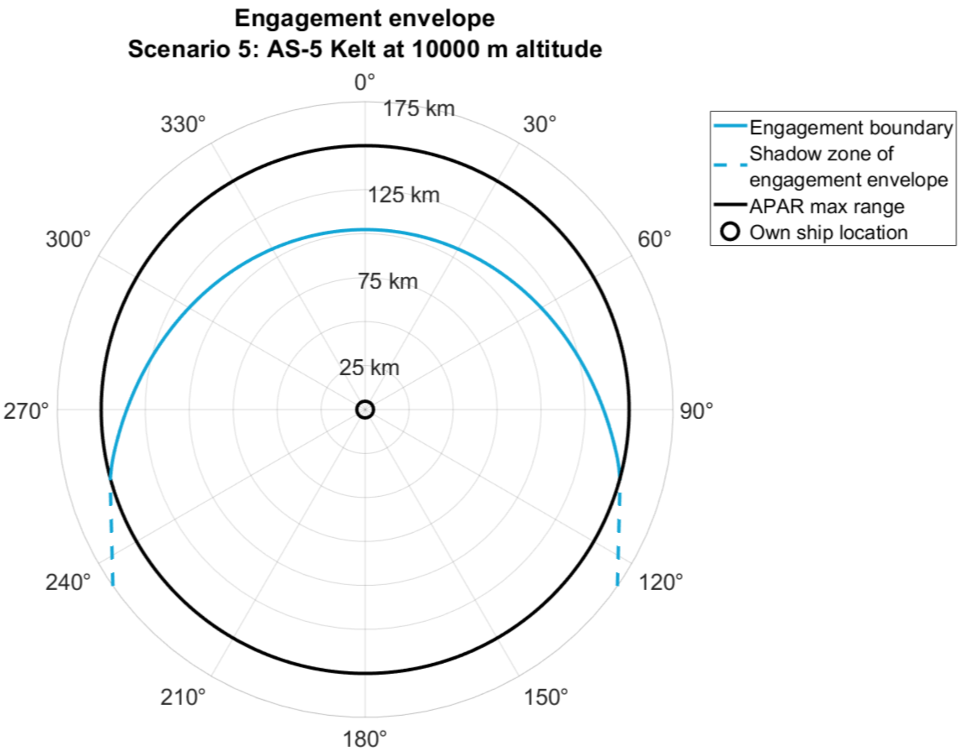

Figure 51: Engagement envelope for threat engagement scenario 2: AS-5 Kelt at a cruise altitude of 10000m and a cruise speed of 347 m/s. Threats come in from the top of the figure and fly downward. Once the threat passes the radar horizon, it is immediately tracked and engaged with no delay.

5. Conclusions

This thesis investigates the kinematic performance of the Standard Missile-2 and analyses its area-defence capabilities against drones and Anti-Ship Cruise Missiles. A modified point mass Simulink model was developed to simulate the SM-2 intercepting targets using the mathematical theory and interceptor information presented in this thesis. To answer the research questions, flyout tables and engagement envelopes were constructed.

Flyout tables were constructed for multiple Kappa midcourse guidance modes, including a modified version that allows the Standard Missile-2 Block IIIA to fly out to very long ranges. The Standard Missile-2 is found to have a maximum local burn-out Mach number of 4.4, translating to a sea-level adjusted Mach number of 3.8. Using standard Kappa midcourse guidance, the SM-2 Block IIIA has a maximum range of 83 kilometers against ground targets. Using the long-range Kappa guidance mode, the SM-2 is found to have a maximum ground range of 173 km, agreeing closely with the publicly reported maximum range of 167 km. The SM-2's maximum range reduces to 152 km at an altitude of 10 km and 130 km at an altitude of 20 km. Depending on the Kappa midcourse guidance mode, the SM-2 has a maximum effective service ceiling of 20-25 km. For normal Kappa guidance, the maximum service ceiling decreases with downrange distance, as the interceptor loses energy and the ability to manoeuvre during its flight. The maximum service ceiling of the long-range variant is not sensitive to downrange distance, due to the shaping of the flyout trajectories, resulting in very little energy loss at higher altitudes. For Kappa guidance with a specified target interception ground angle of -75 degrees, the service ceiling is reduced to 10-15 km.

Engagement envelopes were developed to simulate interceptions against crossing threats to analyse the SM-2's area-defence capabilities. Engagement envelopes were developed against the Houthi Samad-2 drone and Al-Mandab 2 Anti-Ship Cruise Missile, as well as against the Soviet-made AS-5 Kelt to simulate engagements against threats flying at a (very) high cruise altitude. The SM-2 is able engage and intercept the very slow flying Samad-2 very close to the target's radar horizon in any direction. The Al-Mandab 2, a high-subsonic Anti-Ship Cruise Missile, is intercepted at a range of 27.5 km in a head-on engagement simulation, leaving the launching ship with only one additional opportunity to re-engage the threat in case of a miss. The SM-2 can intercept the Al-Mandab 2 up to an initial target bearing of plus minus 71 degrees with respect to the head-on scenario direction, providing protection to friendly assets positioned behind the launching ship. Perpendicular to the Al-Mandab 2's flight direction, the SM-2 is able to protect assets up to a range of 36.1 km. Against the AS-5 Kelt, the SM-2 is able to provide extensive area-defence coverage. In a head-on engagement scenario, the SM-2 intercepts the AS-5 Kelt flying at cruise altitudes of 1500 m and 10000 m at ranges of 99.6 km and 102.3 km, respectively. Perpendicular to the direction of flight of the AS-5 Kelt, the SM-2 provides protection up to 128.0 and 135.0 km at the two flight altitudes. The SM-2 is able to provide protection to any asset positioned behind the launching ship in the the AS-5 Kelt's flight direction.

5.1. Implications of results

The Standard Missile-2 Block IIIA is shown to have extensive point-defence and area-defence capabilities against endo-atmospheric threats. With its current generation of Air Defence and Command Frigates and medium-range Surface-to-Air Missiles, the Royal Netherlands Navy is equipped to protect its trade routes in the Red Sea and Gulf of Aden by escorting convoys of commercial ships. Houthi Anti-Ship Cruise Missiles are the biggest threat to shipping, as their sea-skimming abilities and high-subsonic speeds mean they can only be detected, tracked, and engaged at relatively close ranges. Additionally, they carry relatively large explosive payloads that can cripple civilian ships with a single successful hit. The SM-2 is shown to be kinematically very able to intercept this threat type and operators should not hesitate to deploy the SM-2 to intercept these threats. It is shown that the SM-2 poses a threat against highly manoeuvrable fighter jets and AWACS-type airplanes up to a range of 140-150 km, keeping airspace around the launching ship safe. Lastly, the SM-2 is, kinematically speaking, completely overpowered against the Samad-2. Shooting down a swarm of Samad-2's costing 50k (0.05M) each using Standard Missiles costing 3.0-3.5M each is economically not sustainable, even when comparing the collective economic size of NATO to that of Iran and its proxies. The slow flight speeds of the Samad-2 make it a perfect target to be engaged by a ship's on-board canon, Close-In Weapon System, or helicopter gun.

5.2. Future research

1. The next step in making a more detailed flyout model of the Standard Missile-2 is to develop a full 6 Degrees-Of-Freedom model. In this research, the kinematic equations were already prepared to accommodate a 6-DOF simulation model. It would be wise to switch out Missile DATCOM98 by more accurate software such as CFD simulations, as Missile DATCOM98 is only based on semi-empirical relations, resulting in not always the most accurate aerodynamic coefficients for the given flight conditions. In 6-DOF simulations, aerodynamic cross-coupling of the roll, pitch, and yaw channels becomes very apparent and should be modelled accurately, requiring better performing software than Missile DATCOM98.

2. The Simulink model is set up as a generic missile model, meaning any other interceptors can be simulated. Assessing the kinematic performance of any Surface-to-Air, Air-to-Air, or Air-to-Ground missile against any target is thus possible. Investigating the kinematic performance of the SM-2 against the Samad-2, Al-Mandab 2, and AS-5 Kelt is relatively limited, but the engagement performance database can be expanded quickly to many interceptors and many targets.

3. For future research into interceptor performance, it is important to accurately model the seeker and warhead dynamics. Upgrading the Simulink model to 6-DOF should include seeker and warhead dynamics.

4. The Standard Missile-2's ability to intercept (Short Range) Ballistic Missiles could be investigated. Though shown to be theoretically able to intercept ballistic missiles at short ranges in a point-defence scenario if the target trajectory is known perfectly, it is expected that the SM-2 does not have the aerodynamic control authority to make

course corrections at high altitudes, due to its small aerodynamic surfaces. To model the interception of ballistic missiles, the least upgrade to the Simulink model should be seeker noise dynamics to introduce uncertainties in the exact target position.

References

[1] Commander David Ewing RN and Commander Malcolm Fuller RN. IHS Jane's Weapons - Naval Edition. IHS Global Limited, 2017-2018.

[2] Tom Spencer Joshua Cheetham and Shruti Menon. Tracking Houthi attacks in the Red Sea. British Broadcasting Corporation (BBC), January 20, 2024. Accessed via: https://www.bbc.com/news/world-middle-east-68031732.

[3] Fabian Hinz. Houthi anti-ship missile systems: getting better all the time. International Institute for Strategic Studies (IISS), December 19, 2023. Accessed via: https://www.iiss.org/online-analysis/online-analysis/2023/12/global-implications-of-the-shipping-attacks-in-the-red-sea/.

[4] Fabian Hinz. Global implications of the shipping attacks in the Red Sea. International Institute for Strategic Studies (IISS), January 4, 2024. Accessed via: https://www.iiss.org/online-analysis/military-balance/2024/01/houthi-anti-ship-missile-systems-getting-better-all-the-time/.

[5] BBC. Who are the Houthis and why are they attacking Red Sea ships? British Broadcasting Corporation, 15 March 2024. Accessed via: https://www.bbc.com/news/world-middle-east-67614911.

[6] United States Central Command (USCENTCOM) Public Affairs. U.S. Dhow Interdictions. Tampa, Florida., Feb. 19, 2019. Accessed via: https://www.centcom.mil/MEDIA/NEWS-ARTICLES/News-Article-View/Article/2087998/us-dhow-interdictions/.

[7] Ian Williams and Shaan Shaikh. The Missile War in Yemen. 1616 Rhode Island Avenue, NW Washington, D.C. 20036: Center for Strategic & International Studies, June 2020.

[8] Commander David Ewing RN and Commander Malcolm Fuller RN. IHS Jane's weapons: Naval Edition. United Kingdom: IHS Global Limited, 2016-2017.

[9] United Stated Office of Naval Intelligence. The PLA Navy: New capabilities and missions for the 21st century. 4251 Suitland Road Washington DC 20395-521 1: United Stated Office of Naval Intelligence, 2015.

[10] Sam Lagore. USS Mason Fired 3 Missiles to Defend From Yemen Cruise Missiles Attack. United Stated Naval Institute, October 11, 2016. Accessed via: https://news.usni.org/2016/10/11/uss-mason-fired-3-missiles-to-defend-from-yemen-cruise-missiles-attack.

[11] Al Jazeera. Yemen: Houthis claim attack on UAE military vessel. Al Jazeera, October 2, 2016. Accessed via: https://www.aljazeera.com/news/2016/10/2/yemen-houthis-claim-attack-on-uae-military-vessel.

[12] Fabian Hinz. Little and large missile surprises in Sanaa and Tehran. International Institute for Strategic Studies, 17 October 2023. Accessed via: https://www.iiss.org/online-analysis/military-balance/2023/10/little-and-large-missile-surprises-in-sanaa-and-tehran/.

[13] The Islamic Republic News Agency. A deeper look into missiles supplied to IRGC by Iran's defense industries. IRNA - The Islamic Republic News Agency, 7 August 2023. Accessed via: https://en.irna.ir/news/85191553/A-deeper-look-into-missiles-supplied-to-IRGC-by-Iran-s-defense.

[14] Yusuf Çetiner. The Houthis in Yemen Unveil Their New Anti-Ship Missiles At "The Promise of the Hereafter" Military Parade. Accessed via: https://www.overtdefense.com/2022/09/07/the-houthis-in-yemen-unveil-their-new-anti-ship-missiles-at-the-promise-of-the-hereafter-military-parade/: Overt Defense, 7 September 2022.

[15] Alex Walters. HMS Diamond displays kill markings after shooting down nine Houthi drones in Red Sea. Forces.net, February 12, 2024. Accessed via: https://www.forces.net/services/navy/hms-diamond-displays-drone-kill-markings-gibraltar-return.

[16] Armée française - Opérations militaires. EUNAVFOR ASPIDES EU| Interception par l'hélicoptère de la frégate FR d'un drone aérien en provenance du Yémen menaçant le trafic maritime civil en mer Rouge. Armée française - Opérations militaires, 20 March 2024. Accessed via:
https://twitter.com/EtatMajorFR/status/1770479631545532591.

[17] EUNAVFOR ASPIDES. On March 20, while conducting close protection under @EUNAVFORASPIDES in Red Sea, the embarked helicopter of a French destroyer shot down a Houthi UAV threatening the commercial navigation. @hndgspio @MarineNationale @FFEAU_ALINDIEN @EtatMajorFR shieldingfreedomofnavigation. EUNAVFOR ASPIDES, 20 March 2024. Accessed via: https://twitter.com/EtatMajorFR/status/1770479631545532591.

[18] USCENTCOM. Statement: US CENTCOM Statement on 27th Houthi attack on commercial shipping lanes in the Gulf of Aden. United States Central Command, 11 Jan 2024. Accessed via: https://www.centcom.mil/MEDIA/STATEMENTS/Statements-View/\Article/3643121/us-centcom-statement-on-27th-houthi-attack-on-commercial-shipping-lanes-in-the/.

[19] Dr. Carlo Kopp. Soviet/Russian Cruise Missiles: Technical Report APA-TR-2009-0805. Air Power Australia, 2008-2012. Accessed via: https://www.youtube.com/shorts/L4yvE4IsiXA.

[20] Clifton E. Cole Jr. Missile Communication Links. John Hopkins APL Technical Digest, Volume 28, Number 4, 2010.

[21] Robert W. Witte and Robert L. Mc Donald. Standard Missile: Guidance System Development. John Hopkins APL Technical Digest, Volume 2, Number 4, 1981.

[22] Uttam K. Sahu et al. Modified Generalized Explicit Guidance for Midcourse with Near-Zero Lateral Acceleration in Terminal Phase. Cape Town, South Africa: International Federation of Automatic Control, 2014.

[23] Ross A. Blauwkamp Neil F. Palumbo and Justin M. Lloyd. Modern Homing Missile Guidance Theory and Techniques. John Hopkins APL Technical Digest, Volume 29, Number 1, 2010.

[24] Warren J. Boord and John B. Hoffman. Air and Missile Defense Systems Engineering. Boca Raton: CRC Press, Taylor & Francis Group, 2016.

[25] AIAA/ANSI. Recommended Practice for Atmospheric and Space Flight Vehicle Coordinate Systems. 370 L'Enfant Promenade, SW, Washington: AIAA, 1992.

[26] Lieutenant commander Robert D. Broadston. A method of increasing the kinematic boundary of air-to-air missiles using an optimal control approach. Monterey, California: Naval Postgraduate School, 2000.

[27] Marc Naeije and Erwin Mooij. AE3212-I Flight Dynamics, lectures 08: 'Frames and Transformations' and 09: 'Dynamic Transformations and Equations of Motion'. Delft: Delft University of Technology, 2021-2022.

[28] George M. Siouris. Missile Guidance and Control Systems. First Edition. New York: Springer Science + Business Media, March 9, 2004.

[29] Leopoldo Armesto. Robotic Systems: Quaternions. Valencia: Universitat Politecnica de Valencia, 2021.

[30] Ching-Fan Lin. Modern Navigation, Guidance, And Control Processing. Upper Saddle River, NJ: Prentice-Hall, 1991.

[31] E.J. Ohlmeyer and C.A. Phillips. Generalized vector explicit guidance. Journal of Guidance, Control, and Dynamics, 2006.

[32] Paul Zarchan. Tactical and Strategic Missile Guidance. Sixth Edition. 12700 Sunrise Valley Drive, Suite 200: American Institute of Aeronautics and Astronautics, 2012.

[33] D. Serakos and C.F. Lin. Linearized kappa guidance. Journal of Guidance, Control, and Dynamics, 1995.

[34] John A. Lukacs IV and Oleg A. Yakimenko. Trajectory-Shape-Varying Missile Guidance for Interception of Ballistic Missiles during the Boost phase. American Institute of Aeronautics and Astronautics, 2007.

[35] Commander Malcolm Fuller RN. Jane's Naval Weapon Systems, Issue 54. Sentinel House, 163 Brighton Road, Coulsdon, Surrey, CR5 2YH, UK: IHS Global Limited, 2011.

[36] P. Zipfel. Modeling and Simulation of Aerospace Vehicle Dynamics. Reston, VA: American Institute of Aeronautics and Astronautics, 2000.

[37] Missile Defense Project. Standard Missile-2 Block II/III. Center for Strategic and International Studies, April 14, 2016, last modified June 24, 2021. Accessed via `https://missilethreat.csis.org/defsys/sm-2`.

[38] M.E. Brown and P.T. Herman. Model of SM-2 (ER) [Unclassified]. Livermore, California: Lawrence Livermore Laboratory, University of California, October 14, 1974.

[39] Junwei Lei Jian Shen Heng Li and Jing Li. Parameter Estimation and Analysis of Standard-2 Missile. 5th International Workshop on Materials Engineering and Computer Sciences (IWMECS), 2020.

[40] Matthew Montoya. Standard Missile: A Cornerstone of Navy Theater Air Missile Defense. John Hopkins APL Technical Digest, Volume 22, Number 3, 2001.

[41] G.D. Goldshine and G.T. Lacy. High-Response Electromechanical Control Actuator. Pamona, California: General Dynamics Corporation, 1 October 1968.

[42] Jeffrey Strickland. Missile Flight Simulation. Second Edition. 3101 Hillsborough Street, Raleigh, NC 27607: Lulu press, 2015.

[43] Thomas Dekkers Mark Voskuijl and Ralph Savelsberg. Flight Performance Analysis of the Samad Attack Drones Operated by Houthi Armed Forces. Science & Global Security, 2020.

[44] Martin Streetly. Jane's Radar and Electronic Warfare Systems. 2007-2008.

[45] Merrill I. Skolnik. Introduction to radar systems. Third edition. 1221 Avenue of the Americas, New York, NY, 10020: McGraw-Hill Book Co, 2001.

[46] S. Mondal and R. Padhi. Generalized explicit guidance with optimal time-to-go and realistic final velocity. Proceedings of the Institution of Mechanical Engineers Part G Journal of Aerospace Engineering, 2019.

[47] Damen Shipyards Group. Damen Schelde Naval Shipbuilding - Air Defence and Command Frigate (LCF) product sheet. Accessed via: `https://www.damen.com/vessels/defence-and-security/custom-built-combatants/air-defence-and-command-frigates#download`: Damen Shipyards Group.

[48] Damen Shipyards Group. Air Defence and Command Frigates. Accessed via: `https://www.damen.com/vessels/defence-and-security/custom-built-combatants/air-defence-and-command-frigates#specifications`: Damen Shipyards Group.

A. Appendix

A.1. T_{go} approximation

In this section, the time-to-go (T_{go}) is approximated. It should be noted that no open-source information detailing the exact midcourse guidance algorithm used by the SM-2 Block IIIA is available. Similarly, there is no open-source information available on how the SM-2's on-board software estimates the T_{go}. Therefore, the methodology of calculating the midcourse guidance acceleration commands and T_{go} (and V_{MF}) are based on methodologies found in open literature, without providing a guarantee that the adopted methodologies accurately describe the actual guidance software on board the SM-2 Block IIIA.

T_{go} can be approximated using an equation as simple as $T_{go} = R_{MPCP}/V_M$ [24], or can be approached using various approximation methods. In this section, a more advanced method of calculating T_{go} is presented based on the work by Mondal and Padhi [46]. Here, only the final and necessary derivations resulting in the set of equations to calculate T_{go} are presented. The more fundamental derivations are omitted, as they can be reviewed in-depth in Mondal and Padhi's paper.

To start, Equation 9 presents the acceleration commands in the LCIC frame. Mondal and Padhi's approximation of the time-to-go, T_{go}, is a function of the current and specified velocity vector. Therefore, T_{go} is derived based on information on the interceptor's velocity vector, rather than the orientation of interceptor's body frame. To project the acceleration commands in the LCIC frame derived in Equation 9 into the velocity frame, two rotations are applied. First, a rotation consisting of the vertical flight path angle γ_v is performed. Then, a rotation consisting of the heading angle ψ_h is applied [46]. The acceleration commands in MBCF as a function of the acceleration commands in LCIC and flight path- and heading angles are given by Equation 61 [46]:

$$\begin{bmatrix} a_x^{MBC} \\ a_y^{MBC} \\ a_z^{MBC} \end{bmatrix} = \begin{bmatrix} c(\gamma_v)c(\psi_h) & -c(\gamma_v)s(\psi_h) & -s(\gamma_v) \\ s(\psi_h) & c(\psi_h) & 0 \\ s(\gamma_v)c(\psi_h) & -s(\gamma_v)s(\psi_h) & c(\gamma_v) \end{bmatrix} \cdot \begin{bmatrix} a_x^{LCIC} \\ a_y^{LCIC} \\ a_z^{LCIC} \end{bmatrix} \tag{61}$$

where a_x^{MBC}, a_y^{MBC}, and a_z^{MBC} are the acceleration commands in the MBC frame, γ_v is the vertical flight path angle, ψ_h is the heading angle, and a_x^{LCIC}, a_y^{LCIC}, and a_z^{LCIC} are the acceleration commands in the LCIC frame.

Since the solid propellant rocket motor has a fixed thrust profile in time, acceleration commands in the MBCF x-direction cannot be performed. Therefore, the first row in Equation 61 is ignored. We thus define the acceleration commands in y- and z-directions and the LCIC-to-MBCF rotation matrix in y- and z-direction as (Equation 62 and Equation 63) [46]:

$$a^{MBC} = \begin{bmatrix} a_y^{MBC} \\ a_z^{MBC} \end{bmatrix} \tag{62}$$

$$[p] = \begin{bmatrix} s(\psi_h) & c(\psi_h) & 0 \\ s(\gamma_v)c(\psi_h) & -s(\gamma_v)s(\psi_h) & c(\gamma_v) \end{bmatrix} \tag{63}$$

The flight path angle γ_v and heading angle ψ_h are now replaced by their average value during the whole flight, namely $\bar{\gamma_v} = (\gamma_v + \gamma_{v,d})/2$ and $\bar{\psi_h} = (\psi_h + \psi_{h,d})/2$, where $\gamma_{v,d}$ and $\psi_{h,d}$ are the specified desired interception vertical ground angle and heading angle, respectively [46]. The average rotation matrix $\bar{p}$ is now given by Equation 64 [46]:

$$[\bar{p}] = \begin{bmatrix} s(\bar{\psi_h}) & c(\bar{\psi_h}) & 0 \\ s(\bar{\gamma_v})c(\bar{\psi_h}) & -s(\bar{\gamma_v})s(\bar{\psi_h}) & c(\bar{\gamma_v}) \end{bmatrix} \tag{64}$$

The matrices S and $\bar{S}$ are now defined as a function of the rotation matrices p and $\bar{p}$. Equation 65 and Equation 66 present S and $\bar{S}$ as functions of p and $\bar{p}$ [46]:

$$S = p^T p \tag{65}$$

$$\bar{S} = \bar{p}^T \bar{p} \tag{66}$$

The performance index J is now defined using Equation 67 [46]:

$$J = \int_{T_{go}}^{0} \frac{(a^{MBC})^T (a^{MBC})}{2T_{go}^n} dT_{go} \tag{67}$$

where n is the trajectory shaping gain. Increasing n results in a larger T_{go} in Equation 73, which in turn increases the relative weight of the second term in Equation 9.

Integrating the performance index J with respect to T_{go} results in (Equation 68) [46]:

$$J_{opt} = -\frac{1}{2}\left[\mathbf{P}^T \bar{S}\mathbf{P}\frac{T_{go}^{(n+1)}}{(n+1)} + 2\mathbf{P}^T \bar{S}\mathbf{Q}\frac{T_{go}^{(n+2)}}{(n+2)} + \mathbf{Q}^T \bar{S}\mathbf{Q}\frac{T_{go}^{(n+3)}}{(n+3)}\right] \tag{68}$$

where (Equation 69 and Equation 70) [46]:

$$\mathbf{P} = (n+1)\cdot\mathbf{C}_1 \tag{69}$$

$$\mathbf{Q} = (n+2)\cdot\mathbf{C}_2 \tag{70}$$

with (Equation 71 and Equation 72) [46]:

$$\mathbf{C}_1 = -\frac{n+2}{T_{go}^{(n+2)}}\left[(n+3)\mathbf{R}_{MPCP} - (\mathbf{V}_M + (n+2)\mathbf{V}_{MF})T_{go}\right] \tag{71}$$

$$\mathbf{C}_2 = \frac{n+3}{T_{go}^{(n+3)}}\left[(n+2)\mathbf{R}_{MPCP} - (\mathbf{V}_M + (n+1)\mathbf{V}_{MF})T_{go}\right] \tag{72}$$

After much rewriting, Equation 68 becomes Equation 73 [46]:

$$J_{opt} = -\frac{1}{2}\left[AT_{go}^{-(n+3)} + BT_{go}^{-(n+2)} + CT_{go}^{-(n+1)}\right] \tag{73}$$

where (Equation 74 to Equation 76) [46]:

$$\begin{aligned} A = (n+1)(n+2)^2\mathbf{l}_1^T\bar{S}\mathbf{l}_1 - 2(n+1)(n+2)(n+3)\mathbf{l}_1^T\bar{S}\mathbf{l}_2 + \\ (n+3)(n+2)^2\mathbf{l}_2^T\bar{S}\mathbf{l}_2 \end{aligned} \tag{74}$$

$$\begin{aligned} B = 2(n+1)(n+2)^2\mathbf{l}_1^T\bar{S}\mathbf{m}_1 - 2(n+1)(n+2)(n+3) \\ (\mathbf{l}_1^T\bar{S}\mathbf{m}_2 + \mathbf{m}_1^T\bar{S}\mathbf{l}_2) + 2(n+3)(n+2)^2\mathbf{l}_2^T\bar{S}\mathbf{m}_2 \end{aligned} \tag{75}$$

$$\begin{aligned} C = (n+1)(n+2)^2\mathbf{m}_1^T\bar{S}\mathbf{m}_1 - 2(n+1)(n+2)(n+3) \\ \mathbf{m}_1^T\bar{S}\mathbf{m}_2 + (n+3)(n+2)^2\mathbf{m}_2^T\bar{S}\mathbf{m}_2 \end{aligned} \tag{76}$$

in which (Equation 77 to Equation 80) [46]:

$$\mathbf{l}_1 = (n+3)\cdot\mathbf{R}_{MPCP} \tag{77}$$

$$\mathbf{l}_2 = (n+2)\cdot\mathbf{R}_{MPCP} \tag{78}$$

$$\mathbf{m}_1 = -(\mathbf{V}_M + (n+2)\mathbf{V}_{MF}) \tag{79}$$

$$\mathbf{m}_2 = -(\mathbf{V}_M + (n+1)\mathbf{V}_{MF}) \tag{80}$$

In Equation 73, J_{opt} is now a function of the T_{go} and the time-varying variables A, B, and C. By differentiating Equation 73 with respect to T_{go} as described in Equation 81, the extremum can be found [46]:

$$\frac{dJ_{opt}}{dT_{go}} = -\frac{1}{2}\left[C(-n-1)\,T_{go}^{-(n+2)} + B(-n-2)\,T_{go}^{-(n+3)} + A(-n-3)\,T_{go}^{-(n+4)}\right] \tag{81}$$

Multiplying both sides of Equation 81 by $T_{go}^{(n+4)}$ results in Equation 82 [46]:

$$(n+1)C\cdot T_{go}^2 + (n+2)B\cdot T_{go} + (n+3)A = 0, \tag{82}$$

which, finally, is rewritten to find T_{go} by applying the quadratic equation in Equation 83:

$$T_{go} = \frac{-(n+2)B \pm \sqrt{(n+2)^2B^2 - 4(n+1)(n+3)AC}}{2C(n+1)} \tag{83}$$

Equation 83 results in two real and positive results for T_{go} [46]. Mondal and Padhi show that the expression with the 'minus' sign always results in the correct value for T_{go} [46].

A.2. V_{MF} approximation

To approximate the predicted interceptor velocity at the PCP, V_{MF}, one can simply assume $V_{MF} = V_M$, similar to the simple calculation of $T_{go} = R_{MPCP}/V_M$. However, a more advanced methodology to calculate V_{MF} is presented here based on the methodology of Mondal and Padhi [46]. For the full derivation of V_{MF}, the reader is referred to Mondal and Padhi's work [46].

Equation 84 presents Mondal and Padhi's equation to calculate V_{MF} [46].

$$V_{MF} = \frac{V_M}{1 + \left(\frac{1}{2}\bar{\rho} C_D S_{Ref}\right) V_M T_{go}} \tag{84}$$

where $\bar{\rho}$ is the average air density of the missile's current altitude and at the PCP, $\bar{\rho} = (\rho + \rho_{PCP})/2$.

The predicted missile velocity vector at the PCP, $\mathbf{V}_{MF}$ in Equation 9, is the product of the specified missile velocity unit vector at the PCP, $\mathbf{i}_{MF}$ and V_{MF}, where $\mathbf{i}_{MF}$ is found through the specified interception vertical flight path angle $\gamma_{v,d}$ and heading angle $\psi_{h,d}$.

A.3. Six Degrees of Freedom Equations of Motion

In six Degrees of Freedom (6-DOF) simulations, the interceptor's Euler angles ϕ, θ, and ψ that orient the MBC frame with respect to the LCIC frame are explicitly modeled. They are no longer constructed with respect to the velocity vector, as is the case for modified point mass simulations. The interceptor now has both an explicit position and orientation inside the LCIC frame. The forces and moments acting on the interceptor inside the now non-inertial (rotating) MBC frame result in translational and rotational accelerations along and about the interceptor's body axes. To calculate both the translational and rotational accelerations in the MBC frame, the angular rates of the MBC frame itself must be taken into account. The resulting translational accelerations in the MBC frame can be directly translated to accelerations in the LCIC frame by applying the quaternion transformation matrix found in Equation 8. The rotational accelerations are first integrated in time to find the angular rates, p, q, and r, which are used to find the angular rates of the Euler angles.

To start, the angular rate vector $\boldsymbol{\omega}^b$ describes the rotational velocities about the interceptor's body axes and is expressed as [28]:

$$\boldsymbol{\omega}^b = p\mathbf{i} + q\mathbf{j} + r\mathbf{k} = \begin{bmatrix} p \\ q \\ r \end{bmatrix}_b, \tag{85}$$

where p, q, and r are the angular rates about the missile's X_b, Y_b, and Z_b axes, respectively. The missile's roll rate is p, q is the pitch rate, and r is the yaw rate.

A.3.1. Translational accelerations in the Missile Body Coordinate frame

The translational accelerations in the rotating MBC frame are calculated by taking the instantaneous forces acting on the interceptor at timestep t as if the MBC frame were an inertial frame, minus the cross product of the angular velocities about, and linear velocities along, the body axes. The acceleration that the interceptor experiences with respect to the rotating MBC frame is thus described by [28] [42]:

$$\dot{\mathbf{V}}^b = \frac{\mathbf{F}^b}{m} - (\boldsymbol{\omega}^b \times \mathbf{V}^b) = \begin{bmatrix} \dot{u} \\ \dot{v} \\ \dot{w} \end{bmatrix}_b, \tag{86}$$

where $\mathbf{F}^b$ is the force vector in the MBC frame frame, $\boldsymbol{\omega}_b$ is the angular rate vector about the X_b, Y_b, and Z_b axes, and $\mathbf{V}^b$ is the velocity vector describing the velocities u, v, and w along the body axes.

The cross product $(\boldsymbol{\omega} \times \mathbf{V})$ is:

$$(\boldsymbol{\omega} \times \mathbf{V}) = \begin{bmatrix} \mathbf{i} & \mathbf{j} & \mathbf{k} \\ p & q & r \\ u & v & w \end{bmatrix} = (wq - vr)\mathbf{i} + (ur - wp)\mathbf{j} + (vp - uq)\mathbf{k}. \tag{87}$$

Rewriting Equation 86 and dividing it into its individual components, the interceptor's accelerations along the X_b, Y_b, and Z_b axes are thus defined as [42]:

$$\dot{u} = \frac{F_x^b}{m} - (wq - vr), \tag{88}$$

$$\dot{v} = \frac{F_y^b}{m} - (ur - wp), \tag{89}$$

and

$$\dot{w} = \frac{F_z^b}{m} - (vp - uq), \tag{90}$$

where $\dot{u}$, $\dot{v}$ and $\dot{w}$ are the components of the translational acceleration along the X_b, Y_b, and Z_b axes of the MBC frame; F_x^b, F_y^b, and F_z^b are the total forces acting on the missile along the X_b, Y_b, and Z_b axes; u, v, and w are the missile's velocities in the MBC frame, and p, q, and r are the missile's angular rates about the X_b, Y_b, and Z_b axes [42].

A.3.2. Rotational accelerations in the Missile Body Coordinate Frame

The time rate of change of a missile's angular momentum in an inertial reference frame is equal to the moment acting upon the missile, or:

$$\frac{d}{dt}\mathbf{h} = \mathbf{M}, \tag{91}$$

where the particle's angular momentum vector $\mathbf{h}$ is given by [42]:

$$\mathbf{h} = [\,\mathbf{I}\,]\boldsymbol{\omega} = [\,\mathbf{I}\,](p\mathbf{i} + q\mathbf{j} + r\mathbf{k}) = [\,\mathbf{I}\,] \cdot \begin{bmatrix} p \\ q \\ r \end{bmatrix}, \tag{92}$$

in which $[\,\mathbf{I}\,]$ is the particle's inertia matrix and $\boldsymbol{\omega}$ is the angular velocity vector about the particle's x-, y- and z- axes. The inertia matrix $[\,\mathbf{I}\,]$ is given by [42]:

$$[\,\mathbf{I}\,] = \begin{bmatrix} I_{xx} & -I_{xy} & -I_{xz} \\ -I_{xy} & I_{yy} & -I_{yz} \\ -I_{xz} & -I_{yz} & I_{zz} \end{bmatrix}, \tag{93}$$

where I_x, I_y, and I_z are the moments of inertia about the interceptor's x-, y- and z- axes and I_{xy}, I_{xz}, and I_{yz} are products of inertia [42]. Strickland stipulates that "a particular orientation of the reference frame axes relative to the body can always be chosen for which the products-of-inertia terms vanish", resulting in a simplified inertia matrix $[\,\mathbf{I}\,]$, where $[\,\mathbf{I}\,]$ is now expressed using [42]:

$$[\mathbf{I}] = \begin{bmatrix} I_x & 0 & 0 \\ 0 & I_y & 0 \\ 0 & 0 & I_z \end{bmatrix}. \tag{94}$$

For axisymmetric missiles, the missile body axes align with the principle axes for which it holds that $I_{xy} = I_{xz} = I_{yz} = 0$ [42]. The Standard Missile-2 is not quite axisymmetric since it has two sets of four fins. However, these fins are located in the same planes as the MBC frame's Y- and Z-axes. The products of inertia can thus be assumed to be zero. Furthermore, the fins have a very small mass compared to the main body. The products of inertia can thus be assumed to be zero even if the fins were positioned using an X-configuration, rather than the SM-2's cross-configuration. We also assume that, similar to the missile's mass m, the inertia tensor $[\,\mathbf{I}\,]$ may be assumed to be constant or be given an instantaneous value at timestep t. Therefore, time rate of change of the angular momentum of an axisymmetric missile in an inertial reference frame can be expressed by [42]:

$$\frac{d}{dt}\mathbf{h} = \frac{d}{dt}([\,\mathbf{I}\,]\boldsymbol{\omega}) = [\,\mathbf{I}\,]\dot{\boldsymbol{\omega}} = \begin{bmatrix} I_x & 0 & 0 \\ 0 & I_y & 0 \\ 0 & 0 & I_z \end{bmatrix} \cdot \begin{bmatrix} \dot{p} \\ \dot{q} \\ \dot{r} \end{bmatrix} = \mathbf{M} = \begin{bmatrix} L \\ M \\ N \end{bmatrix}, \tag{95}$$

resulting in the angular acceleration equations about the interceptor's x-, y-, and z- axes in the inertial reference frame:

$$\dot{p} = \frac{L}{I_x}, \tag{96}$$

$$\dot{q} = \frac{M}{I_y}, \tag{97}$$

and

$$\dot{r} = \frac{N}{I_z}. \tag{98}$$

In a rotating frame, as is the case for the MBC frame in 6-DOF simulations, the angular rate accelerations $\dot{p}$, $\dot{q}$, and $\dot{r}$ are found in a similar method to the procedure of deriving the translational accelerations in the rotating MBC frame. By subtracting the cross product of the angular rate vector and local velocity vector, $\left(\boldsymbol{\omega}^b \times \mathbf{V}^b\right)$, from the moment vector $\mathbf{M}^b$ and subsequently dividing by the Inertia tensor, the angular accelerations about the body axes are found using [42] :

$$\dot{\boldsymbol{\omega}}^b = \frac{\mathbf{M}^b - \left(\boldsymbol{\omega}^b \times \mathbf{V}^b\right)}{[\,\mathbf{I}\,]} = \begin{bmatrix} \dot{p} \\ \dot{q} \\ \dot{r} \end{bmatrix}_b , \tag{99}$$

where the definition of the cross product $\left(\boldsymbol{\omega}^b \times \mathbf{V}^b\right)$ is found in Equation 87. Finally, rewriting Equation 99 and expressing each individual component results in [42]:

$$\dot{p} = \frac{L - qr(I_z - I_y)}{I_x}, \tag{100}$$

$$\dot{q} = \frac{M - pr(I_x - I_z)}{I_y}, \tag{101}$$

and

$$\dot{r} = \frac{N - pq(I_y - I_x)}{I_z}, \tag{102}$$

where $\dot{p}$, $\dot{q}$ and $\dot{r}$ are the angular acceleration components about the X_b, Y_b and Z_b axes in the MBC frame frame, L, M and N are the total moment components about the X_b, Y_b, and Z_b axes, p, q and r are the components of the angular rate vector $\boldsymbol{\omega}$ and I_x, I_y, and I_z are the moments of inertia about the X_b, Y_b and Z_b axes.

A.3.3. Euler angle rates of change

Finally, the Euler angles that describe the interceptor's attitude with respect to the inertial reference frame can be derived. The equations describing the rates of change of the Euler angles are given by [42]:

$$\dot{\phi} = p + \left(qsin(\phi) + rcos(\phi)\right) tan(\theta), \tag{103}$$

$$\dot{\theta} = qcos(\phi) - rsin(\phi), \tag{104}$$

and

$$\dot{\psi} = \frac{\left(qsin(\phi) + rcos(\phi)\right)}{\cos(\theta)}. \tag{105}$$

The Euler angles ϕ, θ, and ψ can now be found by integrating the Euler angle rates.

A.4. Aerodynamic forces and moments in 6 Degrees of Freedom simulations

The moments acting about the SM-2's body axes are the result of aerodynamic moments, denoted as:

$$\mathbf{M}^b = \mathbf{M}_A^b, \tag{106}$$

where $\mathbf{M}_A^b$ is the aerodynamic moment vector acting about the missile's body axes. Represented by its individual components, $\mathbf{M}_A^b$ is defined as:

$$\mathbf{M}_A^b = L\mathbf{i} + M\mathbf{j} + N\mathbf{k} = \begin{bmatrix} L_A \\ M_A \\ N_A \end{bmatrix}_b, \tag{107}$$

where L_A, M_A and N_A are the aerodynamic moments acting about the interceptor's local X-, Y-, and Z-axes, respectively. The aerodynamic moments are the product of the moment coefficients, multiplied by the dynamic pressure, reference area, and interceptor diameter, denoted as:

$$\begin{bmatrix} L_A \\ M_A \\ N_A \end{bmatrix}_b = q_d \cdot S_{Ref} \cdot D \cdot \begin{bmatrix} C_{M_x} \\ C_{M_y} \\ C_{M_z} \end{bmatrix}_b. \tag{108}$$

A.5. Brown and Herman's detailed SM-2 Block I geometry diagrams

Brown and Herman's detailed geometric description of the Standard Missile-2 Block I is presented in Figure 52, Figure 53, and Figure 54 [38].

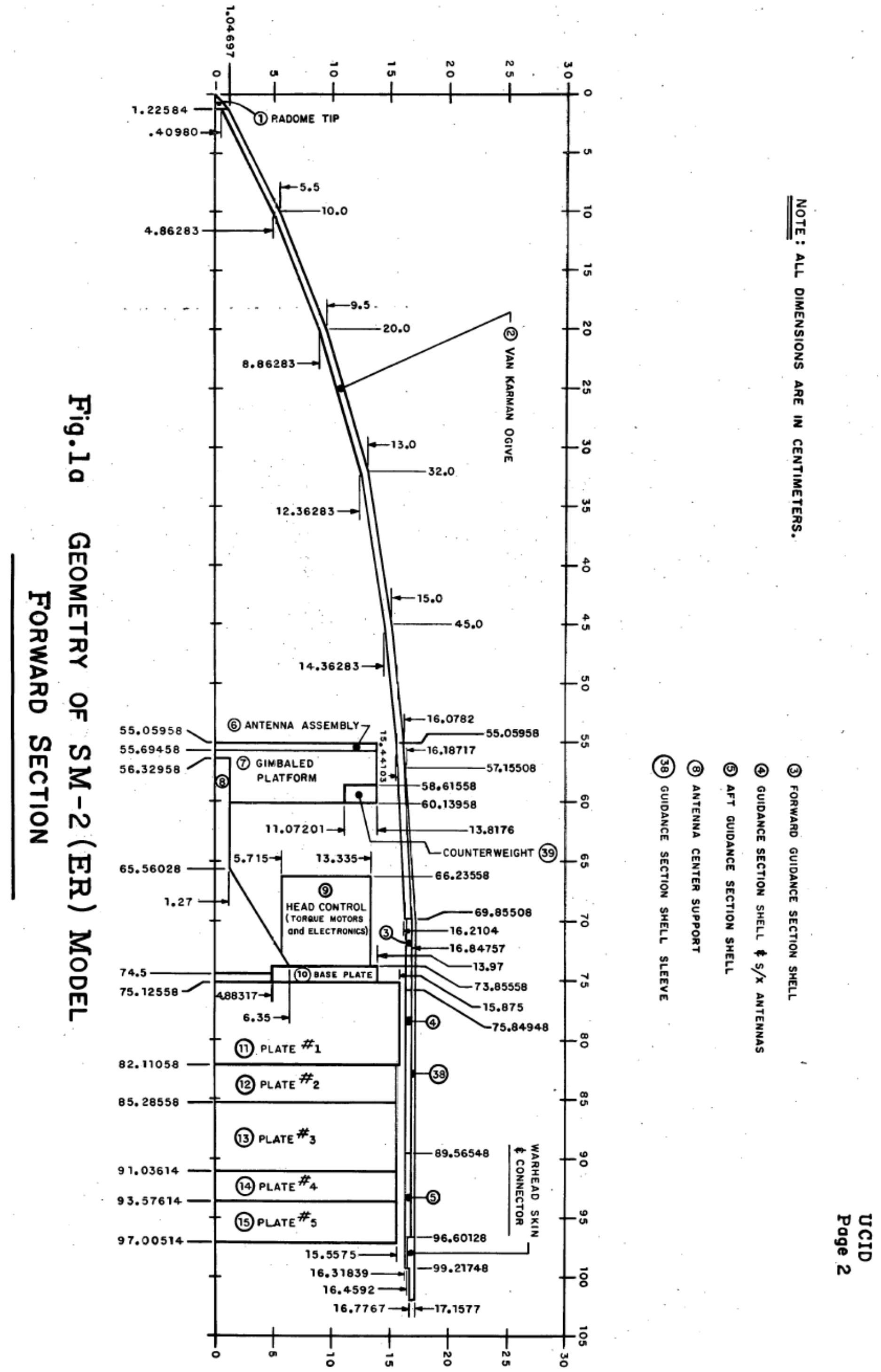

Figure 52: Front section of the Standard Missile-2 Block I according to Brown and Herman [38]

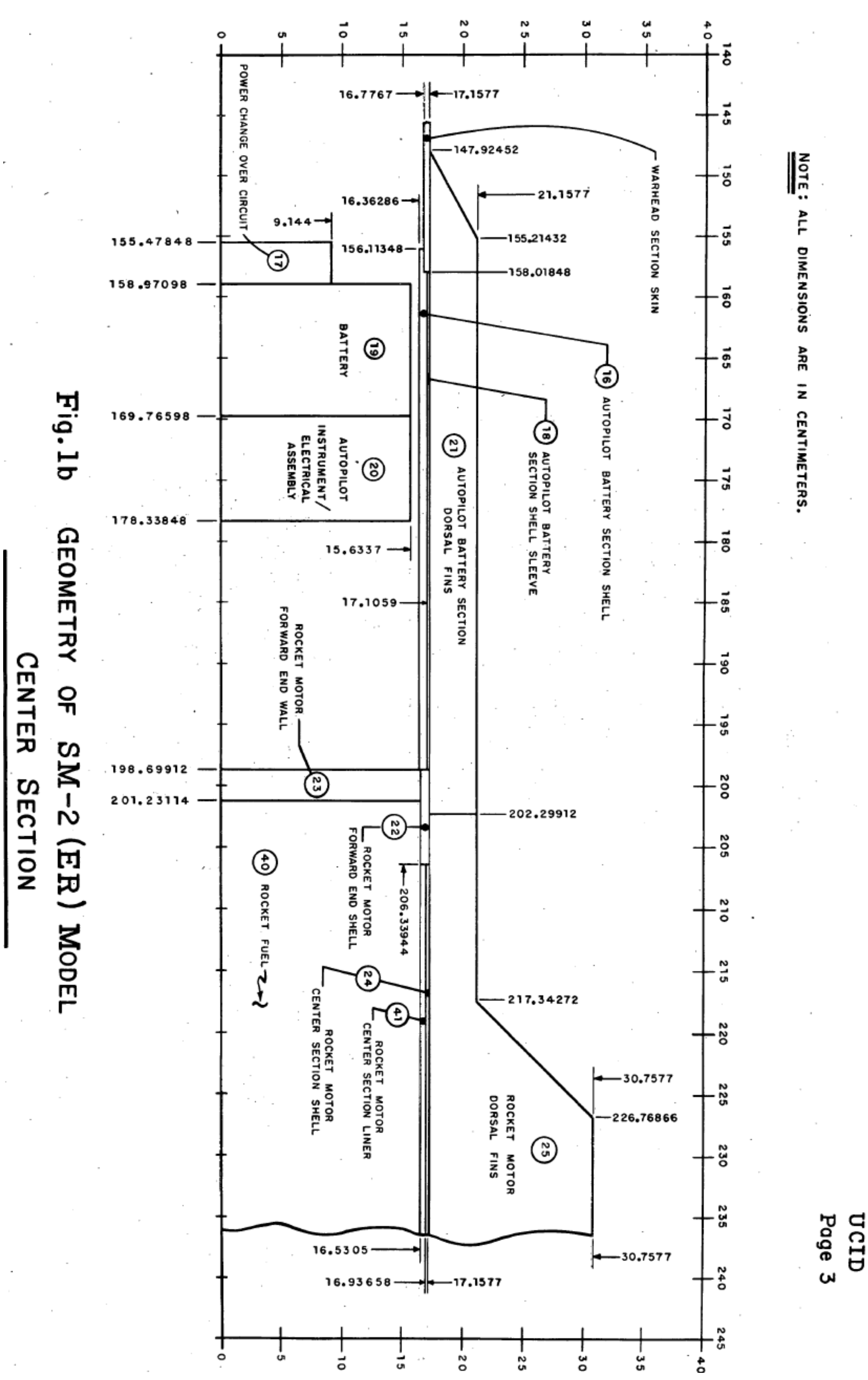

Figure 53: Center section of the Standard Missile-2 Block I according to Brown and Herman [38]

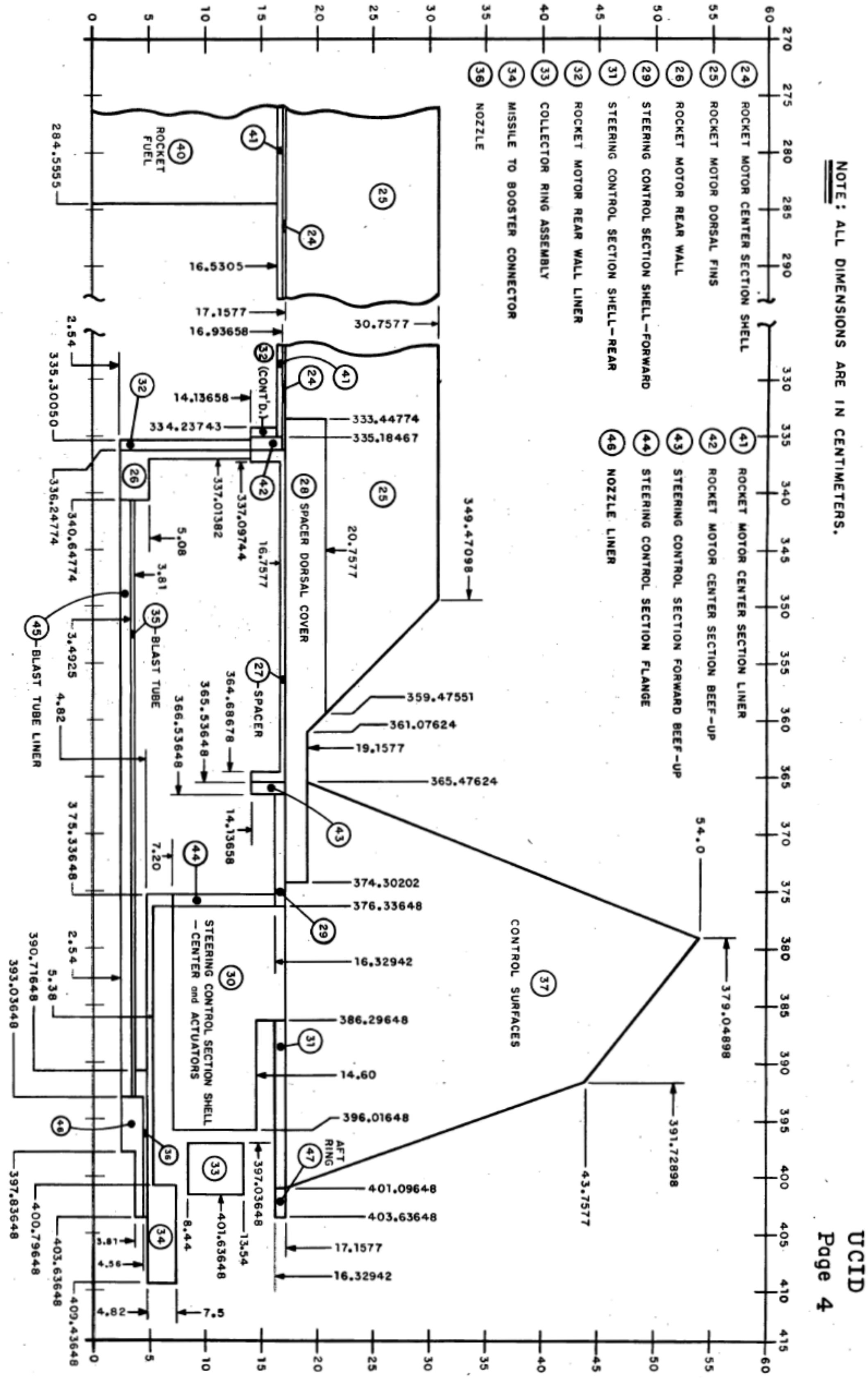

Figure 54: Rear section of the Standard Missile-2 Block I according to Brown and Herman [38]

A.6. Open-source photos of cross-section of SM-2 main wings

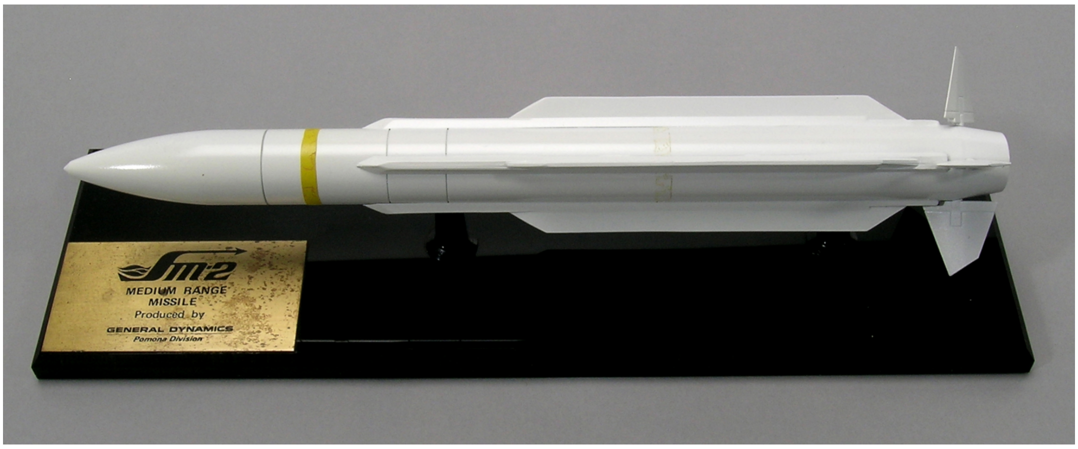

Figure 55: To-scale (scale unknown) model of the Standard Missile 2. Credit: Smithsonian National Air and Space Museum

Figure 56: Standard Missile-2 on a trainable launcher. Credit: Missile Defense Advocacy

A.7. APAR Height estimation

No open-source information could be found specifying the APAR's height. Therefore, the APAR's height is estimated using available photos found on the internet. Figure 57, a side-view of the LCF supplied by the ship's builder, Damen Shipyards Group, is used to approximate the height of the APAR. In Figure 57, the ship has a length of 1808 pixels long and an APAR height of 342 pixels. The LCF ships have a length of 144.2 meters [47]. The APAR is thus approximated at 27.25 meters above sea level.

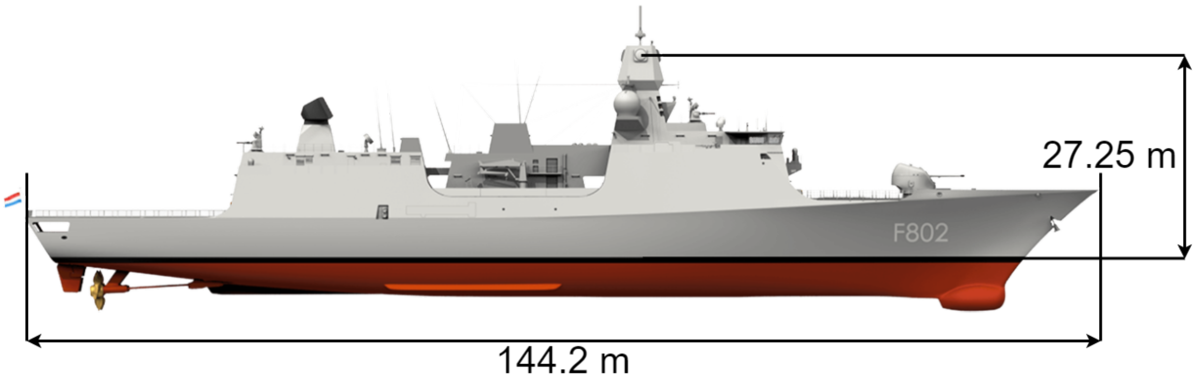

Figure 57: F802 "De Zeven Provinciën" - Royal Netherlands Navy Air Defence and Command Frigate (LCF), used to approximate APAR height above sea level. Image source: Damen Shipyards Group [48].

Implementing Equation 60 for a target altitude of 10m above sea level, Figure 58 presents the the resulting radar horizon distance as a function of radar height. Figure 58 shows that assuming a radar height of 27.25m is a good estimate for the APAR. The radar horizon distance does not differ greatly between an APAR height of 25 and 30 meters above sea level.

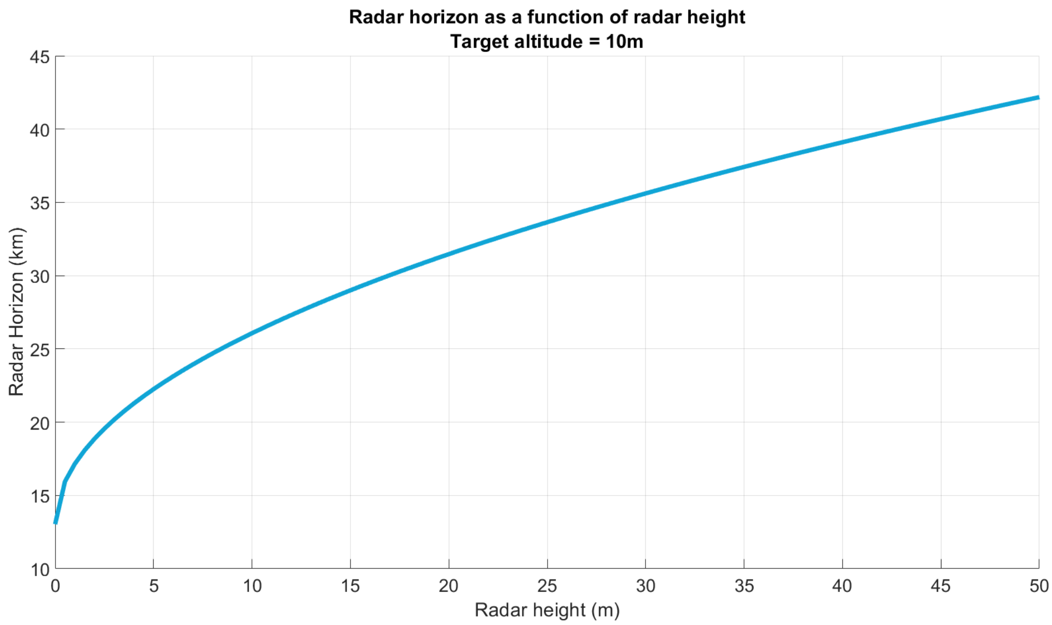

Figure 58: Radar horizon as a function of radar height for a target at 10m above sea level.

A.8. Additional flyout tables and trajectories - Intercept angle at the Primary Command Point: +45 Degrees

Figure 61 presents the flyout tables for the SM-2 Block IIIA where the terminal intercept angle is specified to be +45 degrees.

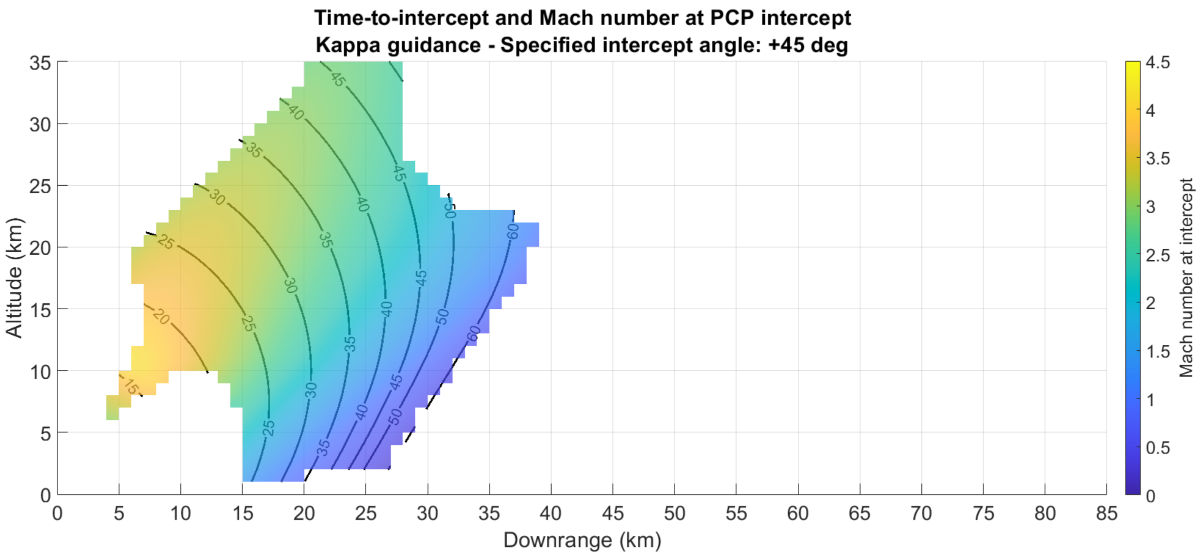

Figure 59: Time-to-intercept and Mach number at intercept for SM-2 Block IIIA. Specified intercept angle: +45 degrees. Time-to-intercept contour lines are constructed every 5 seconds for time-to-intercept = [15:50] seconds and every 10 seconds for time-to-intercept = [50:60] seconds.

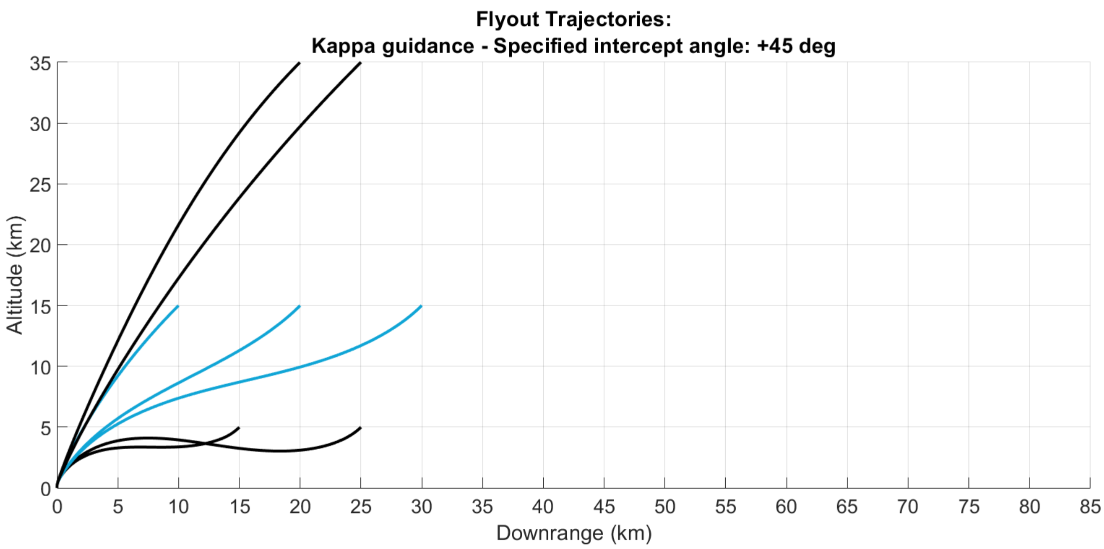

Figure 60: Flyout trajectories for Kappa guidance with a specified intercept angle of +45 degrees

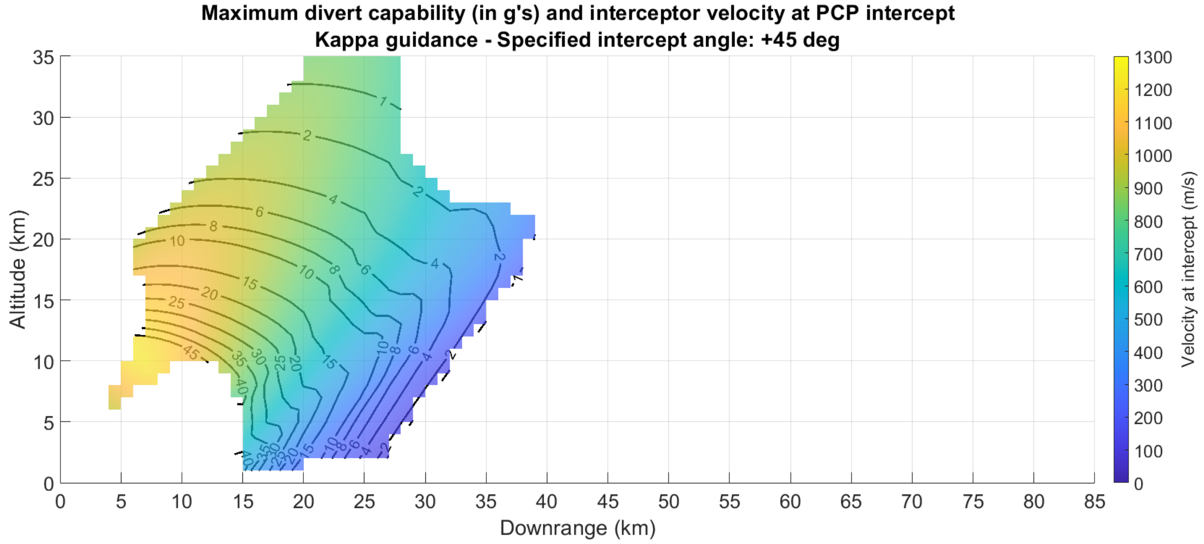

Figure 61: Maximum divert capability (in g's) and interceptor velocity at PCP intercept for Kappa guidance with a specified intercept angle of +45 degrees. Maximum divert contour lines are constructed at maximum divert = 1g, every 2 g's for maximum divert = [2:10], and every 10 g's for maximum divert = [15:45].

A.9. Missile DATCOM 98 Inputs

A.9.1. Trimmed conditions

```
CASEID RIM-167 SM-2 Blk-IIIA full wing new tail
DIM M
DERIV RAD
$FLTCON
       NALPHA=20.,
       ALPHA=0.,1.,2.,3.,4.,5.,6.,8.,10.,12.,
       ALPHA(11)=14.,16.,20.,24.,28.,32.,36.,40.,44.,48.,
       NMACH=20.,
       MACH=0.1,0.5,0.7,0.9,0.95,1.0,1.05,1.1,1.3,1.5,
       MACH(11)=1.6,1.8,2.4,2.5,2.6,2.75,3.0,3.5,4.25,5.0,
       ALT=0.,0.,0.,0.,0.,0.,0.,0.,0.,0.,
       ALT(11)=0.,0.,0.,0.,0.,0.,0.,0.,0.,0.,
       PHI=0.,
$END
$REFQ
       LREF=0.3432,
       XCG=1.925,
       SREF=0.0925
       BLAYER=TURB,
       RHR=125.,
$END
$AXIBOD
       LNOSE=0.699,
       DNOSE=0.3432,
       BNOSE=0.,
       TNOSE=KARMAN,
       LCENTR=4.021,
       DCENTR=0.3432,
       DEXIT=0.,
$END
$FINSET1
       XLE=1.4793,1.5521,2.1881,2.2677,
       SSPAN=0.0,0.045,0.055,0.136,
       CHORD=2.1515,2.0387,1.3876,1.2270,
       ZUPPER=0.019,0.009,0.0125,0.007,
       ZLOWER=0.019,0.009,0.0125,0.007,
       LMAXU=0.04,0.04,0.04,0.04,
       LFLATU=0.92,0.92,0.92,0.92,
       NPANEL=4.,
       PHIF=45.,135.,225.,315.,
$END
$FINSET2
```

```
        XLE=4.3560,4.4596,4.4996,
        SSPAN=0.0,0.266,0.3684,
        CHORD=0.3640,0.1667,0.,
        ZUPPER=0.025,0.020,0.020,
        ZLOWER=0.025,0.020,0.020,
        LMAXU=0.3,0.3,0.3,
        LFLATU=0.4,0.4,0.4,
        NPANEL=4.,
        PHIF=45.,135.,225.,315.,
$END
$TRIM
        SET=2.,DELMIN=-50.,DELMAX=50.,
        PANL1=.TRUE.,PANL2=.TRUE.,PANL3=.TRUE.,PANL4=.TRUE.$
SOSE
NO LAT
PLOT
SAVE
NEXT CASE
```

A.9.2. Coefficient and dervatives at specific δ

```
CASEID RIM-167 SM-2 Blk-IIIA full wing new tail
DIM M
DERIV RAD
$FLTCON
        NALPHA=19.,
        ALPHA=0.,1.,2.,3.,4.,5.,6.,8.,10.,12.,
        ALPHA(11)=16.,20.,24.,28.,32.,36.,40.,44.,48.,
        NMACH=20.,
        MACH=0.1,0.25,0.7,0.9,0.95,1.0,1.05,1.1,1.3,1.5,
        MACH(11)=1.6,1.8,2.4,2.5,2.6,2.75,3.0,3.5,4.25,5.0,
        ALT=0.,0.,0.,0.,0.,0.,0.,0.,0.,0.,
        ALT(11)=0.,0.,0.,0.,0.,0.,0.,0.,0.,0.,
        PHI=0.,
$END
$REFQ
        LREF=0.3432,
        XCG=1.925,
        SREF=0.0925
        BLAYER=TURB,
        RHR=125.,
$END
$AXIBOD
        LNOSE=0.699,
        DNOSE=0.3432,
        BNOSE=0.,
```

```
        TNOSE=KARMAN,
        LCENTR=4.021,
        DCENTR=0.3432,
        DEXIT=0.,
$END
$FINSET1
        XLE=1.4793,1.5521,2.1881,2.2677,
        SSPAN=0.0,0.045,0.055,0.136,
        CHORD=2.1515,2.0387,1.3876,1.2270,
        ZUPPER=0.019,0.009,0.0125,0.007,
        ZLOWER=0.019,0.009,0.0125,0.007,
        LMAXU=0.04,0.04,0.04,0.04,
        LFLATU=0.92,0.92,0.92,0.92,
        NPANEL=4.,
        PHIF=45.,135.,225.,315.,
$END
$FINSET2
        XLE=4.3560,4.4596,4.4996,
        SSPAN=0.0,0.266,0.3684,
        CHORD=0.3640,0.1667,0.,
        ZUPPER=0.025,0.020,0.020,
        ZLOWER=0.025,0.020,0.020,
        LMAXU=0.3,0.3,0.3,
        LFLATU=0.4,0.4,0.4,
        NPANEL=4.,
        PHIF=45.,135.,225.,315.,
$END
$DEFLCT
        DELTA2=-0.,-0.,0.,0.,
SOSE
NO LAT
PLOT
SAVE
NEXT CASE
```